E-630

ABSTRACT

A STUDY OF THE PROPERTIES OF MUONS PRODUCED IN THE DECAYS OF CHARMED PARTICLES

PATRICIA LOUISE MCBRIDE

Yale University, 1984

One of the most efficient ways of studying particles with lifetimes on the order of 5×10^{-13} seconds is with a high resolution ($<100\ \mu$) visual detector employed as a target in a high energy particle beam. The initial particle interactions and subsequent decays can be directly observed and measured. The High Resolution Streamer Chamber, designed and built at Yale, is one such detector. This dectector, used in conjunction with a highly selective trigger, produced a data sample of hadronic interactions rich with charm particle production.

This dissertation will describe an experiment in which charmed particles produced in collisions of high energy neutrons (~330Gev) on Helium-Neon nucleons were observed inside the Streamer Chamber. The primary focus will be on the properties of muons generated in the decays of the charmed particles. The average charm branching ratio into electrons has been measured to be 8%. We employed a muon trigger which enhanced the charm content of our data sample by a factor of 40. We measured the momentum and charge of each trigger muon with two steel toroidal magnets. A sample of 23 charm candidates with a background of 5.68 events was observed.

From these events we conclude that $D\bar{D}$ production is dominant over associated production of $\Lambda_c^+\bar{D}$ and that the D's ($c\bar{q}$) are produced centrally in p-N collisions. The measured momentum and transverse momentum spectra are consistent with $D\bar{D}$ production. Furthermore, the results are consistent with the standard model of charm decay which assumes μ-e universality. The average charm lifetime was measured to be $(6\pm1)\times10^{-13}$sec.

A STUDY OF THE PROPERTIES OF MUONS PRODUCED IN THE DECAYS OF CHARMED PARTICLES

A Dissertation

Presented to the Faculty of the Graduate School

of

Yale University

in Candidacy for the Degree of

Doctor of Philosophy

by

PATRICIA LOUISE MCBRIDE

MAY, 1984

In memory of my mother
Patricia Cramer McBride

Acknowledgements

Many people have made large contributions to this experiment and to the quality of my life at Yale and at Fermilab where I spent several winters. To begin, I would like to acknowledge the dedication and fatherly leadership of the late Horace D. Taft, Professor of Physics. His contributions to the on-line software were tremendous, but it was his persistent alertness and cheerfulness at the start of the 4 AM shift that remain a constant inspiration.

I would like to thank my advisor, Jack Sandweiss, who is always a great source of new ideas and encouragement. The help and friendship of Jean Slaughter has been invaluable. Without her, the experiment described in this thesis would have never come together. Dick Majka deserves special recognition for his skill with electronics and for his terrific coffee. I would especially like to thank Dick and Jean for carefully reading this thesis.

I would like to acknowledge all the collaborators on this experiment: Liang Tzeng, Peter Cooper, Marvin Johnson, Peter Nemethy and Lucien Teig. Andy Disco and David (Liang) Tzeng deserve great praise for their work with the streamer chamber.

The PWC's were built with the aid of Ed Arko, Don Emery, Victor Martinez and the Fermilab PC shop. Jim and John Welch, Greg Granberg and Tom Butler were indispensible in the installation of the chambers in the beam line.

I would also like to thank the staff of the Proton Lab at Fermilab for all their help in building and running this experiment. Here at Yale, Ozzie Murphy and Dennis Petrillo were instrumental in maintaining the smooth operation of the film measuring facility.

Much of the film scanning and measuring was performed at the Fermilab Film Analysis Facility. Candy Kastner and Annette Bays deserve special recognition for their

speed and dedication. Here at Yale, Catherine Bettega has been a tremendous help to this experiment. Developing the film analysis program for streamer chamber work was no easy task. I would like to thank Catherine for her patience and dedication throughout that development.

Peter Martin and Sara Batter have made our lives at Yale immeasurably easier and much more enjoyable. Phyllis Hale and the late Joanie Bjorken were their counterparts at Fermilab. All I can say is Thank You.

Piotr Karasinski implemented MACSYMA for the muon momentum analysis. Rob Steiner, Kevin Black and Yau Wah provided great encouragement, friendship and help when it was most needed.

To all my friends at Yale and at Fermilab who have shared the good times and commiserated during the bad, I express my thanks. I know that I will miss them in years to come.

Last of all, I would like to thank Bill Sherman, who did, among other things, the drafting for this thesis.

Table of Contents

List Of Figures vii

List Of Tables x

Chapter 1: Introduction 1

Chapter 2: A Review of Charm Production and Decay 4
- 2.1 Production 4
  - 2.1.1 Fusion models 4
  - 2.1.2 Recombination 5
  - 2.1.3 Flavor Excitation 7
- 2.2 Decay Properties 9
  - 2.2.1 Muon-Electron Universality 16

Chapter 3: Experimental Apparatus 19
- 3.1 The Streamer Chamber 20
- 3.2 The Neutron Beam 24
- 3.3 The Downstream Spectrometer 32
  - 3.3.1 The Hadron Shield 32
  - 3.3.2 The Toroids 36
  - 3.3.3 The Trigger Counters 38
  - 3.3.4 Trigger Electronics 41
  - 3.3.5 Proportional Wire Chambers 42
- 3.4 Installation 47

Chapter 4: Data Acquisition 48
  - 4.0.1 The Trigger 48
  - 4.0.2 Background Triggers 49
  - 4.0.3 The Trigger Logic 50
- 4.1 Gating 55
- 4.2 Monitoring the Experiment 55
  - 4.2.1 Monitoring the Streamer Chamber 57
  - 4.2.2 The Wire Chambers 57
- 4.3 Muon Studies 58
- 4.4 Alignments 59

Chapter 5: Film Analysis 60
- 5.1 Event Measurement 61

5.1.1 Data Handling 63
5.2 The Picture Analysis 63
5.2.1 Track and Vertex Fitting 64
5.3 Candidate Selection 66
5.4 The final event selection 67

Chapter 6: Momentum Analysis 73
6.1 Event Selection--The First Pass 74
6.2 Muon Studies and Alignments 76
6.3 Refinements in the Analysis 80
6.4 Cluster Studies 80
6.5 Muon Selection-The Second Pass 82
6.6 Momentum Analysis 84
6.7 A Summary of the Muon Selection 88

Chapter 7: Results and Conclusions 90
7.1 Production Characteristics 91
7.2 The Momentum Spectrum 99
7.3 The Average Charm Lifetime 110
7.4 Conclusions 113

Appendix I: The Momentum Analysis 117
I.1 The Probability Density Function 118
I.2 Generating the Likelihood 123

Appendix II: Monte Carlo Simulation 128
II.1 Event Generation 128
II.2 The Muon Trajectories 130
II.3 The Streamer Chamber 134

Appendix III: The Candidate Events 136

List of Figures

Figure 2-1:	Gluon-gluon and quark-quark fusion diagrams	6
Figure 2-2:	Flavor excitation diagrams contributing to QCD calculations of order $[\alpha^2]$ for hadronic charm production	10
Figure 2-3:	Blow-up of a flavor excitation diagram showing the beam hadron collision with the active quark inside the target hadron. The spectator c quark is able to recombine with quarks from the target.	10
Figure 2-4:	Decay of a charmed quark and a muon	12
Figure 2-5:	Spectator diagrams contributing to the decays of charmed mesons	14
Figure 2-6:	Non-spectator diagrams contributing to charmed particle decays	15
Figure 3-1:	Drawing showing the inside of the high resolution streamer chamber	21
Figure 3-2:	The Marx Generator and Blumlein pulse forming system	23
Figure 3-3:	Two pictures from the streamer chamber	25
Figure 3-4:	Schematic diagrams of the neutron beam	28
Figure 3-5:	Layout of E-630 neutron beam	29
Figure 3-6:	Image of the neutron beam at the entrance to the streamer chamber; actual size	30
Figure 3-7:	The neutron spectrum	31
Figure 3-8:	Acceptance for charm decay muons for a) momentum and b) polar angle θ	33
Figure 3-9:	Drawing of the E-630 Spectrometer	34
Figure 3-10:	Cross Section of the first section of the Hadron Shield	36
Figure 3-11:	Steel toroidal magnet used in muon spectrometer	37
Figure 3-12:	The trigger counters; the shaded region shows a muon trigger from an interaction	40
Figure 3-13:	Cross section of the hole in PWC D	45
Figure 3-14:	Schematic of the PWC Gas System	46
Figure 3-15:	Diagram of the PWC Electronics	46
Figure 4-1:	The Fortran subroutine that defined the logical functions of the PLU's	51
Figure 4-2:	The Trigger Logic Diagram, Part I: This shows each logic path for the trigger requirements N,I,CV,MU,and T2.	53
Figure 4-3:	The Trigger Logic Diagram, Part II: This shows the final trigger selection units and the data acquisition control.	54
Figure 4-4:	The electronics for the trigger gating system	56
Figure 5-1:	An example of a reconstructed event showing the measured points, the fitted tracks and the boundaries of the obscured region	65
Figure 5-2:	a) Schematic drawing showing the topology cuts; b)Schematic drawing showing the miss distance	68

Figure 5-3: The Candidate events with $S/\Delta S > 3.0$ 71

Figure 5-4: The $S/\Delta S$ distributions for Monte Carlo events with and without charm; the NIC̄V̄ distribution was plotted before rescanning for mismeasurements 72

Figure 6-1: Change in ϕ from chamber D to chamber T2. The solid curve is the same distribution in a Monte Carlo simulation. 77

Figure 6-2: The ΔU distributions for triplets with one and only one cluster in each of the PWCs' three planes 78

Figure 6-3: Scattergrams of momentum versus -ln(L) for a) the data, and for b) Monte Carlo events 87

Figure 6-4: The distribution in azimuthal angle of all NIC̄V̄MU events in the Matched Muon sample 89

Figure 6-5: The distribution in polar angle of all NIC̄V̄MU events in the Matched Muon sample 89

Figure 7-1: The distribution of the polar angle θ of the muons from the 23 candidate events 92

Figure 7-2: The distribution of the azimuthal angle ϕ of the muons from the 23 candidate events 93

Figure 7-3: The momentum spectra for the charge mode categories $(-+)$ and $(--)$ 97

Figure 7-4: The momentum spectra for the charge/mode categories $(++)$ and $(+-)$ 98

Figure 7-5: Muon Momentum Spectrum for the Charm Candidates 100

Figure 7-6: Measured Muon Momentum spectrum as predicted by the production model $(1 - |x|)^7(1 - |x|)^1$ for $D\bar{D}$ pairs. The data points, with errors, are also shown 101

Figure 7-7: Measured Muon Momentum spectrum as predicted by the production model $(1 - |x|)^5(1 - |x|)^5$ for $D\bar{D}$ pairs. The data points, with errors are also shown 102

Figure 7-8: The electron energy spectrum measured by the DELCO Collaboration at 3.77 GeV. The curve is the spectrum of electrons in the center of mass frame of the charmed meson in our Monte Carlo simulation. 104

Figure 7-9: The measured P_t spectrum of the 23 Charm Candidates. The average value of P_t is 0.81 GeV/c (background corrected). 105

Figure 7-10: The background added P_t spectrum predicted by the production model $(1 - |x|)^7(1 - |x|)^1$ for $D\bar{D}$ pairs. The data points and errors are also shown. 106

Figure 7-11: The background added P_t spectrum predicted by the production model $(1 - |x|)^5(1 - |x|)^5$ for $D\bar{D}$ pairs. The data points and errors are also shown. 107

Figure 7-12: The P_t spectrum of the 140 background muon events 108

Figure 7-13: The acceptance in P_T for charm taking into account the trigger and the $S/\Delta S$ analysis 109

Figure 7-14: The miss distance (S) distribution for the a) Charm Candidates b) 14 NIC̄V̄ events 111

Figure 7-15: Plot of the - ln (L) for single lifetime fits to the measured miss distance distribution. 112

Figure 7-16:	The integral distribution of the measured miss distances and the prediction of the model where the D lifetime is 5 x 10^{-13} sec.	114
Figure 7-17:	The intrgral distribution of the measured miss distances and the predictions of the model in which $D^{\pm}$ has a lifetime of 8.2×10^{-13}sec and D^0 has a lifetime of 3.9×10^{-13}sec	115
Figure 8-1:	One scatterer and one chamber	119
Figure 8-2:	Schematic layout of the downstream hadron shield and toroids	120
Figure 8-3:	Momentum resolution, $\delta p/p$, taken from Monte Carlo events	125
Figure 8-4:	Polar angle resolution, $\delta\theta$ in radians, taken from Monte Carlo events	126
Figure 8-5:	Azimuthal angle resolution, $\delta\phi$ in degrees, taken from Monte Carlo events	127
Figure 9-1:	An outline of the Monte Carlo	129
Figure 9-2:	The bending of a particle in the steel toroid	132
Figure 9-3:	The muon trajectory Monte Carlo for a muon of charge Q and momentum P	135

List of Tables

Table 2-1:	Prediction of quark counting rules, taken from the fusion model and quark recombination. The experimental results are taken from [7, 8, 96, 98]	8
Table 2-2:	Table showing results of three beam dump experiments' measurements of the ratio of prompt electron neutrino flux to muon neutrino flux	18
Table 3-1:	Features of the high resolution streamer chamber	24
Table 3-2:	Neutron Beamline Channel and Collimators	27
Table 3-3:	Characteristics of the neutron beam	30
Table 5-1:	Final results of the $S/\Delta S$ analysis	70
Table 7-1:	The Charge and Mode ratios of the 23 charm candidates and the background events	95
Table 7-2:	The Charge / Mode Fractions for eight Charm production models.	96
Table 7-3:	Values of the likelihood for five different lifetimes. Here we have assumed that the charm events were of a single lifetime.	113

Chapter 1

INTRODUCTION

In the initial conception of the quantum number charm in 1964, there was a desire by physicists to maintain a harmonious symmetry between hadrons and leptons [35]. The charmed quark was more formally introduced in the model of Glashow, Illiopoulos and Maiani in 1970 as a means of explaining the noted absence of strangeness changing neutral currents [67]. The Weinberg-Salam model of weak interactions predicted both strangeness changing and strangeness conserving currents. At that time, neither had been directly observed, but the processes $K_L{}^0 \rightarrow \mu^+\mu^-$ and $K^+ \rightarrow \pi^+\nu\nu$ were found to be highly suppressed. The addition of a fourth quark led to a cancellation of the $s \leftrightarrow d$ part of the weak hadronic current.

Indirect evidence of the fourth quark came from measuring $R(W) \equiv \sigma_{tot}(e^+e^- \rightarrow$ hadrons$)/\sigma(e^+e^- \rightarrow \mu^+\mu^-)$ in 1973 [78]. The observed rise of R(W) above W=3 GeV was in conflict with the three quark prediction. It was a year later that the first direct evidence of the fourth quark, the charmed quark, was announced.

The quantum number charm (C) is conserved in the strong and electromagnetic interactions. The fourth quark has quantum numbers S=0, Q=2/3, B=1/3 and C=1. The charmed quark (c) will decay weakly into a strange (s) quark, cabibbo-favored, or a down (d) quark, Cabibbo-suppressed, by emitting a virtual W^+. Low mass states of charmed particles were predicted to decay weakly.

The first observations of the bound state of a charm-anticharm pair were announced by two experiments, one at the AGS [17] and one at SLAC [24]. The newly discovered J/ψ resonance was eagerly studied by many experimenters. Measurements of the excited states of the J/ψ and the radiative transitions between the states were soon to follow. Open (or bare) charm, the combination of a charmed quark with a lighter quark partner in a hadron, was observed in e^+e^- collisions at SLAC [69, 88]. The measured hadron spectrum verified the existence of the fourth quark.

The early experiments studying open charm states were performed at e^+e^- machines because of the simplicity of the events and the possibility of high production cross sections relative to background events. Precision measurements of the masses of the D mesons were made by examining the interaction $e^+e^- \rightarrow \psi''$ which decays into $D\bar{D}$ pairs. Measurements of the branching fractions describing charm decay products were first done at e^+e^- machines. In particular, the average semi-leptonic branching ratio has been measured by several experiments [26, 10, 111]. Many other properties of open charm, such as the spin, were first examined by e^+e^- experiments.

However, to study the charmed meson and baryon lifetime directly, fixed target experiments were needed. The short lifetimes characteristic of weak charm decay are observable with high resolution detectors in high energy photon, lepton or hadron beams. Many experiments have recently measured the charm lifetimes. Among them was a Fermilab experiment using a neutrino beam incident on an emulsion target followed by a downstream spectrometer (The E531 Collaboration). They have reported results on the lifetimes for the D^0 [113], $D^\pm$, F^+ and Λ_c^+ [114, 115], but still with limited statistics. Other results have been reported by the LEBC collaboration at CERN [6]. They used a small, high resolution hydrogen bubble chamber in front of a spectrometer. They operated in a hadron beam, and reported results from π^-p and pp data. Many other experiments have reported charmed meson and baryon lifetime measurements [1, 94] in the past few years including one using an active silicon target [11]. The reported lifetimes are 3.9×10^{-13} sec for the D^0 and 8.2×10^{-13} sec for the D^+.

Fixed target experiments, in general, are of three types. First, there are the spectrometers complete with momentum measurment and particle identification. They have the capability to fully reconstruct the charm decay products for specific final states. The high multiplicities associated with high energy collisions make their data difficult to analyze. The second class of experiments utilize high resolution vertex detectors in order to directly observe the charm decay vertex. Often the vertex detector is used in conjunction with a full downstream spectrometer forming a hybrid spectrometer. Several such experiments were mentioned above. In the third class of experiments, the momentum of a prompt lepton produced in the interaction of a lepton or hadron inside a dense target is measured and this will provide indirect information about the charm production and decay properties.

The experiment discussed in this thesis combines the latter two methods. We directly observed the production and decay of charmed particles from hadronic interactions inside a high resolution streamer chamber. Each streamer chamber event was triggered by a prompt muon with momentum greater than 6.5 GeV/c. The measurement of the hadronic charm production cross section from this experiment has been presented elsewhere [112]. This thesis will concentrate on the hadronic production properties as inferred from the muon momenta and the charm lifetime(s) as measured in the streamer chamber.

Chapter Two gives a brief overview of the theory of hadronic charm production and the fundamentals of charm decay. Chapter Three contains a description of the apparatus and the beam. The data acquisition is discussed in Chapter Four. The next two chapters focus on the event selection and analysis. Chapter Five outlines the film analysis and Chapter Six the muon momentum analysis. The results of the final sample selection are presented at the end of Chapter Five. The final analysis of the selected events is presented in Chapter Seven.

Chapter 2

A REVIEW OF CHARM PRODUCTION AND DECAY

2.1 Production

Production of heavy flavors has been a topic of great interest for several years as a new testing ground for QCD. Charm quark production is in a regime where QCD processes are (almost) calculable. Perturbative QCD has been employed to predict the production of the ψ in muon and photon production [72, 85]. The successes in the comparison of theory and experiment has been encouraging, but by no means complete.

2.1.1 Fusion models

Hadronic cross section measurements of open charm states, however, have not been so easily explained by perturbative QCD. Calculations of open charm were first performed using gluon-gluon and quark-quark fusion models. Diagrams of the leading order fusion processes are shown in figure 2-1. Unfortunately, models based primarily on the fusion process have predicted charm cross sections that are an order of magnitude lower than measured cross sections at $\sqrt{s}$= 27, 53 and 62 GeV. Calculations have been performed that can eliminate the discrepancy in the cross section by lowering the value of the charmed quark mass to 1.15 GeV/c^2 [44]. This is, however, in conflict with the mass of 1.5 GeV/c^2 demanded by lepton production calculations. Moreover, these models have

been unable to explain the diffractive-type production of the charmed baryon Λ_c^+ observed at the ISR [119] or the reported enhancement of D^- and D^0 production in $\pi^- N$ and $\pi^- p$ collisions [29, 7, 98].

The gluon-gluon fusion process should be dominant over $q\bar{q}$ fusion processes in nucleon-nucleon collisions. The model predicts central production of charmed particles, reflecting the hard scattering of the gluons. The production of $D\bar{D}$ pairs is predicted to be clustered at low values of x_F:

$$E\frac{d^3\sigma}{dp^3} = A\ (1 - |x|)^n\ e^{-bp_t} \tag{1}$$

$$n = 4\text{-}6$$
$$b = 2.5\ (\mathrm{GeV}/c)^{-1}$$
$$x = x_F = P_{||}/P_{||max}$$

In the fusion model, all effects of the charm structure function of the nucleon are completely ignored, and the model gives no direct explanation of leading particles.

2.1.2 Recombination

Modifications to the fusion model have been proposed to explain the x_F dependence of the charm cross sections. Models in which the charmed quark recombines with a valence quark from the fragmenting beam particle have had some success. Simple quark counting rules derived from QCD calculations of sea quark distributions indicate an x_F dependence of $(1 - |x|)^1$ for Λ_c^+, $(1 - |x|)^3$ for the $\bar{D}$ associated with the Λ_c^+, and $(1 - |x|)^7$ for $D\bar{D}$ production. These quark counting rules treat the charmed sea quark as a part of the hadron bound state, and have been used to predict sea quark distributions of lighter quarks:

$$f(x) \sim (1\text{-}x)^{2n_s - 1}$$

where n_s is the number of spectator quarks transferring momentum via gluon exchange to the sea quark. In inclusive production of hadrons, the spectator quarks are those quarks not included in the final state hadron.

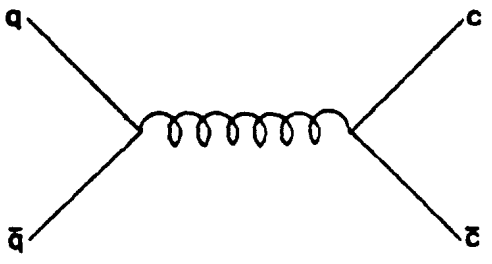

QUARK FUSION

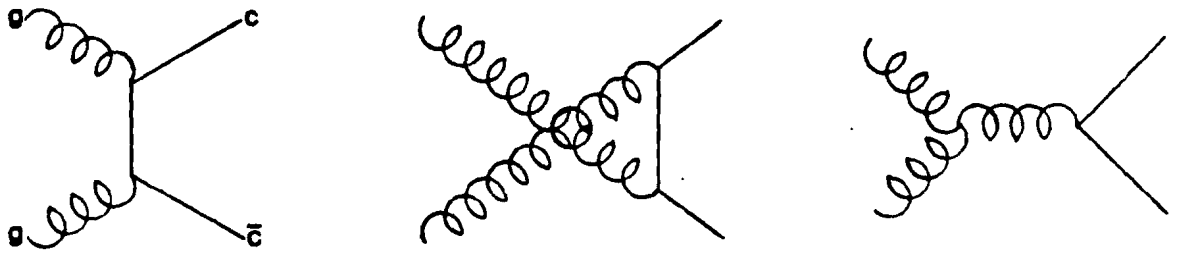

GLUON FUSION

Figure 2-1: Gluon-gluon and quark-quark fusion diagrams

Gunion [71] in 1979 proposed a modified spectator quark counting rule

$$f(x) \sim (1-x)^{2n_B+n_{PL}-1}$$

where n_{PL} is the number of spectator quarks that participate in the 'point-like' generation of a sea quark and n_B is the number of spectator quarks in a hadron bound state that includes the sea quark. In hadron collisions, inclusive differential cross sections of lighter mesons exhibit an x_F dependence that can in general be described by these modified quark counting rules.

While the results for $K^{\pm}$ production have been quite successful, the modified counting rules have been inadequate in accounting for the differential cross sections of charmed mesons that have been observed in pp collisions by the LEBC collaboration. A summary of the results of two experiments measuring the x_F dependence of the cross section are given in Table 2-1. The predictions of the modified counting rules are listed in direct analogy to K production. Two values of n are presented where it is thought that two mechanisms might contribute to the production, one producing a central distribution and one producing leading particles.

Though the comparison is crude, it seems that in pp collisions, the production mechanism may be different in $p \rightarrow D/\bar{D}$ than in $p \rightarrow K/\bar{K}$ fragmentation. The differences in the experimental results are not well understood. Possibly they could result from nuclear effects in the iron. There is certainly a need for more study and more experimental work.

2.1.3 Flavor Excitation

Originally, it was thought that fusion was the primary process in QCD contributing to heavy quark production in hadron collisions. However, after the measurements of hadronic cross sections at the ISR [66, 55, 56, 119]it was realized that flavor excitation of a charmed quark from the sea could not be ignored [48]. Another proposal brought forth a non-perturbative approach in which one of the hadrons emits a gluon which then simply fragments into a quark and antiquark [73].

beam	predicted n	LEBC (360GeV/c pH_2)	E-595 (350GeV pFe)
p D^- ($\bar{c}d$)	(5,4)	2±1	5.4+1.2 -0.9
$\bar{D}^0$ ($\bar{c}u$)	(5,3)	2±1	
D^0 ($c\bar{u}$)	5	2±1	4.1+1.7 -1.1
D^+ ($c\bar{d}$)	5	2±1	
		(360GeV/c $\pi^- H_2$)	(278GeV π^-Fe)
π^- D^- ($\bar{c}d$)	(5,1)	(6±3,1±1)	1.6±0.3,x_F>0.2
$\bar{D}^0$ ($\bar{c}u$)	(5,1)	(6±3,1±1)	
D^0 ($c\bar{u}$)	5	6±3	2.1±0.5, x_F>0.2
D^+ ($c\bar{d}$)	5	6±3	

Table 2-1: Prediction of quark counting rules, taken from the fusion model and quark recombination. The experimental results are taken from [7, 8, 96, 98]

Odorico, in an effort to explain hadronic charm production inside the framework of perturbative QCD, proposed a model including flavor excitation diagrams where the charm-anticharm quark pair is excited from the sea [87]. The lowest order diagrams are shown in Figure 2-2. A simple recombination model was included to describe hadronization. In the flavor excitation scheme, a quark in the beam hadron scatters off a charmed quark in the target hadron by exchanging a gluon. Figure 2-3 shows a close-up of a flavor excitation diagram. The target charmed quark is formed by QCD evolution, a cascade of quark and gluon creation in the nucleon. The QCD evolution is estimated by a Monte Carlo simulation of the cascade process. The effect is to simulate the charm structure function of the nucleon. The scale of the evolution, $Q^2_{evol} = -\hat{t}_{min}$ is set by

constraining the predicted $\langle p_T \rangle$ of the simulated hadrons to match measured values of $\langle p_T \rangle$ [119].

The flavor excitation scheme yields charm cross sections in good agreement with the measured values and accurately predicts the energy dependence. The spectator quark in this model is able to recombine with the valence quarks in the target nucleon to produce the leading particle effect at large values of x_F ($x_F > 0.5$). The active quark hadronization yields a more central distributions. Quantitative evaluation of the model at low x_F, however, is probably impossible because of soft hadron effects. Furthermore, the structure functions of heavy nuclei may not be the same as those of H_2 [21], so the effects of a nuclear target have not been predicted in these calculations. This experiment concludes that the A dependence of the cross section is $A^{2/3}$ rather than A^1. This conclusion is drawn by matching our cross section measurement for a neon target with the measurement of the LEBC Collaboration which used a hydrogen target [112, 9].

2.2 Decay Properties

The decay properties of charmed particles have been under investigation for some time. Much work has been done to establish the decay branching fractions. Of interest here, since the experiment uses a muon trigger, is the semi-leptonic branching ratio. An early measurement of the inclusive branching fraction into electrons gave a result of $Br(e^+e^- \rightarrow eX) = (8.0 \pm 1.5)\%$ [26]. More recent experiments have measured

$Br(C \rightarrow e) = (6.3 \pm 1.2 \pm 2.1)\%$ at 29 GeV e^+e^- [86]

$Br(C \rightarrow \mu) = (11.5 \pm 1.0 \pm 1.7)\%$ at $33 \leq \sqrt{s} \leq 38.54$ GeV e^+e^- [4]

$Br(C \rightarrow e) = (9.1 \pm 0.9 \pm 1.3)\%$ at 29 GeV e^+e^- [10].

Taking all the measurements, it is reasonable to assume the average branching ratio is 8% for $C \rightarrow e$ and $C \rightarrow \mu$.

Individual branching ratio measurements of charged and neutral D's have been less

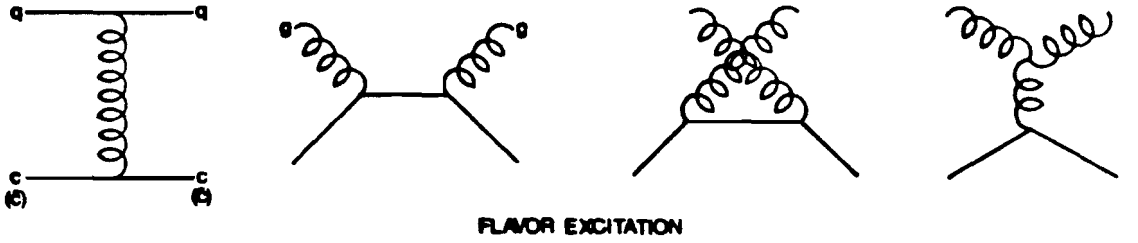

Figure 2-2: Flavor excitation diagrams contributing to QCD calculations of order $[\alpha^2]$ for hadronic charm production

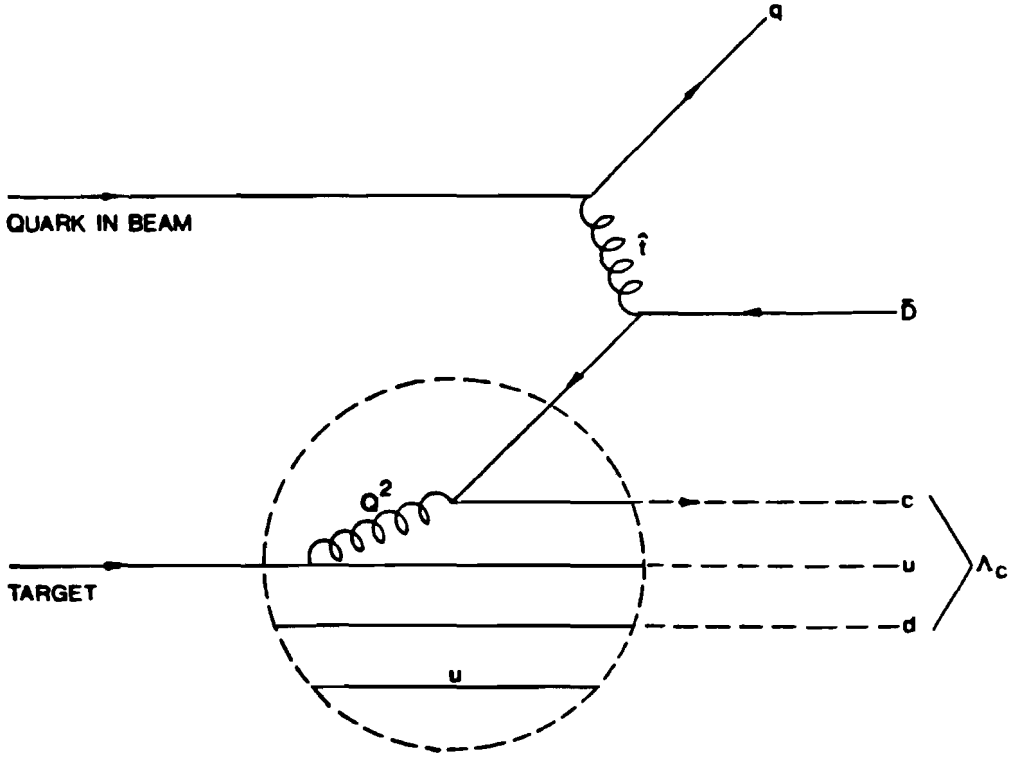

Figure 2-3: Blow-up of a flavor excitation diagram showing the beam hadron collision with the active quark inside the target hadron. The spectator c quark is able to recombine with quarks from the target

conclusive. Measurements of the semi-leptonic branching ratios by the DELCO collaboration and MarkII produced the following results.

	DELCO	MarkII
$Br(D^+ \rightarrow e)$	(22.2+4.4)%	(16.8±6.4)%
$Br(D^0 \rightarrow e)$	<4%	(5.5±3.7)%

The ratio of the semi-leptonic branching fractions $Br(D^+ \rightarrow e)/Br(D^0 \rightarrow e)$ is, however, proportional to the lifetime ratio for the two particles. This is due to the nature of the Cabibbo-favored semi-leptonic Lagrangian

$$L \sim \cos\theta_c (\bar{c}s)(l^+ \nu_e)$$

which carries an isotopic spin of zero. It follows that

$$\Gamma(D^+ \rightarrow l^+ + \nu + X^0) = \Gamma(D^0 \rightarrow l^+ + \nu + X^-)$$

where the X's are K's and K^*'s. Summing over these X's, one can relate the lifetimes to the semileptonic branching ratios [111]. Experiments measuring the lifetimes have been able to make more precise measurements.

The semi-leptonic branching fraction is important for determining the charm cross section from this experiment, but it is also important for understanding the mixture of $D^\pm$, D^0 and Λ_c^+ expected in the final data sample. While the average branching fraction for D's of all varieties is about 8%, the value for Λ_c^+ has been measured to be $Br(\Lambda_c^+ \rightarrow e)$=(2.7±1.7)% [107].

Naively, one would expect the semi-leptonic branching ratios to be the same for all charmed mesons and baryons. In the simplest model for the weak decay of a charmed hadron, the c quark decays by emitting a W^+ in direct analogy to μ decay (see Figure 2-4). This model is known as the spectator model since the other quarks in the hadron are not involved in the weak decay. The decay rate predicted by this model can be written

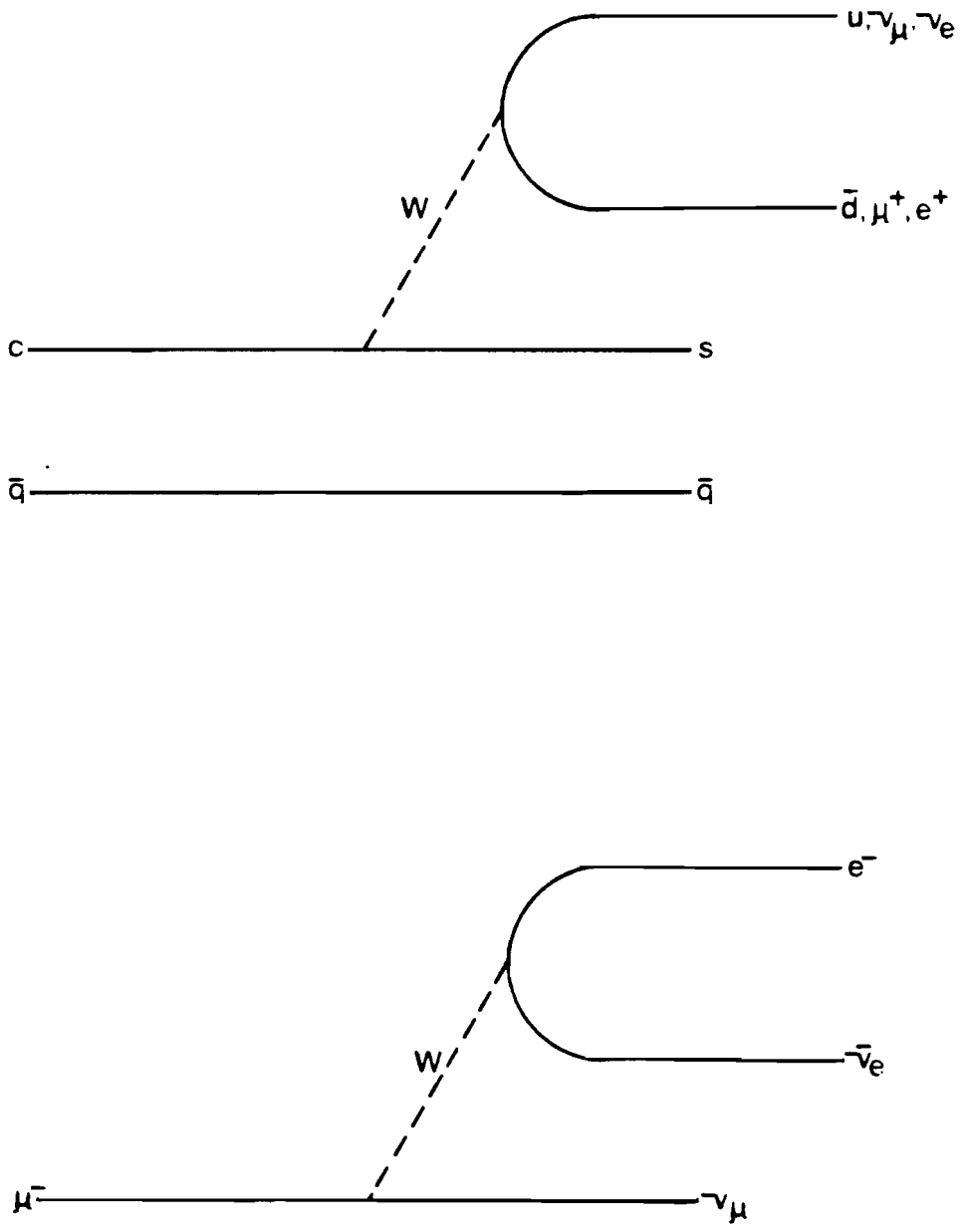

Figure 2-4: Decay of a charmed quark and a muon

$$\Gamma_{c_{tot}} = 5\left(\frac{M_c}{M_\mu}\right)^5 \Gamma(\mu \rightarrow e\nu\bar{\nu})$$

where M_c is the mass of the charmed quark. The factor 5 enters because the W couples to three colors of quarks and 2 lepton types. In this model, the semi-leptonic branching ratio and the lifetimes of the D^+, D^0, F^+ and Λ_c^+ are equal. Figure 2-5 shows the diagrams for charm decay in this model. Indicated on the diagram, are the Cabibbo-favored ($\cos\theta$) and suppressed ($\sin\theta$) decay modes.

However, experimental data are at odds with this naive model. The charmed quark does not always decay independently of the other quarks. Other Cabibbo-favored processes indicated in Figure 2-6 contribute to the decay of charmed mesons and baryons. The annihilation process contributes to F^+ decays, while the exchange process is important in D^0, $\bar{D}^0$ and Λ_c^+ decays. These processes are all Cabibbo-suppressed in $D^\pm$ decays. Gluonic effects must be considered in calculations of the non-spectator diagrams, particularly in the annihilation process where they are needed to conserve angular momentum. The ratio of the lifetimes $\tau(D^+)/\tau(D^0)$ gives an indication of the relative strengths of the spectator and non-spectator processes in charm decays.

Theoretical predictions using the spectator model to describe the semi-leptonic decay rate of the D^+ have been quite successful.

$$\Gamma(c \rightarrow e\nu X) \approx \left(\frac{M_c}{M_\mu}\right)^5 \Gamma(\mu \rightarrow e\nu_e\nu_\mu)$$

For a charmed quark mass of 1.5 GeV/c^2, the decay rate is calculated to be

$$\Gamma(c \rightarrow e\nu X) = 2.6 \times 10^{11}\ \mathrm{sec}^{-1}.$$

The agreement with the experimental measurement derived from D^+ lifetime measurements is quite remarkable.

$$\Gamma(D^+ \rightarrow e\nu X) = (2.4 \pm 0.6) \times 10^{11}\ \mathrm{sec}^{-1}\ [94]$$

The ratio of $\tau(D^+)/\tau(D^0)$ has been measured by a variety of experiments. The current world average for this ratio is

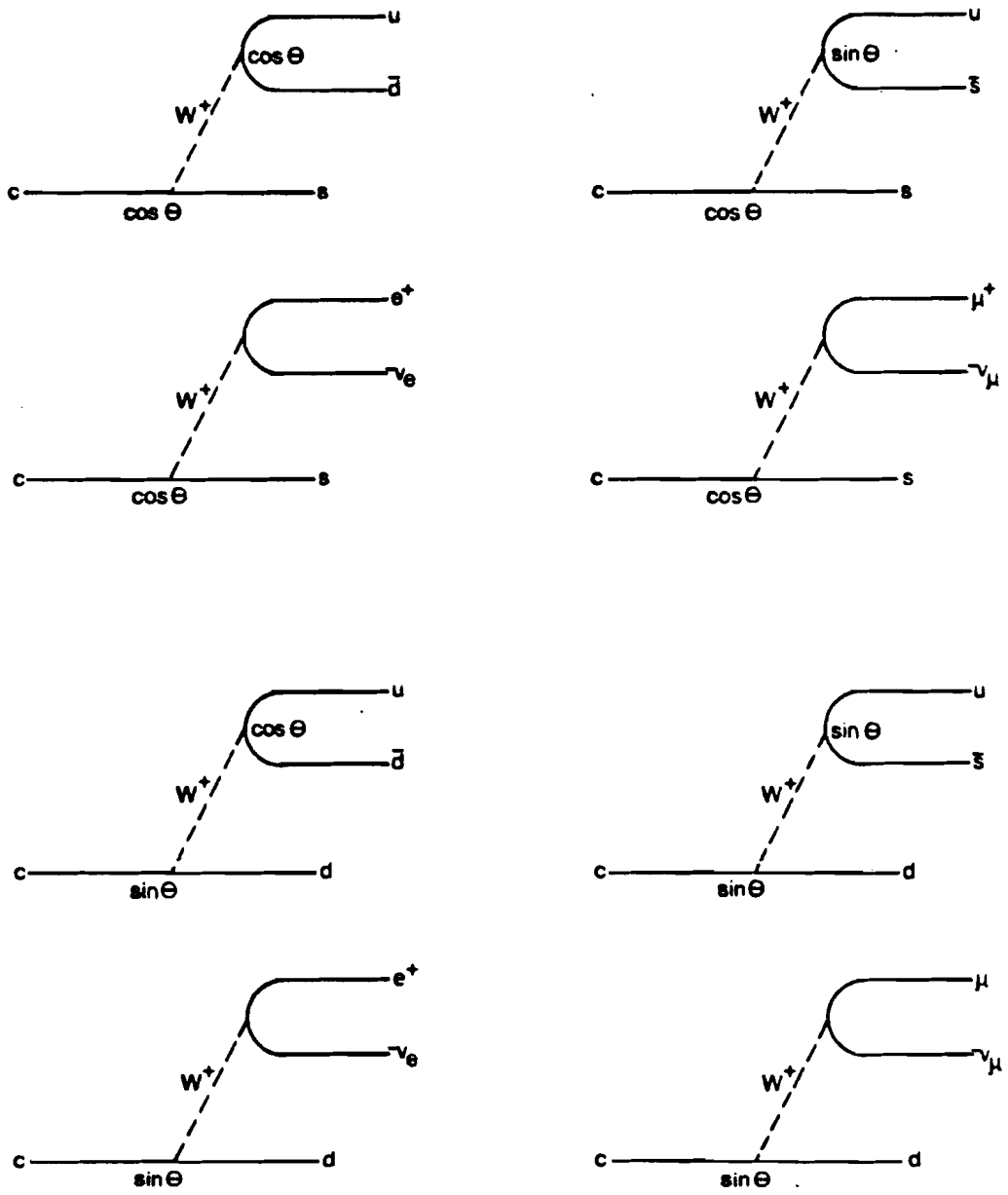

Figure 2-5: Spectator diagrams contibuting to the decays of charm mesons

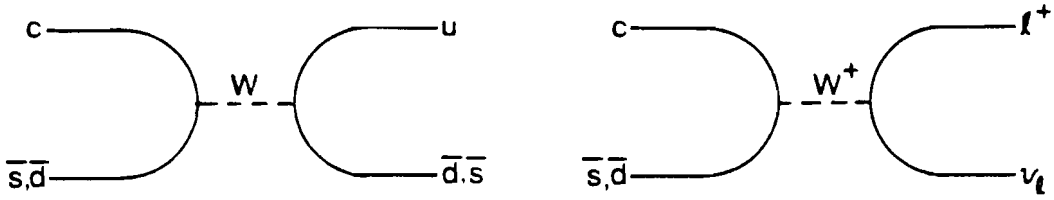

ANNIHILATION PROCESS

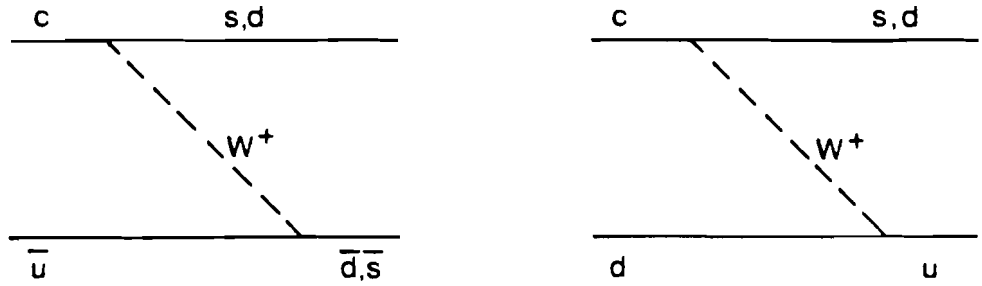

EXCHANGE PROCESS

Figure 2-6: Non-spectator diagrams contributing to charmed particle decays

$$\tau(D^+)/\tau(D^0) = 2.08 \pm 0.34 \text{ [94]}.$$

In this experiment, we measured an average value of the charm lifetime of $(6\pm1)\times10^{-13}$. We are not able to distinguish between charged and neutral charmed particles, because the decay vertices are not visible.

2.2.1 Muon-Electron Universality

In 1979 and 1982, the results from several beam dump experiments performed at CERN indicated an excess of prompt muon neutrino flux relative to the observed prompt electron neutrino flux [13, 62, 74, 2]. These experiments measured the neutrino flux stemming from pN collisions of the 400 GeV/c SPS proton beam on the same thick copper target. The experiments observed a 5 standard deviation effect in the ratio of electron neutrino flux to muon neutrino flux:

$$\phi(\bar{\nu}_e+\nu_e)/\phi(\bar{\nu}_\mu+\nu_\mu) = 0.55\pm0.08$$

There has been much speculation about this ratio [51, 32]. The experiments were designed to observe the hadronic production of charmed particles in the beam dump. A ratio of electron to muon neutrino fluxes from charm decay that is different from one is inconsistent with the standard model of charm decay which assumes μ-e universality. Speculation has arisen that attributes the excess of electron neutrinos to the neutrino oscillations [51], to the preferential decay of a Higgs particle into $\nu_\mu\bar{\nu}_\mu$, or to a π meson whose branching ratio $e\nu_e$ is suppressed [72]. However, experimental evidence goes against these theories.

Barger et al. [32] have proposed a theory of charm decay in which the charmed particle decays via a charged Higgs boson which does not couple to first generation leptons and quarks. Thus the model predicts $C\rightarrow s$ and $H^+\rightarrow\mu^+\nu_\mu$. The muon energy distribution is predicted to be

$$E d\Gamma^{H}/dp \sim x(1-\tfrac{2}{3}x);$$

$$x = 2p_c \cdot p_\mu / m_c^2$$

rather than the

$$E\Gamma^{W}/d^3p \sim x(1-x)$$

distribution expected from W^+ decay. The harder muon spectrum of the Higgs decay should be observable in high energy charm decay into muons.

In 1983, two of the beam dump experiments presented new results [118] that are inconsistent with their old measurement. A third CERN experiment, by the CHARM Collaboration, however, presented a result that is consistent with the old measurement of ν_e/ν_μ ratio of 0.55 (See Table 2-2). Furthermore, a beam dump experiment at Fermilab has measured a ratio consitent with 1.0 [72, 118]. The question of μ-e universality in charm decay remains somewhat of a mystery. The results of this experiment, which measures the muons from charm decays, is consistent with the hypothesis of μ-e universality.

CDHS	$0.83 \pm 0.13 \pm 0.12$ preliminary
BEBC	$1.35^{+0.65}_{-0.34} \pm 12\%$
CHARM	$0.59^{+0.11}_{-0.10} \pm 0.08$

Table 2-2: Table showing results of three beam dump experiments' measurements of the ratio of prompt electron neutrino flux to muon neutrino flux

Chapter 3

EXPERIMENTAL APPARATUS

The goals of the experiment (FNAL-E630) were to observe the production and decays of charmed particles in high energy hadronic interactions. The experiment was completed at the 400 GeV proton synchrotron facility at Fermi National Accelerator Laboratory in Batavia, Illinois. The cross section for hadronically produced charm had been predicted and subsequently measured to be on the order of 30 microbarns [38]; in other words, there should be about one interaction producing charmed particles for every 1000 collisions involving protons or neutrons.

We felt that the best way to detect the charmed particles was to take advantage of their lifetime and search for decays in a high resolution vertex detector. The observation of a visible decay in a vertex detector would preferentially select events with short lifetimes and eliminate background from interactions containing only pions and strange particles whose lifetimes are orders of magnitudes larger. Bubble chambers and nuclear emulsions have been used successfully in charm searches [6, 113]; however, one would have to record 1000 interactions to record 1 charm events in hadronic interactions since neither are triggerable. The streamer chamber seemed an ideal device for this task, because it could be triggered and thus select events that were inherently charm-like. The difficulty lay in developing a streamer chamber with a resolution of less than 100 microns.

3.1 The Streamer Chamber

A high resolution streamer chamber has been developed at Yale [101]. It was first used in Fermilab experiment E-490 [102], a charm experiment and the precursor to this experiment. The chamber used in that experiment was modified and improved for use in E-630. A detailed discussion of the high resolution streamer chamber research and development program can be found in References [101], [112] and [80].

The high resolution streamer chamber was designed to act as a visual target for high energy hadron-hadron collisions. The visible volume of the chamber was 3 x 4 x .45 cm^3. It was filled with 40 atmospheres of Neon-Helium gas. The gas volume outside the fiducial region was held to a minimum by cones that protruded into the chamber tank. Windows for the beam were made of 50 μm stainless steel. The beam passed between two transparent electrodes that carried the high voltage pulse. A diagram of the streamer chamber is shown in Figure 3-1.

In a streamer chamber, ionization electrons left behind by the passing of high energy charged particles through a gas are accelerated in a electric field, setting off small avalanches which grow rapidly in the high electric field inside the chamber. The space charge on the outer edges of an avalanche becomes large enough to neutralize the field inside the avalanche. Inside the electrons and ions recombine emitting photons which can photo-ionize atoms in the gas. On the outside of the primary avalanche, the field is large enough to start secondary avalanches from the photoelectrons. The entire system begins to grow in what is called a self sustaining streamer mode. The field is cut off before the avalanching streamer forms a conducting path between the electrodes. The pulse length and voltage are set so that the streamers are visible but the chamber does not spark. Normal streamer chambers operate with a gas such as Ne- He at one atmosphere and pulses of 20 kV/cm and a pulse width of 10 nsec. The resulting streamers are about 1 mm in diameter.

The high resolution streamer chamber operated at a much higher pressure and a stronger but shorter high voltage pulse. As in conventional streamer chambers, the high

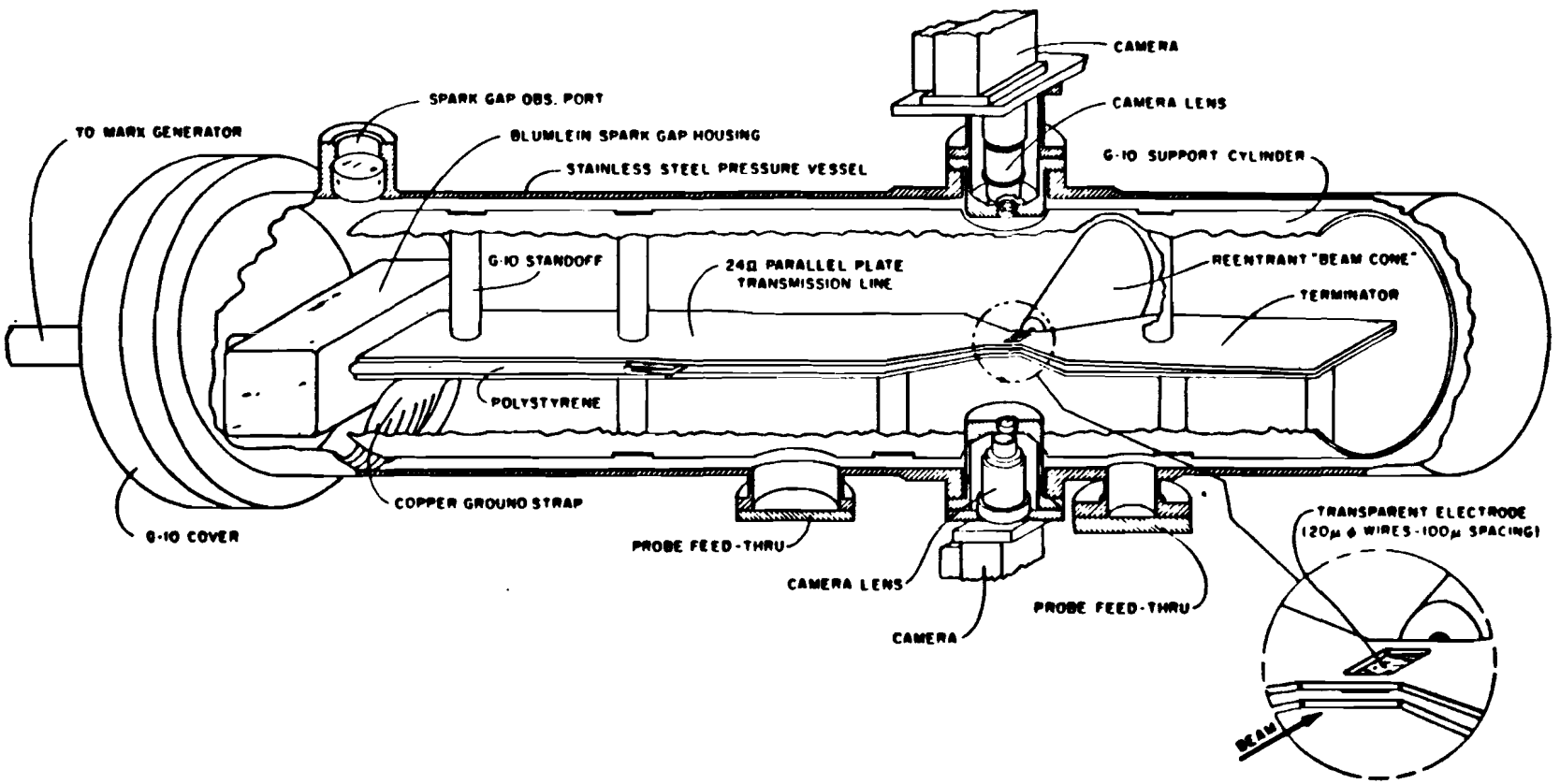

Figure 3-1: Drawing showing the inside of the high resolution streamer chamber

resolution chamber's pulse forming system consisted of a Marx generator connected to a Blumlein system. The Marx generator, made of ten capacitors, could yield voltages of 400kV. The output of the Marx generator was connected through a 100 Ω resistor to a short Blumlein electrode. The streamer chamber pulse was formed by a single spark gap between the electrode and the parallel transmission line as in Figure 3-2. The box surrounding the Blumlein electrode was filled with air or nitrogen to control the breakdown of the spark gap. The output pulse had the form of a heavily damped sine wave, characteristic of an RLC circuit [112]. The peak amplitude of the pulse corresponded to 60% of the voltage applied to the Blumlein electrode. The width (FWHM) of the output pulse was found to be 1.2-1.4 nsec. The parallel plates carrying the pulse to the streamer chamber ended in a carefully designed terminator. The chamber itself was made from 50 μm stainless wires stretched at intervals of 150 μm.

Under our operating conditions, the streamers were small and did not produce much light. Image intensifiers with a resolution of 50μm and a gain of 10,000 improved the sensitivity without spoiling the resolution. With these intensifiers, we were able to operate the chamber so that streamers with diameter comparable to the image intensifier resolution were visible on the film.

Cameras were mounted on the top and bottom of the streamer chamber with the film pressed against the outside of the image intensifier output windows. A lens was mounted between the image intensifiers and the transparent electrodes on each side of te chamber. One lens had a focal length of jfour inches and the other had a focal length of six inches. The image recorded on the film was reduced by the ratio 2 : 3. Furthermore, the lenses were mounted so as to provide a 7° stereo angle which would allow three dimensional reconstruction of the particle tracks. The resolution in the vertical plane was quite poor, because of the small stereo angle [112].

Table 3-1 shows the operating parameters of the high resolution chamber. The primary contribution to the track width was the diffusion of the primary ionization electrons before the arrival of the high voltage pulse. The addition of CO_2 to the gas

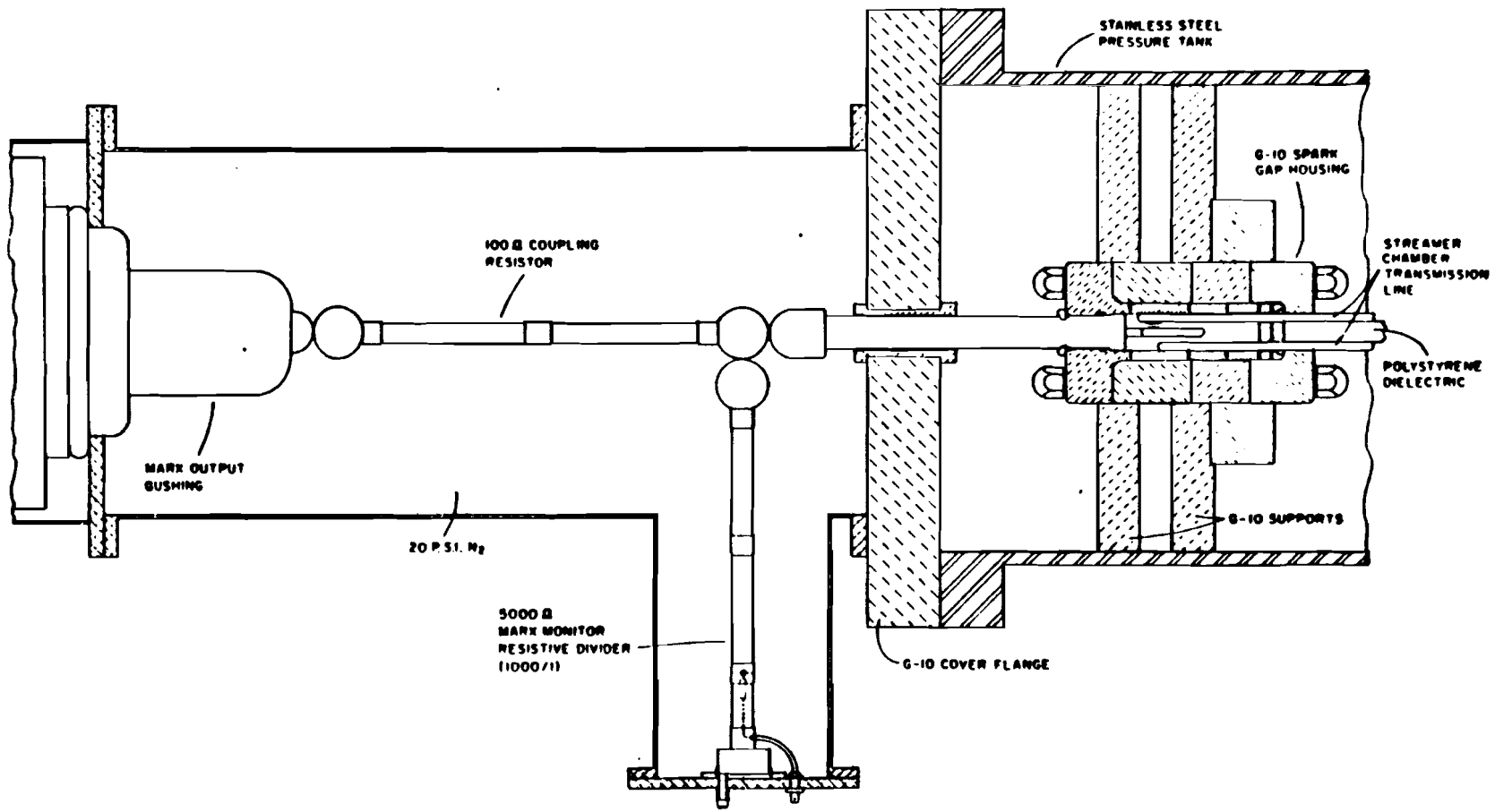

Figure 3-2: The Marx Generator and Blumlein pulse forming system

reduced the diffusion problem, but in the end, this was the limiting factor for the resolution. The minimum distance between two measurable tracks was 150μm as measured on the film, which was notably worse than the measurement resolution for clean clear tracks ($\sim$20μm). One difficulty was the reflection of light off the wires in the streamer chamber electrodes. The two track resolution and the reflections caused by regions of heavy ionization put serious limits on the capabilities of the detector. In fact, the forward travelling tracks were obscured in many events. Despite these limitations, we were able to collect a clean sample of charm events.

Chamber Gas	40 atmospheres Ne/He 2.5% CO_2
High voltage pulse amplitude	150-160 kV
Pulse width(FWHM)	1.3 ns
Visible dimensions of the chamber	3 x 4 x 0.45 cm^3
Optical Gain	10,000
Streamer diameter	50μm
Track width (in space)	120μm

Table 3-1: Features of the high resolution streamer chamber

Figure 3-3 shows two typical pictures of interactions in the streamer chamber. Reflections off the wire electrodes from heavy ionization obscures the vertex in the top event while the vertex in the bottom event is relatively clear. The heavy tracks in the top event are fragments of the neon nucleus. The other tracks are from minimum ionizing tracks, except for the curved tracks which are knock-on electrons (δ rays).

3.2 The Neutron Beam

The beam was carefully designed to match the requirements imposed by the streamer chamber. The beam spot size at the streamer chamber entrance was designed to be 0.1 cm. x 1.0 cm. so that it would fit cleanly between the electrodes and inside the visible region of the chamber. At high rates ($\sim 10^6$ beam particles per second), more than one

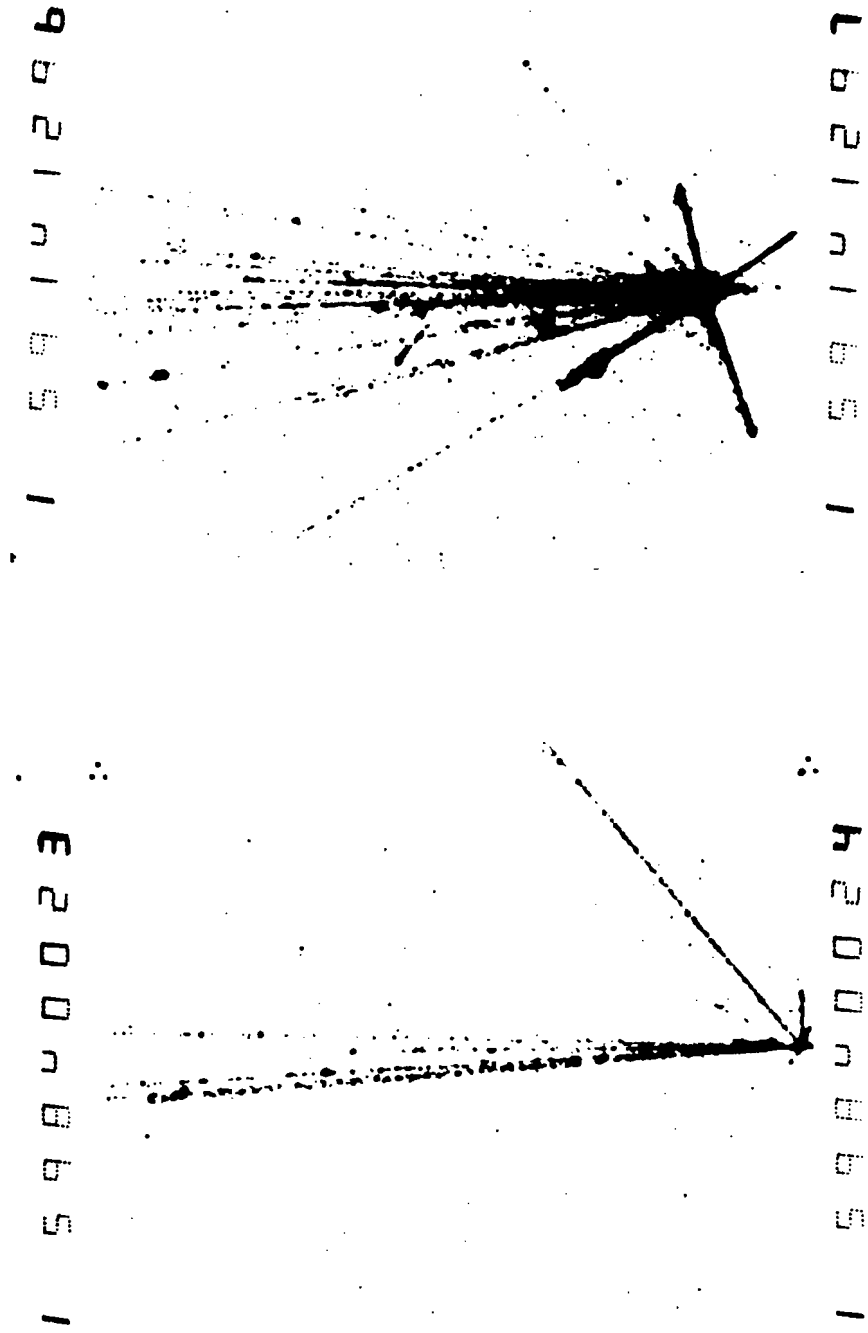

Figure 3-3: Two pictures from the streamer chamber

beam particle often traverses the streamer chamber within the memory time of the gas. In order to avoid visual obscurations from extra non-interacting beam particles, we chose a neutral beam.

A clean neutron beam with a small spot size was designed and built. The beam was made from a beam of 400 GeV protons focused onto a beryllium target. The target was embedded inside a large dump magnet. Charged particles were swept out of the forward channel by a 35 kgauss field and stopped by the steel of the magnet. Forward neutrals were allowed to pass through a 7 meter long channel. The downstream cross section of the channel was 1.0 mm. x 3.0 mm. The primary proton beam was focused on the 1.0 mm. x 0.1 mm. beryllium target at an angle of 0° with respect to the downstream channel. The channel holder was carefully surveyed and installed with utmost care to insure that there would be a clear straight path through the 7 meters of steel and brass. T. Cardello [43] describes a channel designed for charged particle selection in the same magnet. Fifteen small lead inserts (3.2 mm thick) were placed at intervals of 12.2 cm inside the channel to reduce the gamma content of the beam.

The neutron beam spot size was fixed by three collimators. Downstream of the large magnet there were three steel collimators each of length 5 feet. The schematic diagram of the beam channel and collimators can be seen in Figures 3-4. The inner dimensions of the collimators are given in Table 3-2. The collimators were first surveyed into place, but since their openings were so small, they were aligned with the neutron beam itself. Each collimator had a stepping motor at the front and rear that permitted remote vertical adjustment of the channel. The upstream-most collimator had a horizontal motor as well. Small beam monitoring stations were positioned after each collimator to measure the ratio of charged to neutral particles in the beam. By maximizing the neutral-to-charged ratio while adjusting the positions of the collimators, we were able to align the collimators and maximize the neutral content of the beam. The beam monitoring stations were also used to measure the neutron to gamma ratio in the beam. A diagram of the neutron beam can be found in Figure 3-5.

	distance from target (m)	horizontal aperture	vertical aperture
Beam Channel	0.00- 5.33	0.60 cm	1.50 mm
Beam Channel	5.33- 7.32	0.30 cm	1.00 mm
First Collimator	19.74-21.26	0.48 cm	0.45 mm
Second Collimator	30.24-31.76	0.72 cm	0.69 mm
Third Collimator	36.89-38.41	0.88 cm	0.85 mm
Fourth Collimator	39.60-42.00	1.43 cm	2.40 mm
Streamer Chamber	42.40		

Table 3-2: Neutron Beamline Channel and Collimators

Directly upstream of the streamer chamber tank, there was a small copper collimator. Neutral particles in the halo of the beam interacting inside the copper would produce charged particles that were detected in a scintillation counter just downstream. If there were any charged particles around the beam region, the event would be vetoed.

Figure 3-6 shows a Polaroid film image of the beam. The film was exposed at the entrance beam window of the streamer chamber, and shows the actual spot size of the beam. Table 3-3 gives the characteristics of the neutron beam.

A calorimeter was added to the end of the downstream apparatus to observe the energy of the particles in the beam. The beam passed through the hole in the spectrometer to the calorimeter made of scintillators sandwiched between layers of steel. The calorimeter was constructed of 6.0 absorption lengths of steel. The beam spectrum was analyzed for low beam intensity (2.3 X 10^{10} protons per pulse on target) to avoid pile-up in the counters. The measured energy spectrum was calibrated by assuming that the end-point of te spectrum corresponded to 400 GeV.

A picture of the neutron spectrum is shown in Figure 3-7. The curve fitted to the measured spectrum is described by L. Tzeng in Reference [112].

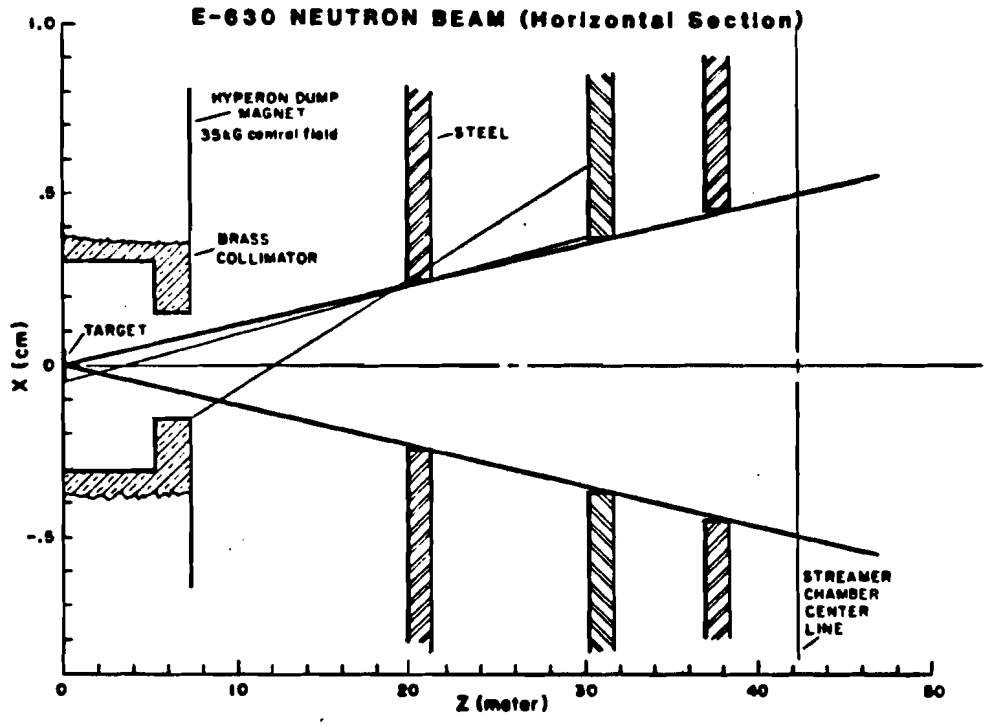

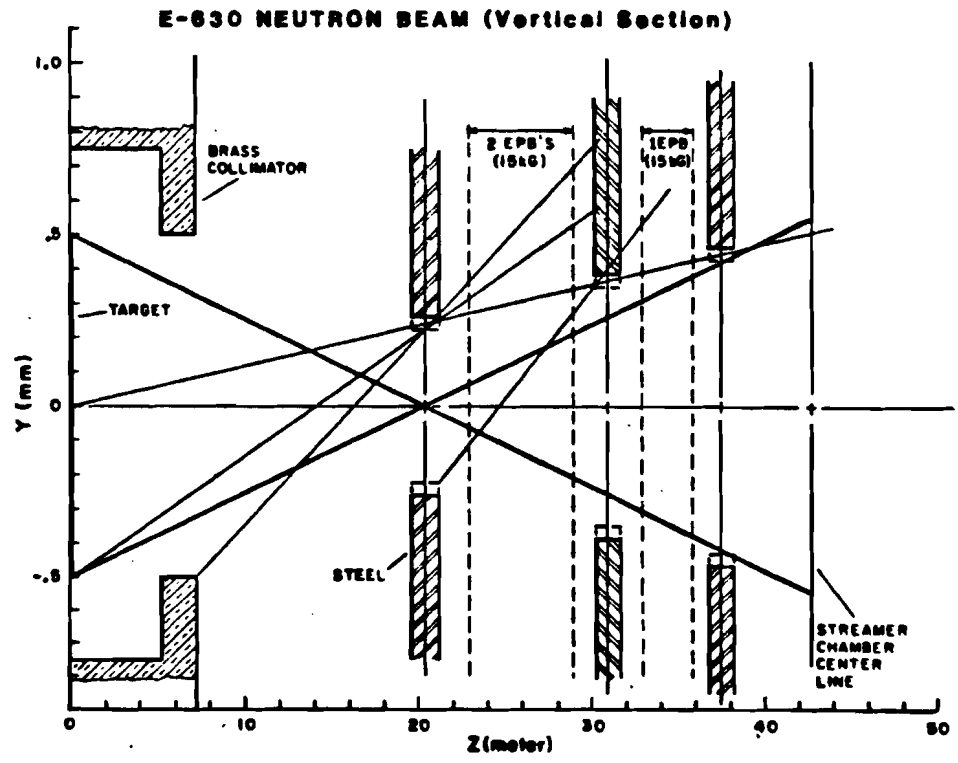

Figure 2-4: Schematic diagrams of the neutron beam

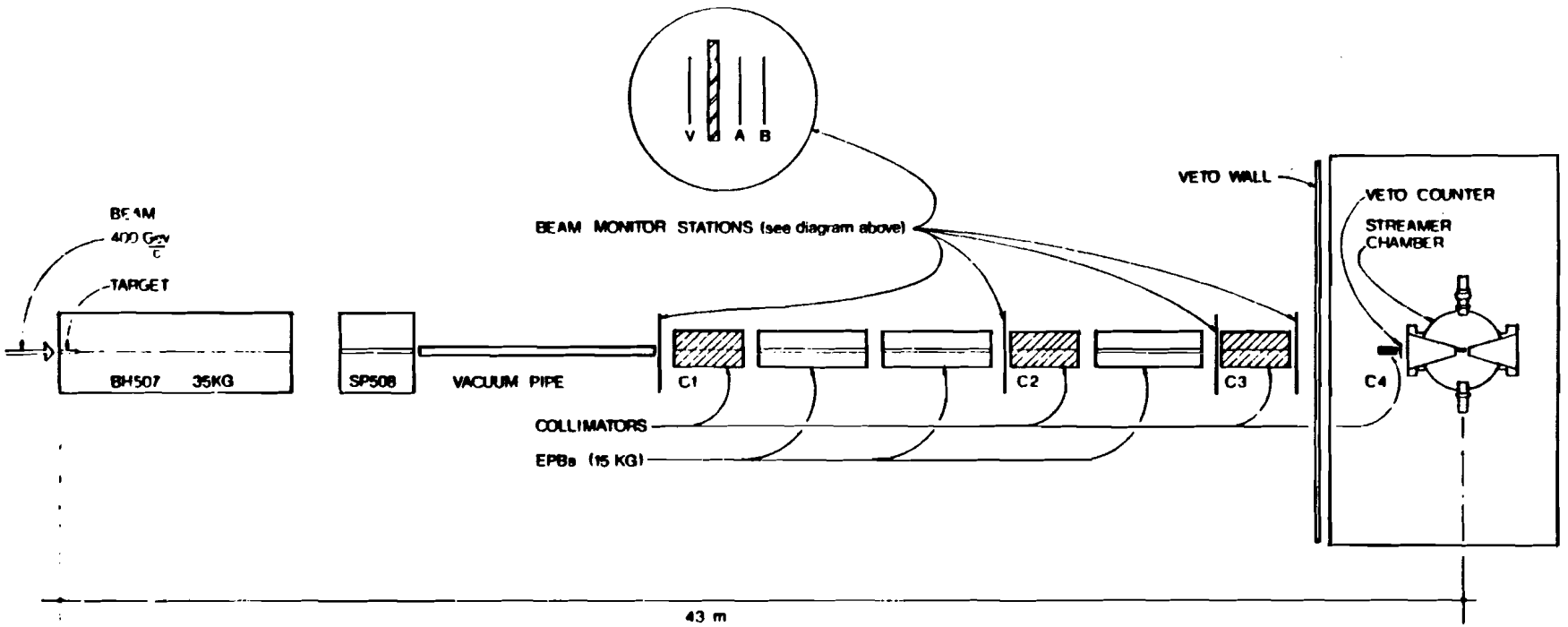

NEUTRON BEAM LINE

Figure 3-5: Layout of E-630 neuton beam

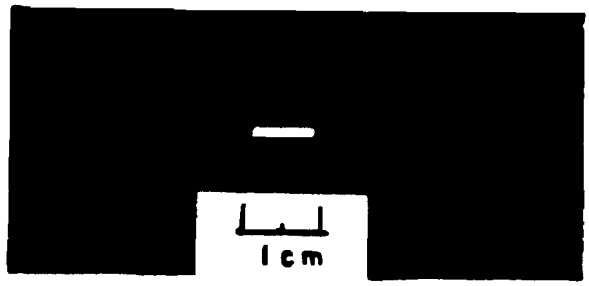

Figure 3-6: Image of the neutron beam at the entrance to the streamer chamber; actual size

Beam spot at chamber	9mm X 1mm
Protons/pulse on target	4.0×10^{11}
Neutrons/pulse at calorimeter	2.3×10^{6}
Average neutron energy	330 GeV/c
Beam halo	< 1%
Neutron/gamma ratio	80
Neutron / Neutral Strange Particle [112]	10^{4}

Table 3-3: Characteristics of the neutron beam

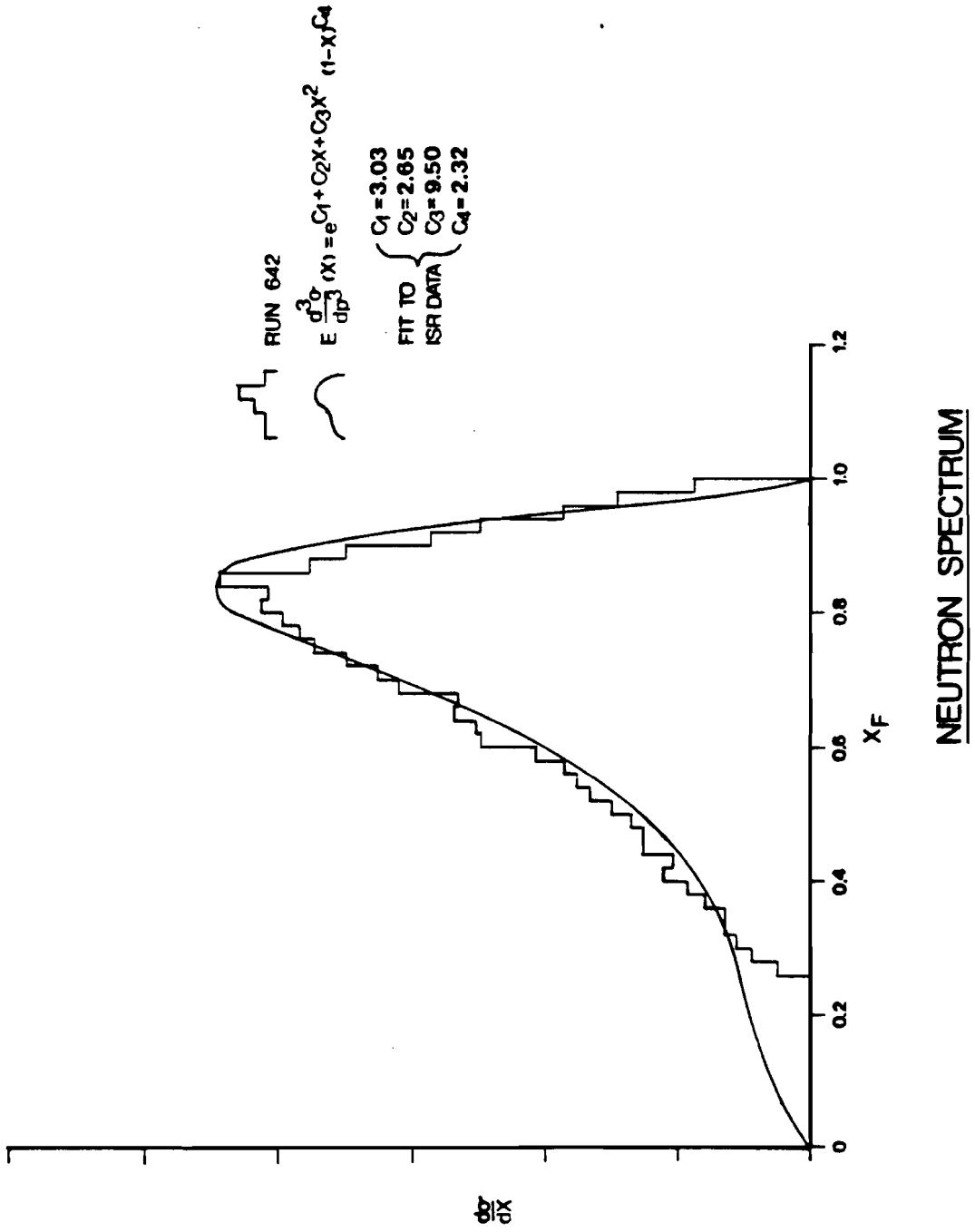

Figure 3-7: The neutron spectrum

3.3 The Downstream Spectrometer

The downstream spectrometer acted as a hadron filter as well as a muon identifier and analyzer. The basic components were 29.8 interaction lengths of steel and concrete covering the region between 30 mrad and 250 mrad in the laboratory including two toroidal magnets, scintillation counters for triggering and three cathode readout proportional wire chambers for muon tracking. The minimum energy necessary for a muon to traverse the spectrometer from the streamer chamber to the last trigger counter was 6.5 GeV. The forward region between 0 and 30 mrad was kept free of material and counters, allowing the beam and forward interaction products to pass through to the neutron calorimeter. The acceptance of the spectrometer was excellent for muons with momentum greater than 8 GeV/c and lab polar angles between 30 and 120 milliradians (see Figure 3-8). A drawing of the apparatus is given in Figure 3-9.

The trigger system was designed so that it was possible to trigger on streamer chamber interactions with muons, ordinary streamer chamber interactions or background muons from upstream beam interactions. In front of the streamer chamber, there was a wall of counters for vetoing chamber interactions occurring in coincidence with a charged track from upstream. Two small veto counters were placed in front of the streamer chamber in order to veto particles in the beam halo that might interact in the streamer chamber electrodes. Interactions in the streamer chamber volume were identified by a two fold coincidence in a pie shaped array of eight small counters just outside the downstream beam window of the streamer chamber. A muon trigger was defined by hits in a straight path through walls of counters upstream of the toroids, in coincidence with a hit in any of the counters behind the toroids.

3.3.1 The Hadron Shield

The steel shield was designed to act as a hadron filter to stop high energy particles, mostly pions, generated in interactions inside the streamer chamber. Furthermore, the shield was designed to keep first generation pions from the interactions from decaying in flight into a muon. This problem was studied by Michael Dine [53, 54] for the design of

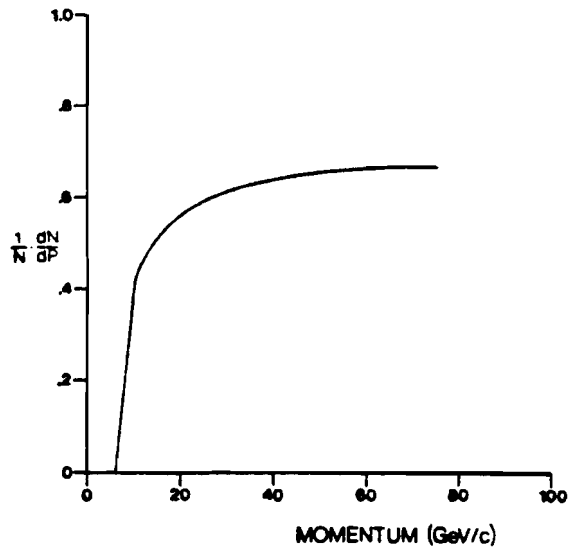

a) ACCEPTANCE

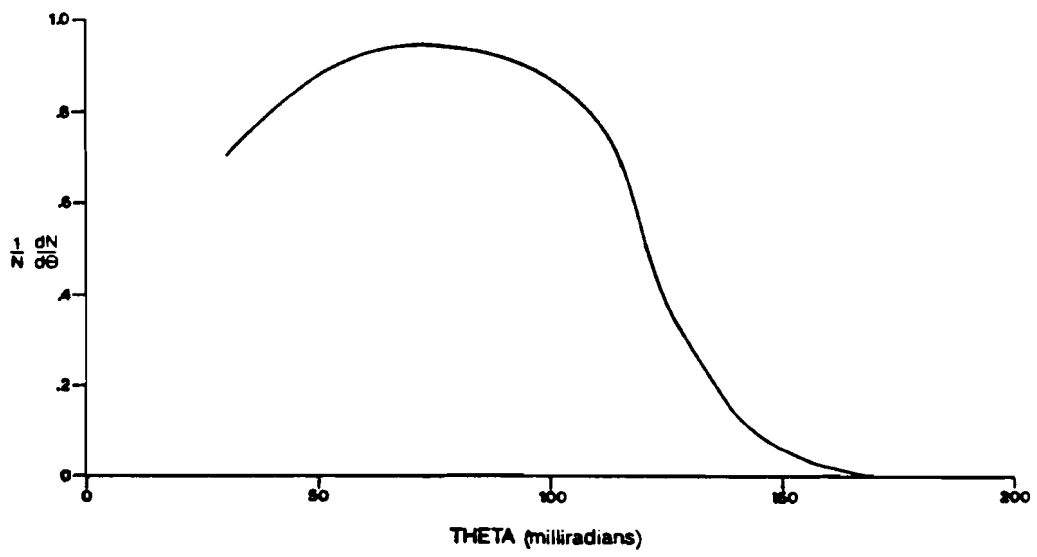

b) ACCEPTANCE

Figure 3-8: Acceptance for charm decay muons for a) momentum and b) polar angle θ

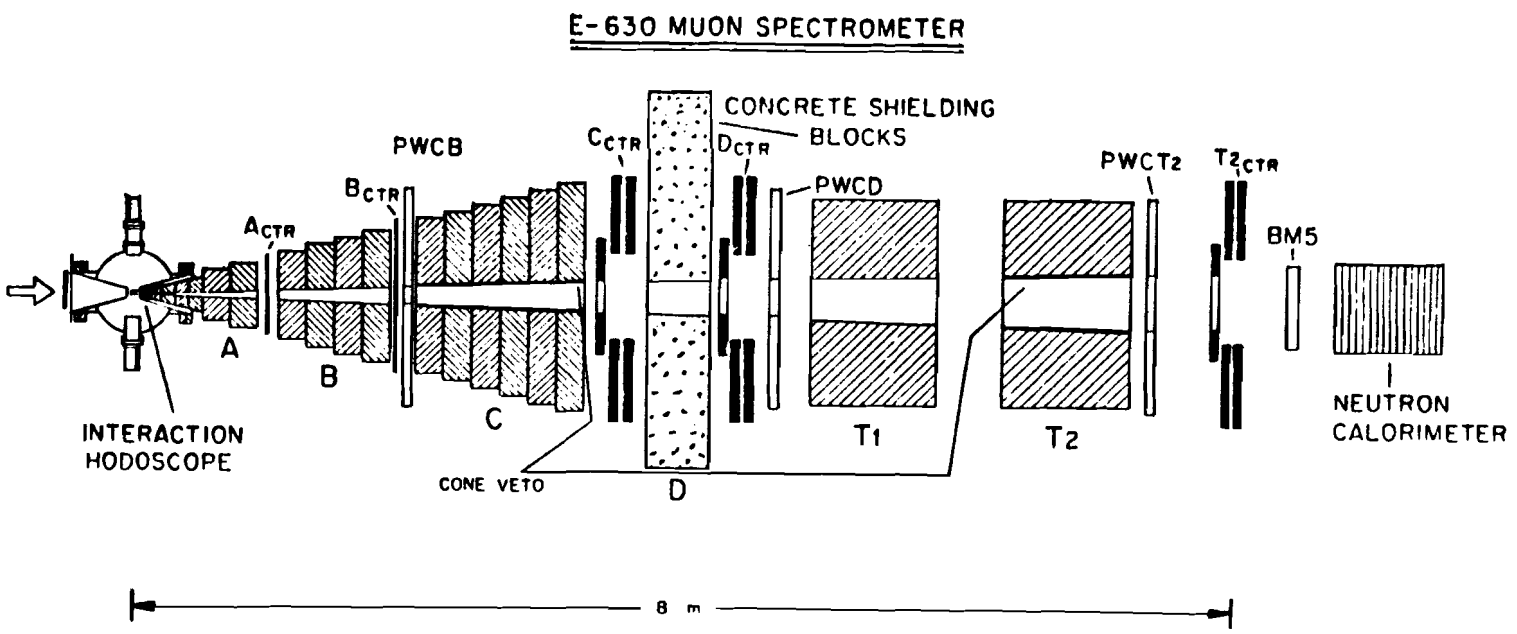

Figure 3-9: Drawing of the E-630 Spectrometer

FNAL experiment E-490 [102] It was most important to locate the steel as close to the streamer chamber as possible; hence, the upstream-most block of steel was made with a snout that extended to within 9 cm of the streamer chamber center.

Still the muons from secondary pion decay and the punch-through of secondary hadrons generated in showers inside the steel remained as a limitation of the trigger. Despite the thirty interaction lengths of steel, the majority of the muon triggers were from normal non-charmed inelastic collisions. We expect that for a 20 μbarn cross section for charm, 5% of the triggers are actually from charm decay muons. This is estimated from the measured trigger rates and the Monte Carlo acceptance for charm. The shield was designed to reduce the muon rates from pion decay and to reduce the hadronic punch-through while allowing a high acceptance of muons from heavy quark decays.

The shield was initially built in three sections, each with a conical hole that would allow beam particles and fast forward secondaries to pass unscattered and undetected. The upstream-most section, section A, was built with a 22 mrad central hole with apex at the upstream edge of the streamer chamber while the others were left with holes of 30 mrad (See Figure 3-10) with apex at the streamer chamber center. Gaps between the steel sections were made for the trigger counters and wire chambers. The hole of the third section was lined with a conical scintillation counter used to veto interactions with secondaries crossing the hole.

The shield with the addition of a concrete wall behind the steel was used successfully in E-490, the earlier charm experiment. The minimum momentum required of a muon that would pass through the shield in this configuration was 3.5 GeV/c. The addition of the two steel toroids to measure the muon momentum raised this minimum to enhance to about 6.5 GeV. The central hole of the second toroid was lined with a conical counter that vetoed muons that curled into the 30 mrad hole.

One of the major difficulties with this closed geometry detector was the multiple scattering and energy loss of the muons inside the steel. Each trigger muon must have passed through 280 radiation lengths before exiting the apparatus. Despite the fact that

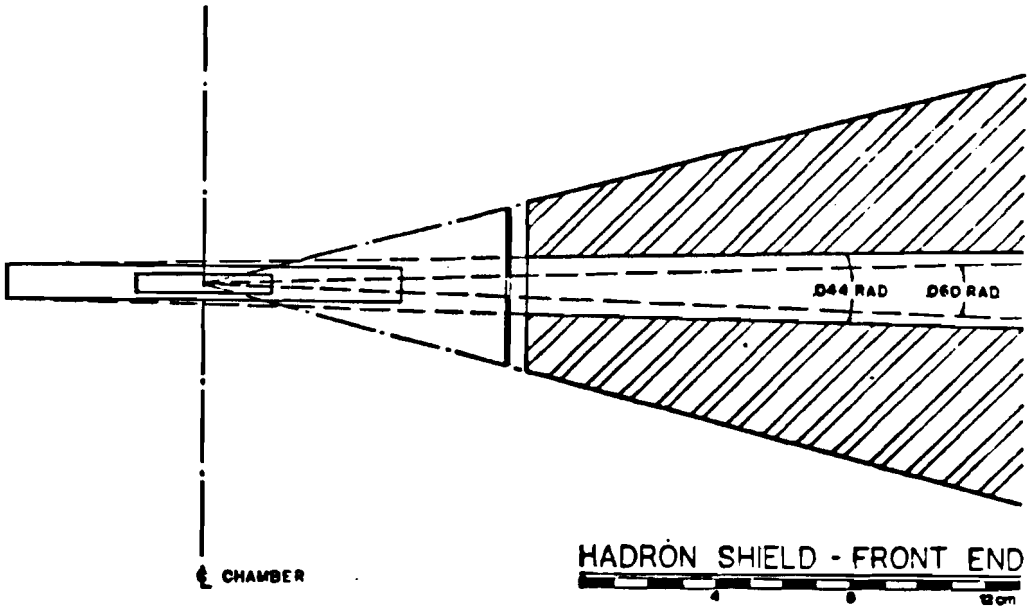

Figure 3-10: Cross Section of the first section of the Hadron Shield

the PWC resolution was not small (~0.6 cm), the multiple scattering set the limits on the resolution of the muon momentum.

3.3.2 The Toroids

The toroidal magnets, rebuilt from laminations of the Cosmotron C-magnets, had a total $\int B \cdot dl$ of 30 kg·m. The outer radii of the two toroids was 91.4 cm (3 ft), and the inner hole was a conical cone of angle of 30 mrad. The toroids' inner cones were machined into disks ten centimeter thick and which were then welded together. Each toroid had two copper coils with ten turns each. For each ten centimeter magnet section a keystone was made to complete the steel circle. Inserted alongside each pair of keystones was a circuit board imprinted with six 4 in. x 7 in. copper loops for measuring the magnetic flux and six Hall probes. One Hall probe on each toroid was instrumented through the beam line controls system so that we could monitor the field on-line. Figure 3-11 shows one of the toroids with the keystone inserts.

The field inside the toroid was measured in forty-eight positions using the loops.

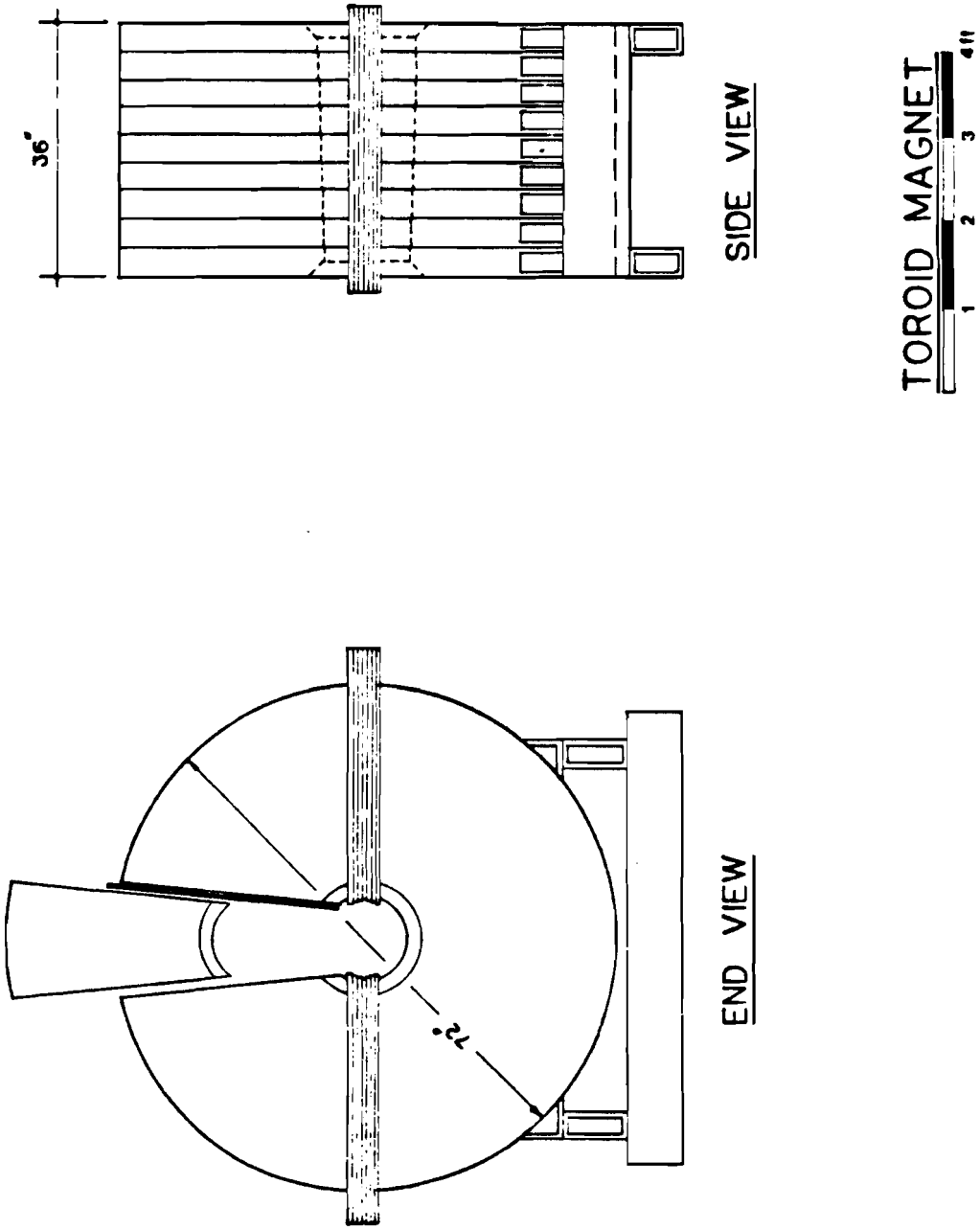

Figure 3-11: Steel toroidal magnet used in muon spectrometer

These measurements were performed by ramping the magnet current from saturation in one polarity to saturation in the other and observing the changing magnetic flux.

$$\oint_{\text{loop}} [\ \text{EMF dl}\ ] = \frac{\partial \Phi_B}{\partial t} = \text{Area} \times \frac{\partial B}{\partial t}$$

The time integral of the EMF around a circuit loop was measured for each of four steps in current(max.→0, 0→min, min.→0, 0→max) in order to obtain the field values at maximum and minimum current. A documentation of integration techniques can be found in Reference [89]. The field measurements, taken in eight groups, were fit to a third order polynomial as a function of radius. This process was repeated for each pair of ten centimeter thick disks. The measured field ranged from 14 Kgauss at the outside edge to 16 Kgauss at the center of the toroid.

The resolution of the momentum measurement using the toroid is limited by the multiple Coulomb scattering in the steel. An estimate of the resolution $\Delta p/p$ can be found by considering the projected root mean squared scattering angle divided by the deflection of a muon traveling a distance l (in meters) through a magnetic field **B**.

$$\frac{\Delta p}{p} = \frac{1}{2}\frac{1}{B}\ \frac{1}{\sqrt{l\,L_R}}$$

For muons with momentum less than 20 GeV/c, the momentum resolution is dominated by the multiple scattering error and the estimate of the resolution is 17 percent. Other effects limiting the resolution such as the measurement error will be considered later.

3.3.3 The Trigger Counters

Banks of large and small scintillation counters were used to form the trigger for the streamer chamber. Counters placed in front of the chamber were used to veto beam halo and non-fiducial interactions. Downstream of the streamer chamber, counters signaled the presence of interactions inside the fiducial volume or high energy muons originating near the chamber. The logic of the trigger system will be explained in more detail later.

Eight small scintillation counters were placed just downstream of the streamer chamber. These counters were used to select interactions in the region of the streamer

chamber. Each counter was cut in a wedge shape and the eight were mounted on the front end of the steel nose of the hadron shield in a pie-like formation. A hole was left to allow the non-interacting beam particles to pass.

Upstream of the streamer chamber house, counters were mounted to act as vetos of particles from upstream interactions. These counters covered a region 6 ft. x 6 ft. with a 2 inch hole for the beam. Just upstream of the streamer chamber, two more veto counters were installed to veto events with charged particles that might interact in the beam flanges or streamer chamber electrodes.

The counters installed inside the holes of the third steel section and the second toroid vetoed events in which any particle crossed into (or out of) the hole. In the region of the toroid this eliminated events in which the muon curled into the toroid hole. The veto in the third section eliminated events with any particle that crossed the hole. The effect was to eliminate confusing track patterns and hadrons which could cause fake muon triggers. Figure 3-12 shows a diagram of the trigger counters with the steel removed.

The muon trigger was set up to select events with a charged particle that passed through the iron of the hadron shield to the downstream end of the second toroid. In order to limit the background due to accidental hits and muons produced upstream of the streamer chamber, five banks of scintillators were positioned between the steel sections and behind the toroid. The first, positioned after the first steel section, was a single counter cut to match the area of the downstream face of the steel. A hole was cut in the counter to match the hole in the steel. The second set was positioned at the back of the second steel section. This bank was segmented vertically and contained four counters. The overall size was determined by the face of the second steel section, and a half-hole was cut into the center two as well. The third, fourth and fifth sets, before and after the concrete wall and after the toroid, were arrays of six 2 ft. x 3 ft. counters accompanied by central 2 ft. x 2 ft. counters into which 30 mrad holes were cut. The central east and west counters extended beyond the edge of the steel, so concrete shielding was added onto either side of the steel. In any event, this was of little consequence since the upstream

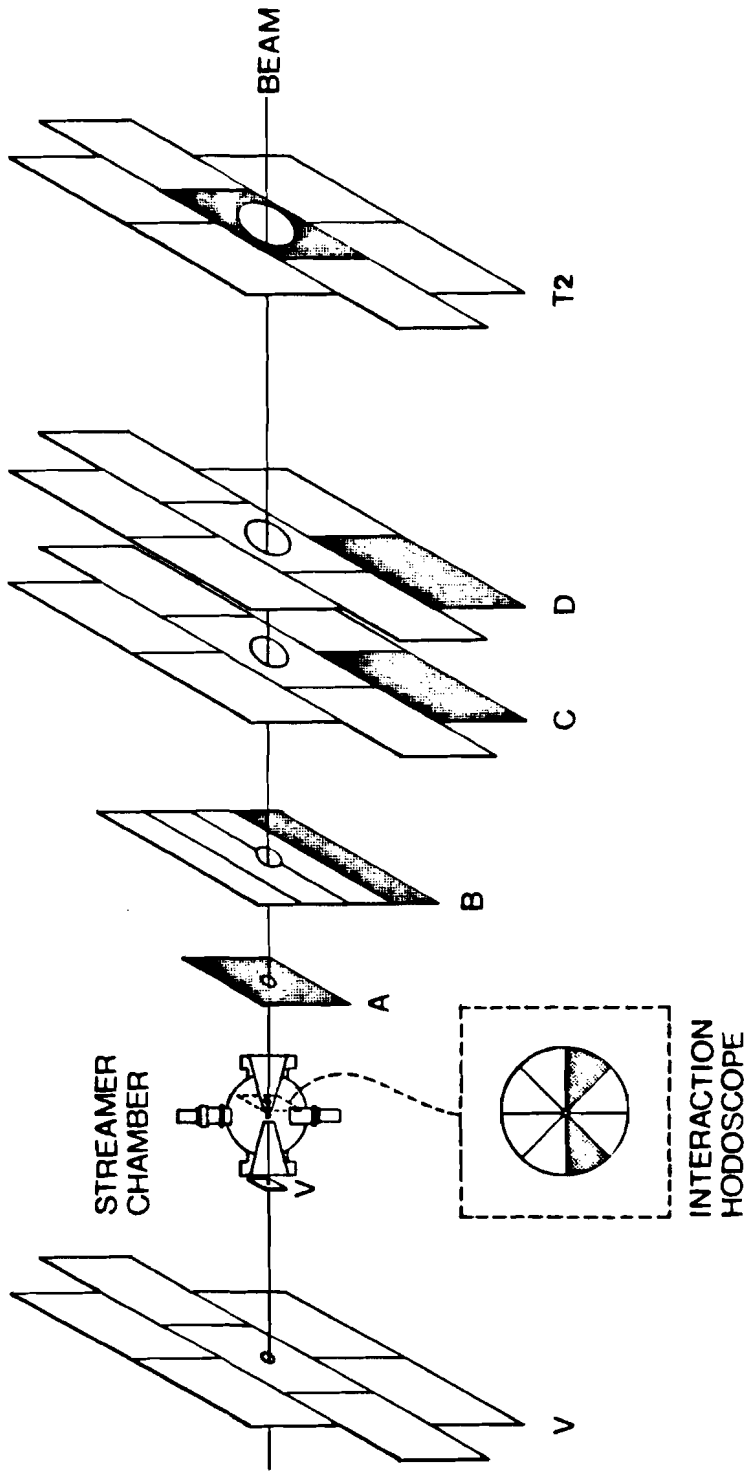

Figure 3-12: The trigger counters; the shaded region shows a muon trigger from an interaction

veto counters shadowed this region and the multiplicity of pions or muons from streamer chamber interactions was assumed to be small at these large angles.

Programmable high voltage power supplies were used for all of the trigger counters. The voltages could be set manually or through a CAMAC interface to the PDP11/34.[1] Lecroy 32 channel 4032A supplies with a serial CAMAC interface were used quite successfully for this purpose, although the microprocessors inside the units were not always reliable. This problem, however, did not affect the operation of the experiment.

3.3.4 Trigger Electronics

The main requirements of the trigger were speed and flexibility. Since the diffusion of the streamers was the limiting factor in the resolution, it was important that the trigger decision be made quickly. However, cables connecting the experimental hall with the counting room where the trigger logic was located were 150-200 nanoseconds long. Hence, we wanted to have the ability to move the electronics to the experimental hall so that it would be as close to the apparatus as possible. The hall was a high radiation area, so in order to have a flexible trigger in these conditions, we wanted a system that could be remotely controlled. The flexibility was needed because three separate triggers were used under normal running conditions, and beam studies, muon studies and early trigger studies required different triggers.

The electronics used in the trigger combined Lecroy ECLine discriminators, delay lines, coincidence units and logic units with more standard NIM electronics modules. The ECL units were CAMAC modules, and the discriminator thresholds, delay times and trigger logic functions could be controlled using Camac Diagnostic Language [45] on the on-line PDP11/34. This configuration allowed flexibility in the trigger and reduced the number of units and cables necessary to perform the task. Although it was not implemented, the programmable feature of the electronics permitted in principle a reduction in the total delay in triggering the streamer chamber by giving control over electronics in the experimental hall, which was inaccessible when the beam was on.

---

[1]PDP11/34: Digital Equipment Corporation

Outputs of the phototube bases were connected to the Lecroy 4416 ECLine discriminators inside the counting room. The shaped output pulses from the discriminators were sent to scalars, latches (Lecroy 4516 coincidence units) and to one of the three programmable logic units (Lecroy ECLine 4506). These units consisted of two sections, each with eight inputs and eight outputs. The 256 x 8 bit memory permitted us to select the logic functions AND, OR, exclusive OR, inhibit, multiply or any combination of these functions. Details of the trigger logic will be given in Chapter Four.

3.3.5 Proportional Wire Chambers

The proportional wire chamber system was designed to complement the closed geometry of the muon filter. The muon momentum spectrum for centrally produced charmed mesons when folded with the trigger acceptance showed that there would be relatively few muons with momentum greater than 30 GeV/c. The deflection caused by the multiple scattering of a 30 GeV/c muon travelling through 200cm of steel was predicted to be .7 cm. Three multiwire proportional chambers employing cathode readout were designed and built with this in mind. The chambers were designed to be sturdy and dense in keeping with the nature of the muon filter. The active area of each chamber was 160cm x 160cm with a deadened "massless" region in the center. Major design considerations were speed of construction and low cost while maintaining precise mechanical tolerances over the large planar distances. Each chamber had one anode wire plane and two striped planar cathodes. The anode wires were wound vertically, and the cathode planes were horizontally and diagonally striped. The anode wires and cathode strips were connected together to form 2 cm strips. The resolution of each plane, considering a uniform sensitivity for each strip, was predicted to be $R = 2\text{ cm} / \sqrt{12} =$ .58 cm.

Each wire chamber was constructed from two large aluminum frames supporting flat planes of craft paper honeycomb (hexcell) and sheet aluminum sandwiches. The inner sides of the sandwiches held large copper-clad printed circuit boards forming the chamber's cathode planes. The two sandwiches were bolted together around the outside

edge. The edge spacers between the two halves set the cathode-to-cathode spacing and held the O-ring for the gas seal.

The anode plane was made from 25 μm gold-plated tungsten wire wound at a tension of 50g. The wire spacing was 2mm and the anode-to-cathode spacing was 6.35 mm. The wires were soldered onto printed circuit boards in groups of five. One end of each group was connected to the high voltage supply through a 10 kΩ resistor. The other was connected through a 180pf capacitor to a preamplifier. The cathode strips were 4mm wide with 1mm gaps. The strips were connected together at one end into groups of two. The cathode planes were held at ground voltage. Five 75 μm silver-plated copper beryllium wires were laid on each edge of the wire planes to prevent discharges due to high field concentrations. The edges of the cathode planes were covered by G-10 (epoxy and fiberglass composite) bars.

The cathode planes were laminated onto the hexcell and aluminum sandwich. The laminating process was done on a large smooth granite block so that the cathode surfaces would be flat. For two of the chambers, the cathode planes were made from copper clad Kapton laminated onto phenolic boards. The strip pattern was etched onto 16 cm wide pieces of Kapton. These pieces were then accurately taped together to form a uniformly striped plane. The taped Kapton sections were rolled onto a bed of epoxy on a thin phenolic board. The results were satisfactory, although much time was spent patching the flaws in the surface caused by air bubbles, excess glue and uneven shrinkage of the Kapton during the etching process. The third chamber, made from the G-10 printed circuit boards, was easier to construct.

The anode wires were wound onto the diagonal cathode plane. Two accurately machined .250 inch support bars were epoxied to the top and bottom of the cathode plane. These bars also held the printed circuit boards to which the wires were glued and soldered. Two narrow bars were glued across the surface of the cathode plane to provide additional mechanical support. The wires were held to these bars with epoxy.

The central region of each chamber was deadened by cutting a hole in the cathode

plane. The supporting hexcell was removed leaving the central region inactive and massless. The gas seal was maintained by sheets of aluminized mylar stretched over the outside of the hole. A thick aluminum ring with well-rounded edges was inserted inside the hole so that the rounded edge was close to the sharp rim of the hole in the cathode. Despite this, the high field concentrations in this region caused difficulties. A 1/4 inch-thick G-10 ring was added to the top of the cathode planes to ease the problems. A thin sheet of mylar was stretched across the top of the ring to aid in deadening the anode wires [50]. A cross section of the region near the hole is shown in Figure 3-13.

Unfortunately the aluminum chamber frames were warped in the welding process. When the frames were bolted together the cathode planes bowed apart making the chambers inefficient in the center. By loosening the bolts and adding extra bracing to the outside and extra machined spacers to the inside, a uniform gap was achieved.

The chambers were tested for stability under high voltage and in beam conditions before the experiment. Tests were done to study the performance with several different gas mixtures. The mixture that was eventually used for the experiment was Argon mixed with 25% Ethane, 0.7% Freon-13B1 (CF_3Br) and 4.2% Methylal ($(OCH_3)_2CH_2$) [47]. The Argon-Ethane-Freon was purchased pre-mixed. A portion of the gas was bubbled through a tank of Methylal at 0 °C and fed through a mixing tube to combine it with the remainder of the gas. A schematic of the gas system is shown in Figure 3-14.

The operating voltage of each chamber was chosen to insure high efficiency on both the anode and cathode planes (~4200 V). As mentioned above, positive high voltage was applied to the anode wires while the cathodes were held at ground. The chambers were very efficient at their operating voltages, although the gas would often break down with high muon fluxes. We were able to cure this by connecting the power supplies to a control module that ramped the voltages to their operating values during the beam spill.

The readout electronics for the PWC's connected each input together into groups of two. The preamplifiers were mounted on the outside of the chambers. They supplied a gain of eight to both the anode and cathode signals and sent output pulses along flat

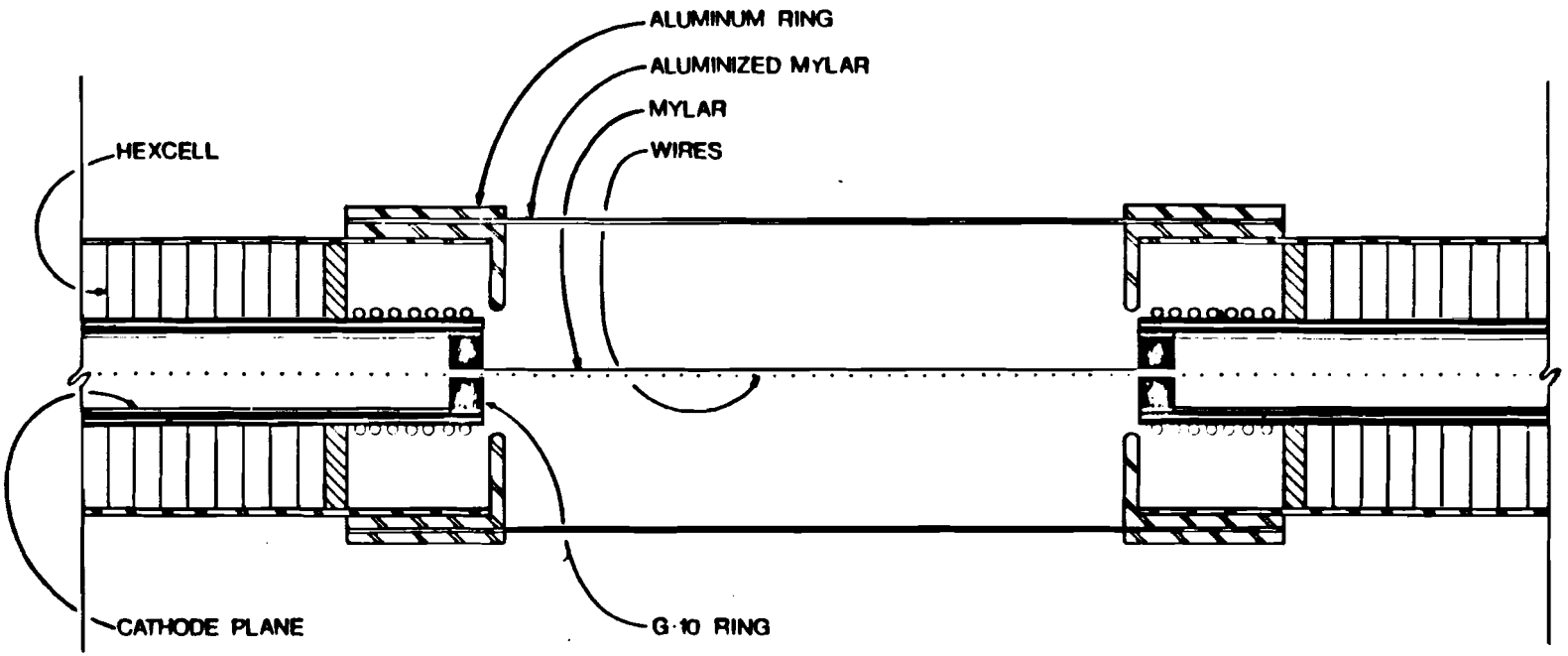

PWC CENTRAL HOLE
CROSS SECTION

Figure 3-13: Cross section of the hole in PWC D

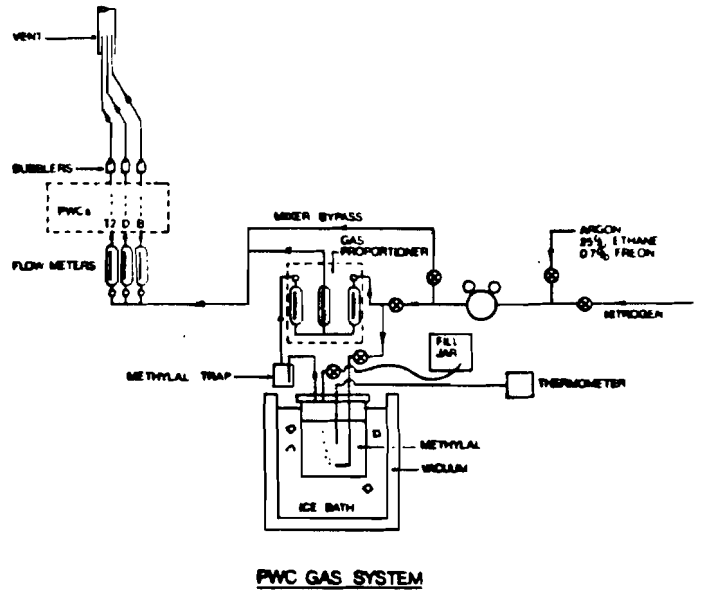

Figure 3-14: Schematic of the PWC Gas System

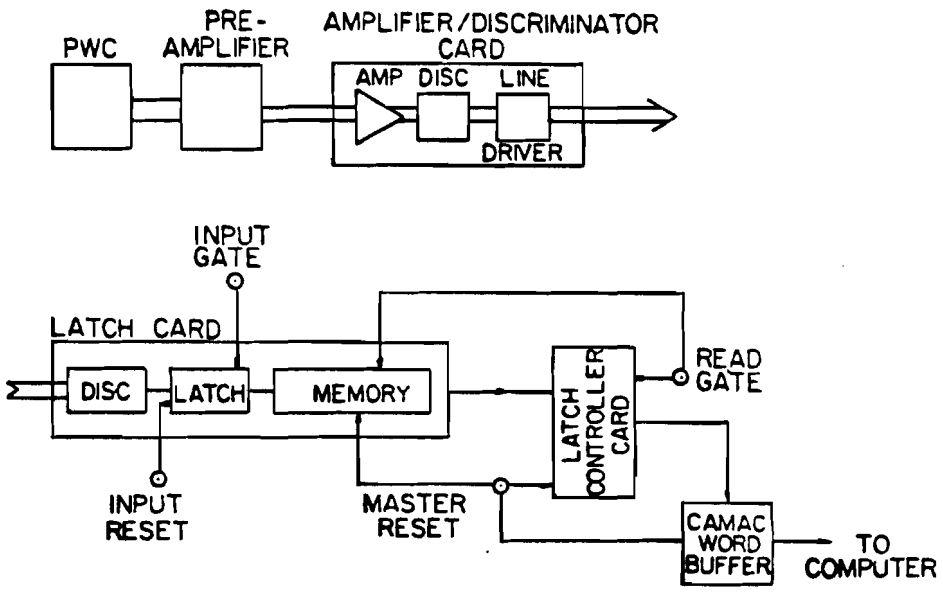

Figure 3-15: Diagram of the PWC Electronics

multiconductor shielded cables to the amplifier/ discriminators. The threshold setting of each channel was set to correspond to 0.25 mV (cathode) and 0.50 mV (anode) at the chamber, where the output signals were observed to be 5 mV and 25 mV respectively. TTL level pulses of width 60 nsec were then sent over 500 nsec of ribbon cable to latches in the counting house. The PWC information was stored in the latches for every trigger and then read by a word buffer [52] which was interfaced through CAMAC to the PDP11/34 (Figure 3-15). The PWC readout apart from the pre-amplifiers was the same as that used in Fermilab experiment E-497 [110].

3.4 Installation

The experiment was installed into the Proton Center experimental area of Fermilab in March of 1981. The streamer chamber was enclosed in a small shielded house to protect the sensitive electronics of the downstream apparatus from the electrical noise generated by the streamer chamber pulse forming network. The trigger electronics and computer were set up inside the counting house which was about 200 feet from the experimental hall. RG-8 foam cables were used for the trigger counter signal cables to minimize the trigger delay time (~700 nsec overall). The high voltage power supplies for the PWC's were also installed in the counting house. We found it necessary to install Reynolds connectors on type-C cable, since the standard high voltage (SHV) connectors were inadequate in the damp conditions of the Proton Center pit.

By April the channel was installed inside the large magnet, and we were able to begin beam studies. The following two months were spent studying muon rates and beam quality. We were able to collect enough pictures and muon data during this engineering run to test the apparatus and to develop the off-line analysis.

Chapter 4

DATA ACQUISITION

The experiment was installed at Fermilab during the spring of 1981. Before the beam was turned off for the summer, we were able to test the apparatus and study the neutron beam. In January of 1982, we began data acquisition. This phase of the experiment was completed in March of 1982. A total of 217,506 streamer chamber pictures were taken, of which 157,508 were taken with the charm-enhancing trigger. The muon trigger enhanced the probability of triggering on an interaction producing a pair of charmed particles relative to the probability of triggering on a normal interaction by approximately a factor of 40. From the collected data, we were able to isolate a sample of interactions rich in charmed particles for further study.

4.0.1 The Trigger

The trigger was set to activate the streamer chamber when the signature of a muon was observed in the downstream counters in coincidence with an interaction in the region of the streamer chamber. In order to explain the trigger requirements, it is best to break the trigger into parts and explain each part separately.

N	The requirement that there were no hits in the counters upstream of the streamer chamber, either in the muon veto wall or in the beam halo vetos.
I	Two or more segments of the interaction hodoscope must have fired to fulfill this trigger requirement.

$\overline{CV}$ This part of the trigger vetoed events with hits in the conical counters lining the central holes of the third section of the hadron shield and the second toroid.

MU Hits were required in the A, B, C, D and T2 counters. There was a tracking requirement on the hits upstream of the toroid.

The A wall was not segmented and was required for every track.

For the B wall, the tracking separated hits in the upper half, middle half and lower half.

The C and D walls were segmented into seven segments. In order to satisfy the trigger, the corresponding counters in the C and D wall must have fired. The hit in the B wall dictated whether the hits in C and D could be in the upper, middle or lower third of the wall.

No tracking requirement was imposed on the T2 wall. A hit in any one of the counters was sufficient.

A hole was cut from the central region of each wall of counters corresponding to a 30 milliradian angle about the beam line and pointing to the center of the streamer chamber.

Thus the charm enhancing trigger will be referred to as the NI$\overline{C}\overline{V}$MU . Figure 3-12 shows the trigger counters and a sample NI$\overline{C}\overline{V}$MU event. Notice that the segmentation of the counter tracking system is coarse enough to accommodate the multiple scattering of the muons in the steel.

The trigger was highly selective, yielding only one trigger for every 10^4 interactions in the streamer chamber. The addition of cone veto counters cut the interaction trigger rate by a factor of five, giving the rate of NI$\overline{C}\overline{V}$MU/NI$\overline{C}\overline{V}$ of 5 X 10^{-4}. Monte Carlo calculations indicated that the acceptance rate for charmed mesons, assuming an average semi-leptonic branching ratio of 8.0% and central production, was 2.0%. This gave us an enhancement for charm of 40. The dependence of the acceptance on the production and decay models is discussed by L. Tzeng in Reference [112]. For reasonable models, the acceptance varies from 1.5% to 3.5%.

4.0.2 Background Triggers

Background triggers, NI$\overline{C}\overline{V}$ in the code given above, were taken for studies of pictures of non-charm interactions. These events would prove to be very valuable in the final film analysis. The pictures of normal interactions were used to calibrate the film measuring

machines and to test the vertex fitting procedures during the film analysis. Simple MU triggers were recorded as well, but only on tape. We studied the muons from these events to determine chamber resolutions, alignments and efficiencies.

4.0.3 The Trigger Logic

The major components of the trigger logic electronics were the Lecroy ECL discriminators, coincidence units, delay modules and programmable logic units. As described in Chapter Three, the logic defining the trigger was implemented inside the programmable logic units (PLU). The logic functions performed by each channel could be set through a Fortran program. The Fortran subroutine PLU provided the logical relation between the inputs and the outputs. Each unit had eight inputs and eight outputs that could be independently programmed. The program PLUFOR assembled the logic functions into actual code needed to program each unit. Figure 4-1 shows a listing of the Fortran subroutine used to define the logic functions of the trigger PLU's.

The overall logic scheme is given in Figures 4-2 and 4-3. The latches and scalars are represented by the code letters L and S. The upstream muon tracking was performed by the coincidence unit shown in Figure 4-2. Also shown, are the PLU's used to select events with I>2 and T2>1. The other PLU in Figure 4-2 performs the logic function OR on all the upstream veto counters. The OR of the cone veto counters was performed by more conventional NIM logic units.

The compilation of the various parts of the trigger was performed in the PLU shown in Figure 4-3. In this diagram, note the separation between all events written on tape [event] and all events with tape and film [trig]. The gate code controlled the trigger selection to enhance the live time.

```
@PLU                                                    27-MAY-91  20:48:30
      SUBROUTINE PLU(IPLU)
C
C     SUBROUTINE TO DEFINE THE CONTENTS OF EACH PLU MEMORY
C     LOCATION.
C
C     INPUTS  NAME    TYPE              RANGE
C             IPLU    INTEGER*4         PLU NUMBER (0 < IPLU < NPLU+1)
C             INPUT   INTEGER*4         0 - 255
C             IN(K)   LOGICAL*1         TRUE (-1) OR FALSE (0)
C                                       K = BIT 0 (0 < K < 8)
C
C     OUTPUTS NAME    TYPE              RANGE
C             OUTPUT  INTEGER*4         0 - 255
C                                       IF OUTPUT IS SET THEN
C                                       OUT(K) VALUES ARE IGNORED.
C             OUT(K)  LOGICAL*1         TRUE (-1) OR FALSE (0)
C                                       K = BIT 0 (0 < K < 8)
C
C     THE VARIABLE NPLU SHOULD BE SET WITH A DATA STATEMENTS
C     TO DEFINE THE NUMBER OF PLU'S TO DO.
C
C     --->    NOTE THAT ALL VARIABLES IS THIS PROGRAM ARE
C             IMPLICITLY LOGICAL*1 EXCEPT (I, J, K, L, M, N).
C
C             PETE COOPER             12-JAN-91
C
C--->  SPECIFICATION STATEMENTS
C
      IMPLICIT LOGICAL*1 (A-Z)
      INTEGER I,J,K,L,M,N,IPLU
C
      COMMON /BITBK/NPLU,INPUT,IN(8),OUTPUT,OUT(8)
      INTEGER NPLU,INPUT,OUTPUT
      LOGICAL*1 IN,OUT
      DATA NPLU/ 8/
C
C--->  PROCEDURE STATEMENTS
C
      GOTO (100, 200, 300, 400, 500, 600, 700,800),IPLU
C
C     PLU ONE - INTERACTION HODOSCOPE - DEMAND COUNT > 1
C
C     MODIFIED TO REQUIRE 2 - 8 TRACKS - USER SELECTABLE
 100  J=0
        DO 150 I=1,8
        IF(IN(I)) J=J+1
 150    CONTINUE
      IF(J.LT.2) GOTO 190
      OUT(1)=.TRUE
      OUT(2)=.TRUE.
      IF (J.LT.3)GO TO 190
      OUT(3) = .TRUE.
      IF (J .LT. 4) GO TO 190
      OUT(4) = .TRUE.
      IF (J .LT. 5) GO TO 190
      OUT(5) = .TRUE.
      IF (J .LT. 6) GO TO 190
      OUT(6) = .TRUE.
      IF (J.LT. 7) GO TO 190
      OUT(7) = .TRUE.
      IF (J .LT  8) GO TO 190
      OUT(8) = .TRUE.
```

1

```
 190  GOTO 1000
C
C     PLU TWO - UPSTREAM VETO - SET OUTPUT IF ANY COUNTER SET
C
 200  VETO=INPUT .NE  0
      OUT(1)=VETO
      OUT(2)=VETO
      GOTO 1000
C
C     PLU THREE - T2 TRIGGER - DEMAND AT LEAST ONE HIT
C
 300  MVUT2=IN(1)
      MEUT2=IN(2)
      MVMT2=IN(3)
      MEMT2=IN(4)
      MVLT2=IN(5)
      MELT2=IN(6)
      MMUT2=IN(7)
      MMLT2=IN(8)
      T2=INPUT .NE. 0
      OUT(1)=T2
      OUT(2)=T2
      GOTO 1000
C
C     PLU FOUR
C
 400  MUUB=IN(1)
      MUMB=IN(2)
      MLMB=IN(3)
      MLLB=IN(4)
      MA  =IN(5)
      OUT(1)=(MUUB .OR. MUMB) .AND. MA
      OUT(2)=OUT(1)
      OUT(3)=(MUMB .OR  MLMB)  AND. MA
      OUT(4)=OUT(3)
      OUT(5)=(MLMB .OR  MLLB) .AND. MA
      OUT(6)=OUT(5)
      OUT(7)=(MUMB .OR. MLMB)  AND. MA
      OUT(8)=OUT(7)
      GOTO 1000
C
C     PLU FIVE - TRIGGER
C
 500  V=IN(1)
      INT=IN(2)
      MU=IN(3)
      T2OR=IN(4)
      CV=IN(5)
      SR=IN(6)
      I=-(2*IN(8)+IN(7))
      OUT(1)=MU .AND  T2OR
      OUT(2)=( NOT.V)  AND. INT
      OUT(3)=( NOT.V)  AND. INT .AND. (.NOT.CV)
      OUT(4)=( NOT.V) .AND. INT .AND. T2OR .AND. MU
      OUT(5)=( NOT V) .AND  INT AND.MU  AND. T2OR  AND. (.NOT.CV)
      OUT(6)=MU  AND  T2OR .AND. (I EQ 2)
      OUT(7)=OUT(3) .AND  (I EQ 1)
      OUT(8)=OUT(5) .AND  (I EQ 0)
      GOTO 1000
C
C     PLU SIX - GATES
C
 600  BG=IN(1)
```

2

Figure 4-1: The Fortran subroutine that defined the logical functions of the PLU's

```
      SR=IN(2)
      NICVB=IN(3)
      MUG=IN(4)
      NOTCH=IN(5)
      SCGATE=BG .AND. (.NOT.SR) .AND. (.NOT.NOTCH)
      J=9
      IF(SCGATE) J=0
      IF(SCGATE .AND. NICVB) J=1
      IF(SCGATE .AND. MUG) J=2
      OUT(1)=SCGATE
      OUT(2)=SR
      OUT(3)=NICVB
      OUT(4)=MUG
      OUT(5)=NOTCH
      OUT(7)=(J AND.1) .NE. 0
      OUT(8)=(J.AND.2) .NE. 0
      GOTO 1000
C
C     PLU SEVEN -( OLD MUON TRIGGER
C
 700  U1 = IN(1)
      E1 = IN(2)
      L1 = IN(3)
      V1 = IN(4)
      U2 = IN(5)
      E2 = IN(6)
      L2 = IN(7)
      V2 = IN(8)
C
      UP   = U1 .OR. U2
      EAST = E1 .AND. E2
      DOWN = L1 .AND. L2
      WEST = V1 .AND. V2
      MU   = UP .OR. EAST .OR. DOWN .OR. WEST
      QUAD = ( UP .OR. DOWN ) .AND  ( EAST .OR. WEST )
C
      OUT(1) = MU
      OUT(2) = QUAD
      OUT(3) = UP
      OUT(4) = EAST
      OUT(5) = DOWN
      OUT(6) = WEST
      OUT(7) = 0
      OUT(8) = 0
C
      GOTO 1000
C
 800  V=IN(1)
      INT=IN(2)
      MU=IN(3)
      T2OR=IN(4)
      CV=IN(5)
      SR=IN(6)
      I=-(2*IN(8)+IN(7))
      OUT(1)=MU .AND. T2OR
      OUT(2)=(.NOT.V) .AND. INT
      OUT(3)=(.NOT.V) .AND. INT .AND. (.NOT.CV)
      OUT(4)=(.NOT.V) .AND. INT .AND. T2OR .AND. MU
      OUT(5)=(.NOT.V) .AND. INT.AND.MU .AND. T2OR .AND. (.NOT.CV)
      OUT(6)=V
      OUT(7)=OUT(3) .AND. (I.EQ.1)
      OUT(8)=OUT(5) .AND. (I.EQ.0)
      GOTO 1000
```

3

```
C
C
C--->   END STATEMENTS
C
 1000   RETURN
        END
```

4

Figure 4-1: Continued

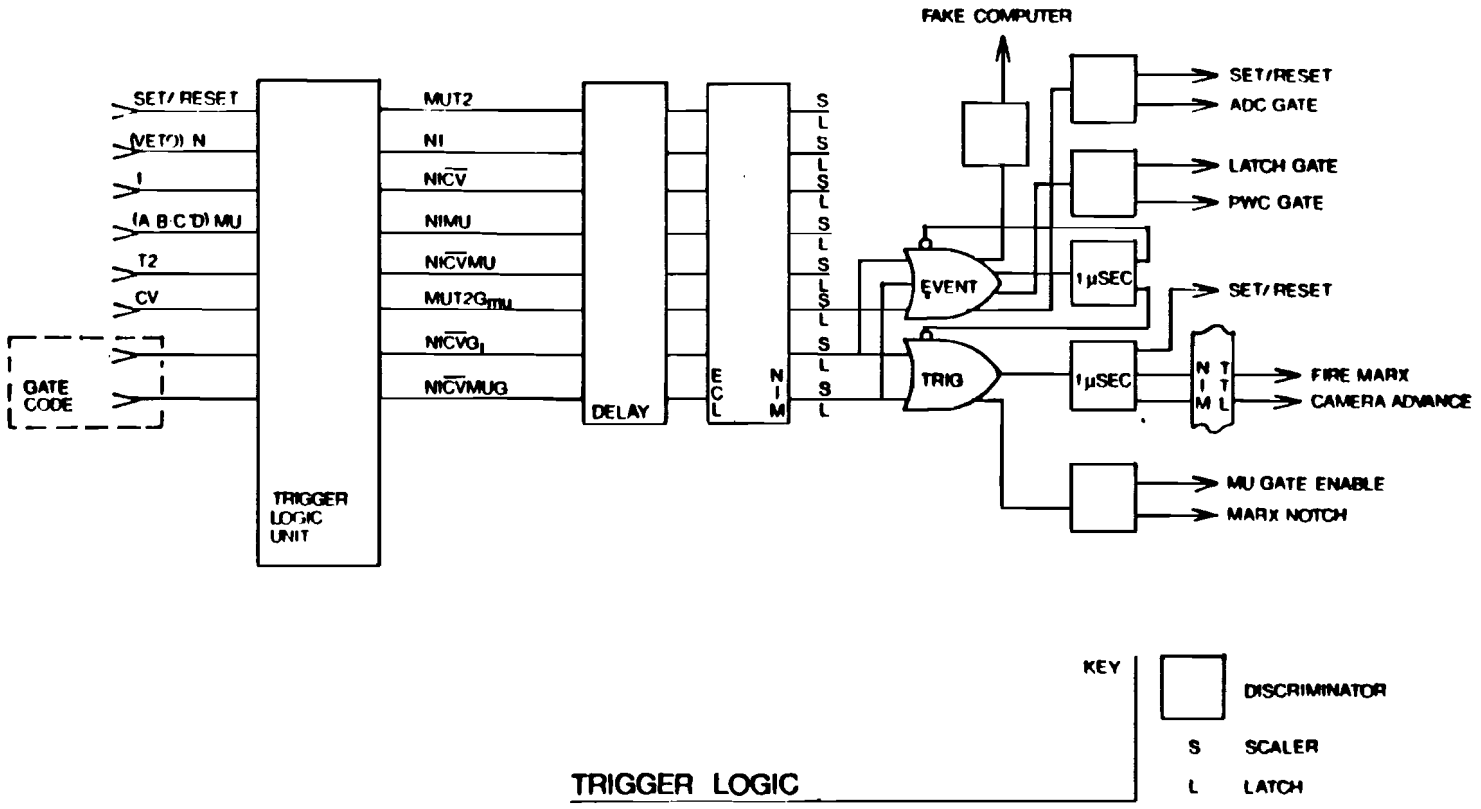

Figure 4-2: The Trigger Logic Diagram, Part I: This shows each logic path for the trigger requirements N,I,CV,MU,and T2.

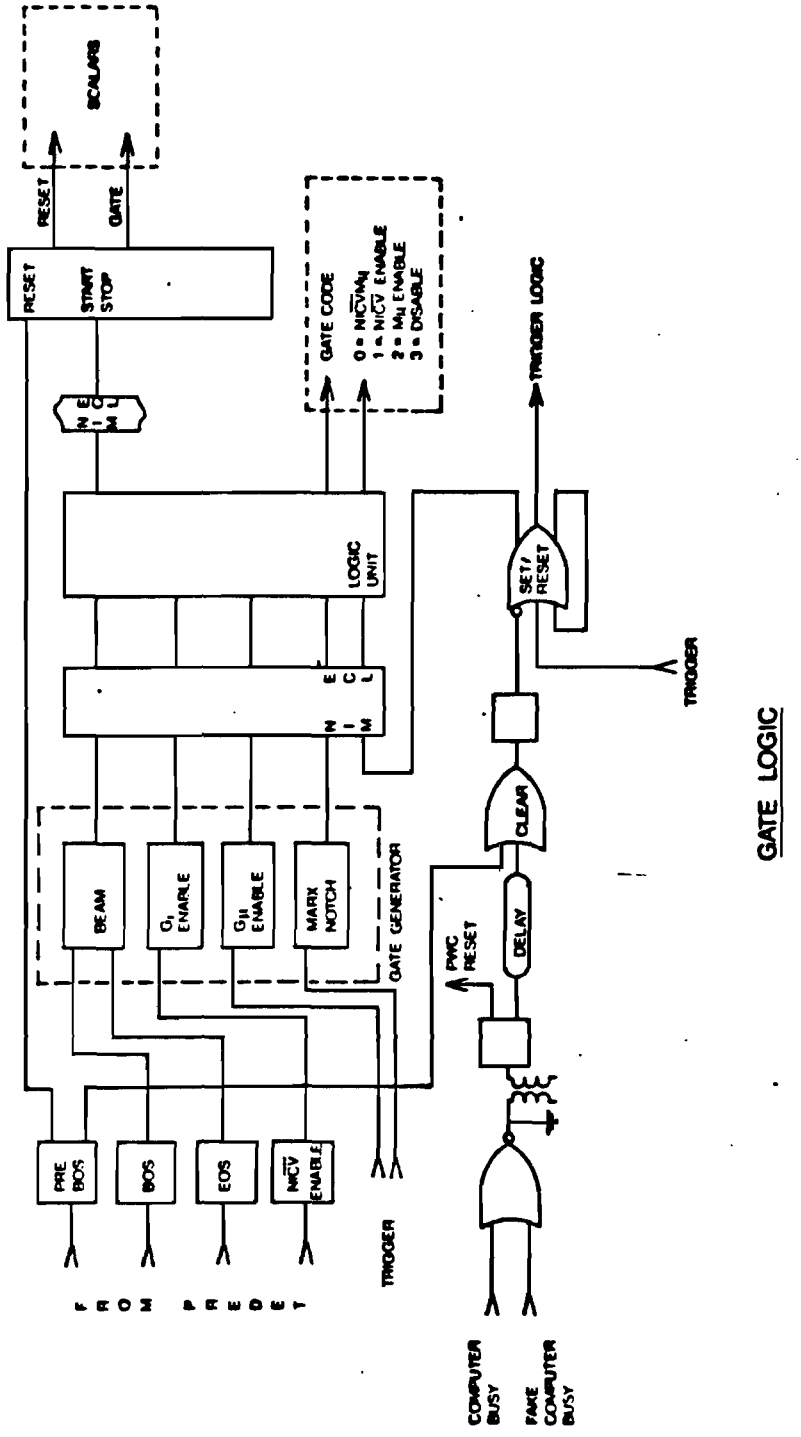

Figure 4-3: The Trigger Logic Diagram, Part II: This shows the final trigger selection units and the data acquisition control.

4.1 Gating

In order to maximize efficiency during data acquisition, a trigger gating system was devised. The accelerator delivered beam in one second spills every fifteen seconds. With 4.0×10^{11} protons during each spill, or in other words with 2.3×10^{6} neutrons incident on the streamer chamber, an average of three NI$\bar{C}\bar{V}$MU triggers were observed; however, the rate of plain interactions producing NI$\bar{C}\bar{V}$ triggers was 8×10^{3}. The gating system limited the number of background interactions recorded on film. The charging time for the Marx dictated the maximum event rate to be 5 pictures per second. At the end of each spill, during the final 10 msec, a gate was opened to permit the recording of NI$\bar{C}\bar{V}$ triggers. For these pictures the recharging of the Marx was done between spills, and hence did not limit the time available for recording NI$\bar{C}\bar{V}$MU events. After each picture, during the time when the Marx recharged, a gate opened to permit the recording of the background MU triggers. Figure 4-4 shows the gating system.

For NI$\bar{C}\bar{V}$MU events and NI$\bar{C}\bar{V}$ events a picture was recorded on film while records of the scintillator hits and the PWC hits were recorded on tape. For MU events only the counter and chamber information was recorded.

4.2 Monitoring the Experiment

At the end of each spill, information from the scalars monitoring the trigger counters and the beam was recorded. In addition to this, the magnet settings and the coded trigger logic for each programmable logic unit was written onto the tape. The on-line software, MULTI, operating under RT-11 [84] on a PDP11/34, handled all the data acquisition and allowed us to monitor the performance of the experiment. The standard MULTI program was appended to include the CAMAC Diagnostic Language commands needed to operate the programmable logic units and high voltage supplies.

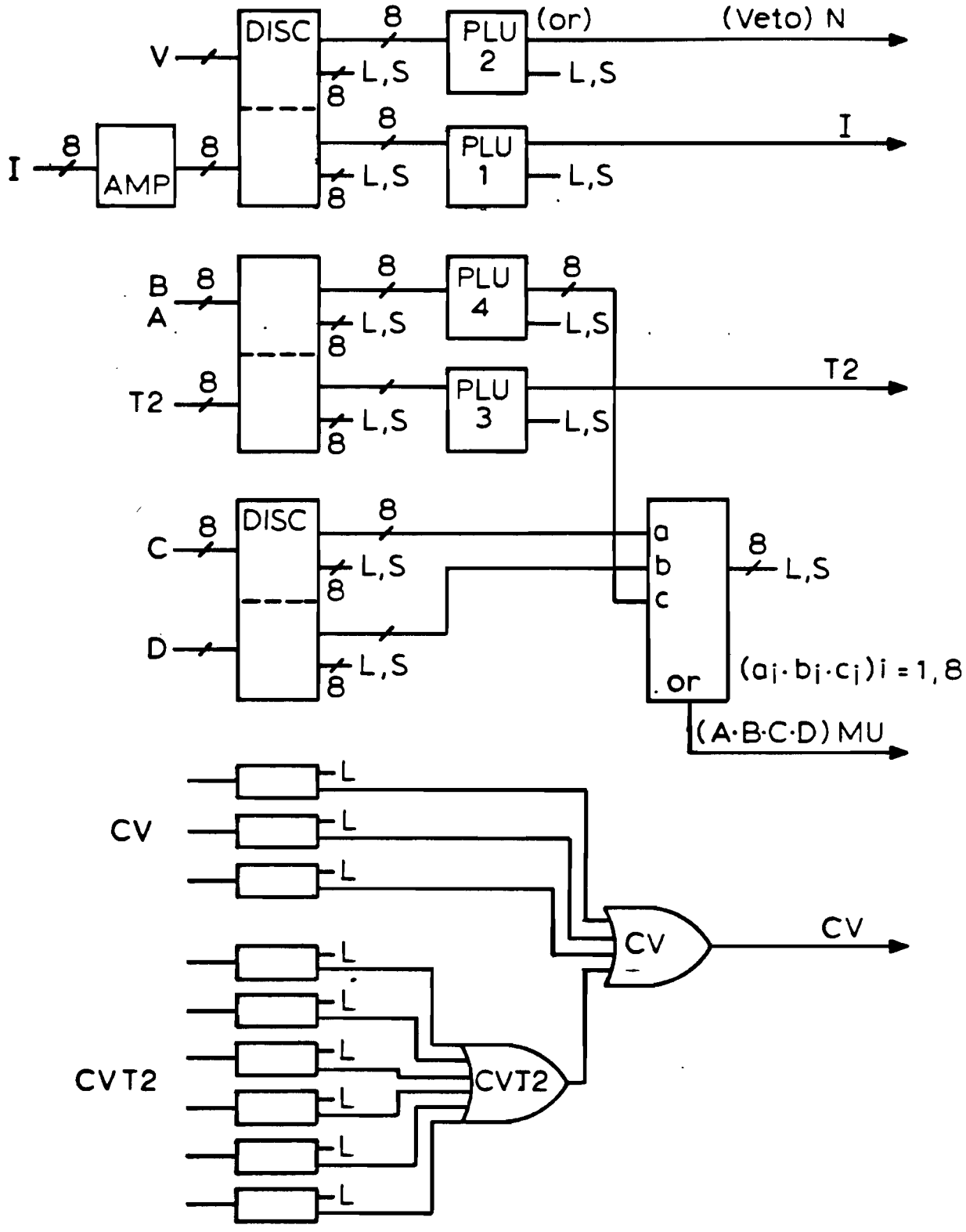

Figure 4-4: The electronics for the trigger gating system

4.2.1 Monitoring the Streamer Chamber

We ended each run after 2500 pictures to take test strips and reload the cameras. Evaluations of the test strips were crucial for setting the best operating voltage for the streamer chamber. Furthermore, we used the test pictures to study and monitor the fraction of pictures containing visible interactions. This fraction, the fiducial fraction, remained steady at 9% throughout the experiment. The interaction trigger selected events that occurred in the region of the chamber, but it was not completely selective.

Small LED dots formed the frame numbers for the pictures. Twelve fiducial marks were exposed onto the edge of every frame along with the run and frame number. The fiducials were the blunt ends of small (100μm) light fibers illuminated by LEDs. On the developed film, the fiducial marks appeared as twelve dark dots. The fiducial marks could be measured to an accuracy of 10μm to provide accurate alignment of each picture. Before the data acquisition began, a three-dimensional grid was photographed inside the fiducial region of the chamber. With these pictures, we were able to obtain the optical constants of the streamer chamber system [112].

4.2.2 The Wire Chambers

We were able to monitor the current through the chambers and we attached an alarm to the power supply to alert us to a sudden increase. A television camera permitted us to monitor the gas flow through the chambers at all times. On-line monitoring of the chambers' performance was achieved through the data acquisition program MULTI.

The chambers operated in a mode where the average anode hit was 1 strip wide, and the average cathode hit was more than 2 (4cm) strips wide. Tests on a small prototype chamber indicated that this was an appropriate operating condition. However, studies of the clusters completed in the off-line analysis indicated that the operating voltages were slightly too high, and the cathode hits were too wide. Note that the the FWHM of a cathode pulse in a chamber with an anode-to-cathode gap of 6 mm has been reported to be 1.2 cm [46]. The resolution was not greatly affected since the charge is distributed symmetrically; however, the wide cathode hits increased the confusion in multi-hit events.

The readout system for the PWC's, being a simple amplifier and threshold discriminator system, was not designed to enhance the chamber resolution since it did not use the pulse height information. The pulses from the chamber were amplified and discriminated and a 60 nsec differential pulse was sent to the latch system over flat multiconductor ribbon cable. The delays in the ribbon cables were carefully selected and adjusted so that the 100 nsec gate initiated by a trigger would arrive at the latch controller at the correct time. Timing studies assured us that the gate timing optimized the chamber efficiency.

4.3 Muon Studies

The initial three weeks of the experiment were spent studying the neutron beam and aligning the collimators. The earlier engineering test in the spring of 1981 had been spent studying the beam and the muon rates in the experimental hall. We added 100 tons of steel and concrete shielding to the front end of the experimental hall as a result of the spring (1981) studies. The flux of charged particles outside the beam originating upstream of our target could reach 2.5 Mhz in the veto wall with proton intensities of 4.0×10^{11} even after the shielding was added.

We wanted to be able to run at high beam intensities without overwhelming the trigger with accidental muons. Studies showed that less than 5% of the background MU triggers occurred without firing a veto counter. We counted an average of 1.7×10^4 MU triggers per spill and 8.0×10^3 NI$\bar{C}\bar{V}$ triggers per spill at 4×10^{11} protons per pulse. After discarding MU triggers occurring in coincidence with veto counters, the accidental NI$\bar{C}\bar{V}$MU trigger rate was estimated to be 0.1 triggers per spill. In the off-line analysis we were able to decrease this number by another factor of 6 by insisting that each muon track point to the streamer chamber.

The polarity of the toroid was alternated after approximately every five runs. Acceptance studies using a Monte Carlo simulation of hadronically produced D - $\bar{D}$ pairs indicated that the trigger acceptance for defocusing charm-like muons was enhanced by a

factor of 2 over the acceptance for focusing muons. Though this ratio varied slightly with production models, the trend was apparent in all models, since the muons were produced at small laboratory angles [112]. By running an equal time in both modes, we hoped to be equally sensitive to positive and negative muons.

4.4 Alignments

Several alignment runs were recorded with the toroid field set to zero. The magnets were carefully degaussed for each alignment run. Calibrated Hall probes, which were attached to the printed circuit boards inside the toroid and monitored through the Fermilab beam line control system, provided on-line measurements of the toroid field. The alignment runs were used to establish the relative alignment of the PWC's and the trigger counters. The chamber and counter efficiencies were also determined from off-line analysis of these runs. A special alignment run at low beam intensity was made with the three PWC's pushed west by 15 inches putting active regions of each chamber into the hole in the hadron shield. With this data, we were able to align the streamer chamber with the PWC's by matching tracks in the streamer chamber to tracks in the PWC's without multiple scattering.

Chapter 5

FILM ANALYSIS

The analysis of the data was split into two parts. The initial event selection was performed by selecting events with good muon tracks in the PWC's. After this initial selection, the analysis of the film and the analysis of the PWC data continued independently. The muon analysis, including the description of the initial muon event selection, will be discussed in Chapter Six. In this chapter, there will be a brief discussion of the film analysis. For further details of this analysis, see Reference [112].

The track width (120 μm) was too wide for us to see the secondary charm decay vertices with much efficiency. However, we found that we could measure single isolated tracks quite well (σ=14-22μm). The strategy of the film analysis program was to measure every clear track in each event that satisfied the off-line muon criteria. and select events in which the combination of measured tracks was inconsistent with one vertex. By simultaneously studying the vertex fits in pictures taken without the charm-enhancing trigger, we could make a comparison between a sample of normal hadronic interactions and a sample of interactions enriched in charm. Frames in both samples had visible secondary vertices, but these were at wide angles and long decay lengths indicative of slow strange particles.

The 116,073 NI$\bar{C}\bar{V}$MU trigger pictures collected were reduced to a sample of 20,138

pictures by an initial off-line muon selection. In addition to this, we included in the sample a second set of NIC̄V̄MU events which did not satisfy the initial off-line muon cuts and NIC̄V̄ events chosen at random. These 48 x 10^3 events were scanned at the Fermilab Film Analysis Facility. The scanners recorded the frame numbers of the pictures containing visible interactions. Interactions occurring within 2 cm upstream of the center of the chamber were included even if their vertices were not visible. Interactions occurring further than 12 mm downstream of the center were too close to the downstream edge of the chamber, so they were ignored. The fraction of pictures with visible interactions was 9%, therefore the scanning process reduced the sample size to 1807 NIC̄V̄MU with good muons, 1115 NIC̄V̄MU events with no muon and 1612 NIC̄V̄ events. In total, the data came from 75 separate rolls of good streamer chamber film with mixed triggers.

All events in the sample with fiducial interactions were measured at Fermilab on MOMM's (Manually Operated Measuring Machines), or at Yale on a Vanguard measuring machine. The point setting error for our streamer chamber film on the MOMM's was 22.0 μm. The film measuring facility was initiated at Yale to aid in the analysis program and increase the physicist's supervision. The Vanguard measuring machine at Yale had a point setting error of 14.0 μm for our streamer chamber tracks [112].

5.1 Event Measurement

Before each frame was measured, the twelve fiducial marks surrounding each picture were measured. The distances between pairs of fiducial points were checked on-line and off-line. Events with bad fiducial mark positions were remeasured.

Each event had two stereo film views, offset by 7°. All tracks were measured that were clear in both views. Tracks that were clear in one view only were measured in that view, but were recorded as overlapping in the other view. Overlapping tracks were measured as obscured regions on the film. Seven or eight points were measured for each track on average. Three was the minimum number allowed and fifteen the maximum. The minimum distance between measurement points was 400 μm (on the film).

For each event, the measurer recorded the number of measurable tracks, the number of interesting tracks such as decay tracks, the number of nuclear fragments, and the number of stray tracks crossing the chamber. Comments on the event or the picture quality could also be recorded. If a frame contained two independent interactions, they were measured as two separate events. Any secondary interaction was measured as part of the associated primary interaction. All clear tracks from the primary vertex and secondary vertices were measured. Events that were too faint or too dark to be accuarately measured were skipped.

Before measuring each track, the measurer recorded the track type and the track quality. The track type flagged tracks from secondary vertices or tracks with heavy ionization. The heavily ionizing tracks were left by fragments of the neon nucleus. We measured these tracks if they were clear and straight. Tracks from secondary vertices were labeled to separate secondary hadronic interactions from neutral or charged decays. A secondary interaction was distinguished from decay by its nuclear fragments. A secondary interaction without visible nuclear fragments was treated as a decay. Minimum ionizing tracks which clearly did not originate from the primary vertex and could not be associated with a visible secondary vertex were labeled as short decays. The track quality label gave an indication of the streamer density and streamer brightness.

The topology of interactions at these high energies was such that most of the particles travelled forward in a jet-like fashion. Since the average charged particle multiplicity is about 8 at these energies, much of the forward region was obscured by overlapping tracks. Furthermore, the region near the primary vertex could become so dense with streamers that an obscuring flare would be formed. These problems were worsened by reflections of the flares from the wire electrodes. In order to record all the information possible for each picture, the measurers recorded the boundary of each obscured region. They classified regions of overlapping tracks and regions obscured by flares separately.

5.1.1 Data Handling

At Yale, the output of the Vanguard machine was read through the program MSCAN [108] into a LSI-11 computer.[2] The coordinates of each measured point were written onto a file stored on a floppy disk. These data files were later transferred to the PDP10 computer for analysis.[3] Once on the PDP10, the measurement data were converted into the standard analysis format.

At Fermilab, the measurement data were read into a PDP15.[4] At the end of each event, the data were transferred to the Fermilab CYBER.[5] The data from each roll were written onto a tape in ASCII format and shipped to Yale. When the tape arrived, the files were read into the PDP10, and converted to the standard analysis format.

Once the measurement data files were converted into the standard format, the files were merged with files containing the PWC and counter information. The merged files were written in a format compatible with the main off-line analysis program.

5.2 The Picture Analysis

The event reconstruction was performed with the aid of the PDP10. Each measured view was analyzed independently. Efforts aimed at taking advantage of the 7° camera stereo angle between the two views did not yield satisfactory results. The stereo angle was too small and the track width too large to do the reconstruction with the accuracy necessary to detect short decay distances in three dimensions. Therefore, we studied each chamber interaction as two independent projections onto the x-y plane.

The main off-line analysis program MAPP was structured so that the user would have interactive access to the data files containing the measurement and PWC data. Our

---

[2]LSI-11: Digital Equipment Corporation

[3]PDP10: Digital Equipment Corporation

[4]PDP15: Digital Equipment Corporation

[5]Cyber 175: Control Data Corporation

track and vertex fitting routines and intermediate muon analysis programs were contained inside the MAPP library. The program gave us the capability of examining each measurement point and each fitted track in a graphic mode or in tabular form. See figure 5-1.

The measurement procedure was calibrated by measuring NIC̄V̄ events both at Fermilab and at Yale. The point setting errors were assigned by fitting vertices to the single vertex events and adjusting the errors so that the X^2 per degree of freedom for the vertex fits was equal to one. Separate point setting errors were assigned to minimum ionizing tracks and to nuclear fragments.[6] We studied the performance of the machines for measuring a well-calibrated grid. The accuracy of both machines is better than 10 microns. Both machines are film plane digitizers and have precision stages for moving the film.

5.2.1 Track and Vertex Fitting

The track fitting algorithm was a least-squares fit to the measured points. The fitting could be done in two or three dimensions. We used two-dimensional fits for the analysis of this experiment. Each track was labeled so as to indicate the vertex from which it originated. If a secondary vertex was not visible, but the track missed the primary vertex, it was labeled as a short decay. A vertex position was calculated by making a least-squares fits to the fitted tracks labeled as associated with that vertex. The original labels were those assigned by the measurers. By labeling measurement points or tracks with a zero in the analysis, they were temporarily removed from the fits.

The information available for each track included the X^2 of the track fit, the contribution of each point to the track X^2, the distance of closest approach to each vertex (the miss distance), and the error on this miss distance. In addition, of course, there was the information on the slopes, intercepts and errors associated with the fitted tracks. The vertex information included each vertex position and accompanying error and the X^2 for each vertex.

---

[6]For a complete discussion of the errors, see Reference [112]

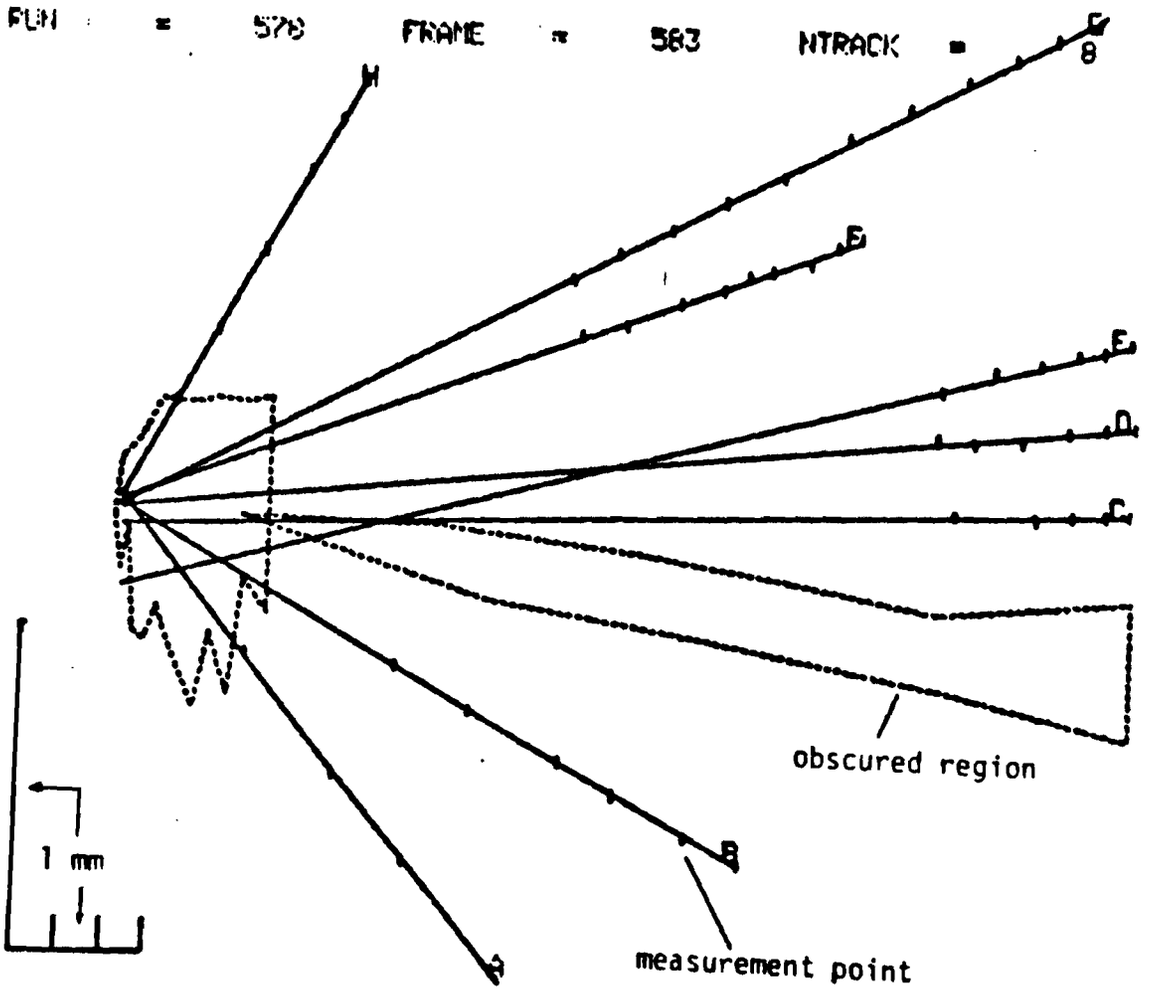

Figure 5-1: An example of a reconstructed event showing the measured points, the fitted tracks and the boundaries of the obscured region

5.3 Candidate Selection

Since the average energy of the neutron beam was 330 Gev, we expected to see approximately 8 charged tracks in each of the pictures. In addition, the charged multiplicity for each charm decay has been measured to be 2.3 [65]. Therefore, looking at the X^2 of a single vertex seemed to be an appropriate technique to separate charm events from single vertex interactions. However, Monte Carlo studies showed us that we often measured only one charm decay track. The other tracks were obscured and were not measured. The vertex X^2 was not a sensitive enough statistic to provide a separation of charm events from ordinary single vertex events [112].

The analysis was built around the idea of studying the miss distances of single tracks from the primary interaction vertex. The miss distance ($S=\gamma\beta c\tau\sin\theta_{lab}$, where θ_{lab} is measured relative to the beam direction) is almost a Lorentz invariant for daughters produced in the decay of relativistic particles. We devised a method for determining the location of the primary vertex from a class of non-charm tracks and then examined the miss distance of each of the remaining tracks. In this way, we could select candidates with short decays even though the decays were not visible by eye.

The scheme for selecting the charm candidates from the pictures was as follows. We labeled all the measured tracks from the primary vertex and from neutral and charged decays to associate them with a single vertex. We treated each view independently. Furthermore, we checked the topology of each neutral and charged decay flagged by the measurers. If one of the prongs from a decay was greater than 150 mrad with respect to the beam, all the prongs from that decay were fit to a secondary vertex. Slow strange particles decay at these wide angles whereas charm does not. Secondary interactions within the chamber were fit to second vertices. All other tracks were fit to one vertex.

We next made a cut on the topology of the event to select events with an unambiguous primary vertex. We required at least two measured tracks originating at the primary vertex to be at angles greater than 150 mrad, and at least one measured track to be at an angle less than 150 mrad. The wide angle tracks were used to

accurately define the primary vertex position. The effect of this topology cut was to reduce the sample by a factor of 2. See Figure 5-2.

The candidate selection was made by choosing events with at least one track with an angle less than 150 mrad and with a value of the miss distance (miss distance $s=$ the distance from a track to the primary vertex) divided by the error in the miss distance ($S/\Delta S$) greater than 3.0. The ratio of charm events to normal interactions should be high in this region. Monte Carlo studies described by L. Tzeng in Reference [112] showed that less than 4% of properly measured single vertex events have a track with $S/\Delta S>3.0$, while 38% of charm evets have at least one such track. The backgrounds come from poorly measured events and strange particles. The same event selection was done for $NI\bar{C}\bar{V}$ events. The $NI\bar{C}\bar{V}$ events provide a model for these backgrounds. See Reference [112] for more details of the miss distance analysis and the associated Monte Carlo studies.

5.4 The final event selection

The final film selection was performed by a physicist scanning all events with $S/\Delta S > 3.0$. Events with obvious mismeasurements were remeasured. Events with mislabeled tracks were fixed. Events that were too faint were discarded. In all, the cleanup reduced the sample by a factor of 3.5. The $NI\bar{C}\bar{V}$ background events were treated identically.

At this point, we combined the information with refined muon track information (see Chapter Six). Of the 1807 $NI\bar{C}\bar{V}MU$ events measured (from the original scan lists), 1492 remained after the Second Pass muon analysis. We checked each event to assure that the measured muon track was consistent with a track from the interaction in the streamer chamber. We also accepted events as being consistent if the muon track matched a measured streamer chamber track of if the muon track projected back to the obscured region where no tracks were measurable. The total number of $NI\bar{C}\bar{V}MU$ events with muon tracks consistent with a track in the chamber was 640. The topology cut reduced this sample to 362.

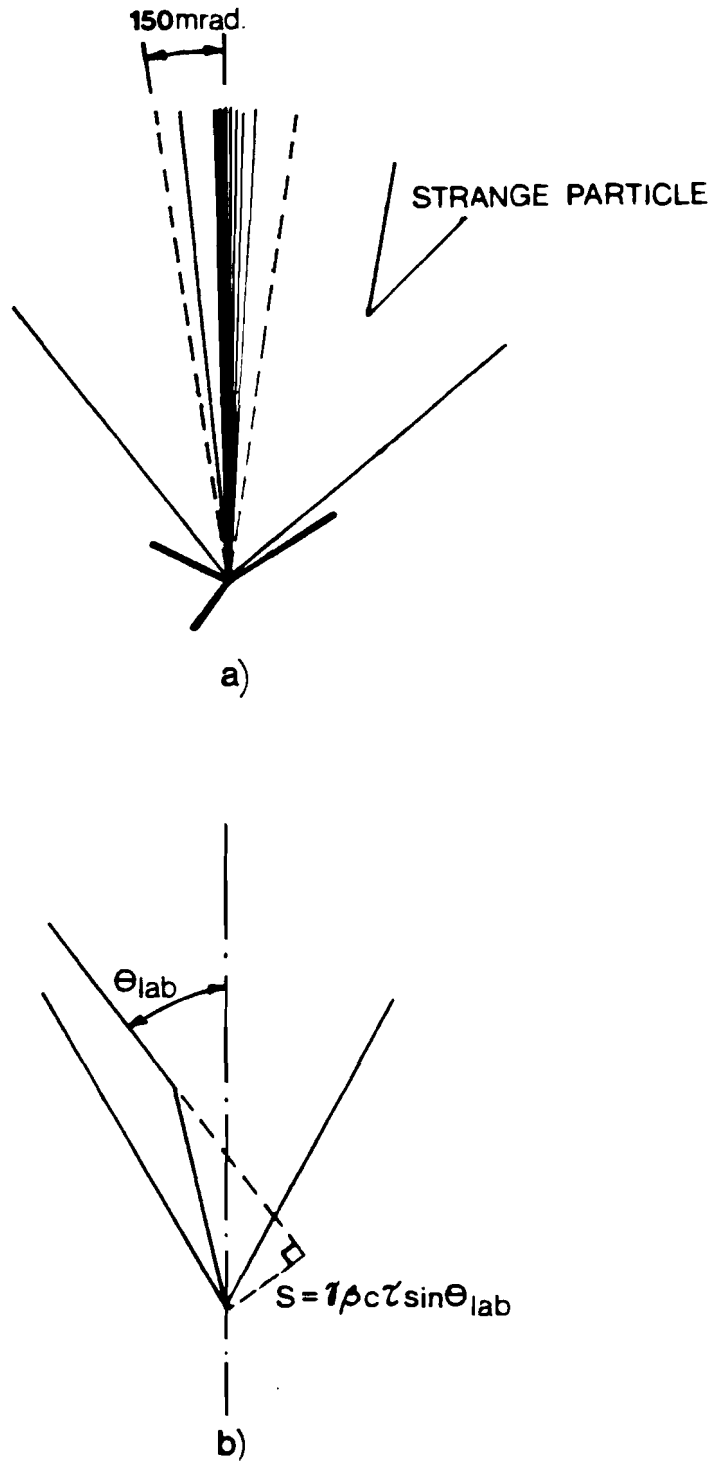

Figure 5-2: a) Schematic drawing showing the topology cuts; b)Schematic drawing showing the miss distance

The total number of NIC̄V̄MU events with $S/\Delta S > 3.0$ and a muon track candidate was 120. After scanning each picture carefully, we reduced the sample to 34. By including the final muon selection criteria, the charm candidate sample was reduced to 24. Of these events there was only one event in which the muon was inconsistent with the picture.

The total number of measured NIC̄V̄ events before the topology cut was 1612. After the topology cut, 892 events remained. Of these, only 88 events had $S/\Delta S > 3.0$. We attributed 64 events to poor event quality and obvious mismeasurement. The remaining 14 events became our estimate of the background due to measurement error and strange particle decays. The muon trigger enhances the number of strange particle events in our final sample; however, we expect this enhancement to be quite small. A Monte Carlo simulation [112] was performed using measured strange particle cross sections to predict the number of strange particles that might contaminate the final sample. In the Monte Carlo, the kinematic cuts (the topology cuts) were able to reject most of the strange particles that decayed within the chamber from the $S/\Delta S$ analysis. Figure S/DS shows the $S/\Delta S$ distributions for the candidate events and the scaled background NIC̄V̄ events.

We took a sample of NIC̄V̄MU events with $1.0 < S/\Delta S < 2.0$ to represent events with background muons. This sample of events was used to estimate the backgrounds to the measured charm-muon distributions. Monte Carlo studies of the $S/\Delta S$ distribution for events with or without charm indicated that the ratio of background to real charm was high in this region, therefore the sample will show little charm contamination. See Figure 5-4.

Summarizing the results of the film analysis, we selected a sample of 23 events with a downstream muon track and at least one measured streamer chamber track with $S/\Delta S > 3.0$. We conclude that these events were rich in charm production. The 23 evets yield 17.32 short-lived "charm" events and only 5.68 background events. The number of background events was determined from the number of ordinary hadronic interactions having a measured $S/\Delta S$ greater than 3.0 in a total sample of 362 NIC̄V̄ events. Table 5-1 gives a summary of the results.

$NI\bar{C}\bar{V}MU$ Measured	Muon Candidates	1807
$NI\bar{C}\bar{V}MU$ Measured	Refined Muon Candidates	1492
$NI\bar{C}\bar{V}MU$ Measured	'Matched' Muon Candidates	640
$NI\bar{C}\bar{V}$ Measured	All Events	1612
$NI\bar{C}\bar{V}MU$ Measured	Correct Topology	362
$NI\bar{C}\bar{V}$ Measured	Correct Topology	892
Charm Candidates	$S/\Delta S > 3.0$	23
$NI\bar{C}\bar{V}$	$S/\Delta S > 3.0$	14
$NI\bar{C}\bar{V}$	Scaled	5.68

Table 5-1: Final results of the $S/\Delta S$ analysis

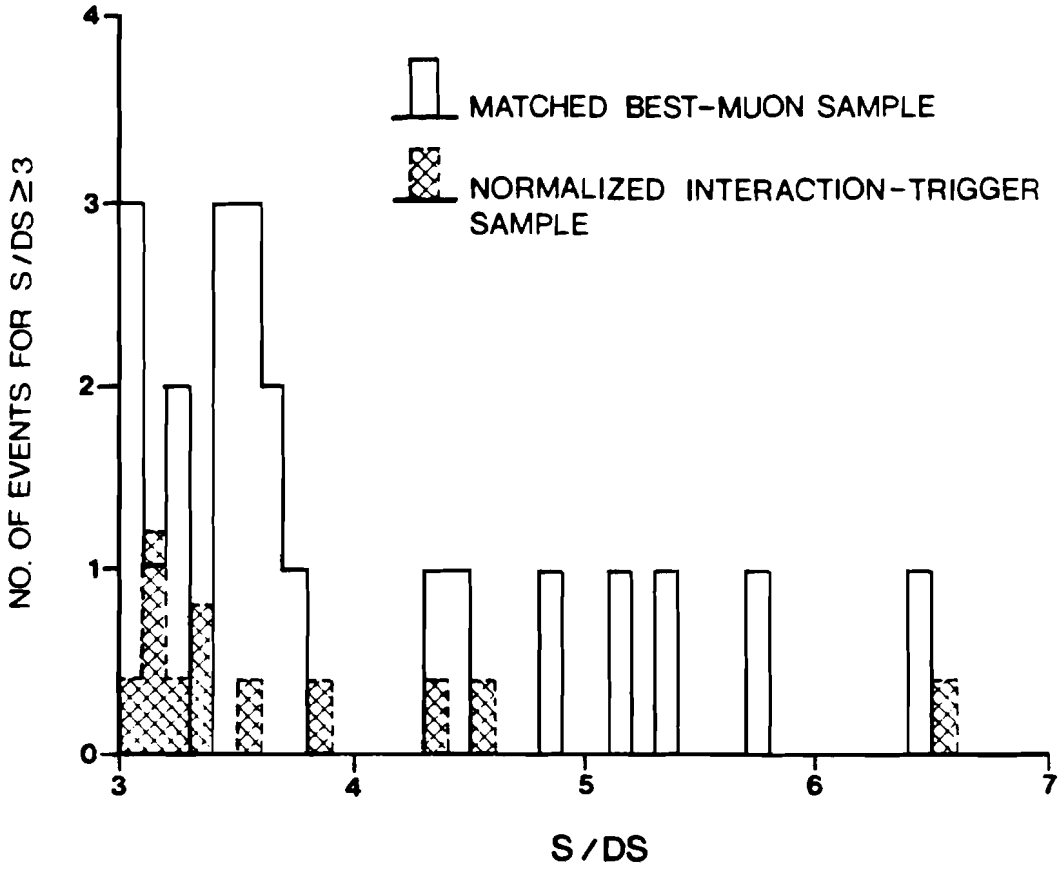

Figure 5-3: The Candidate events with $S/\Delta S > 3.0$

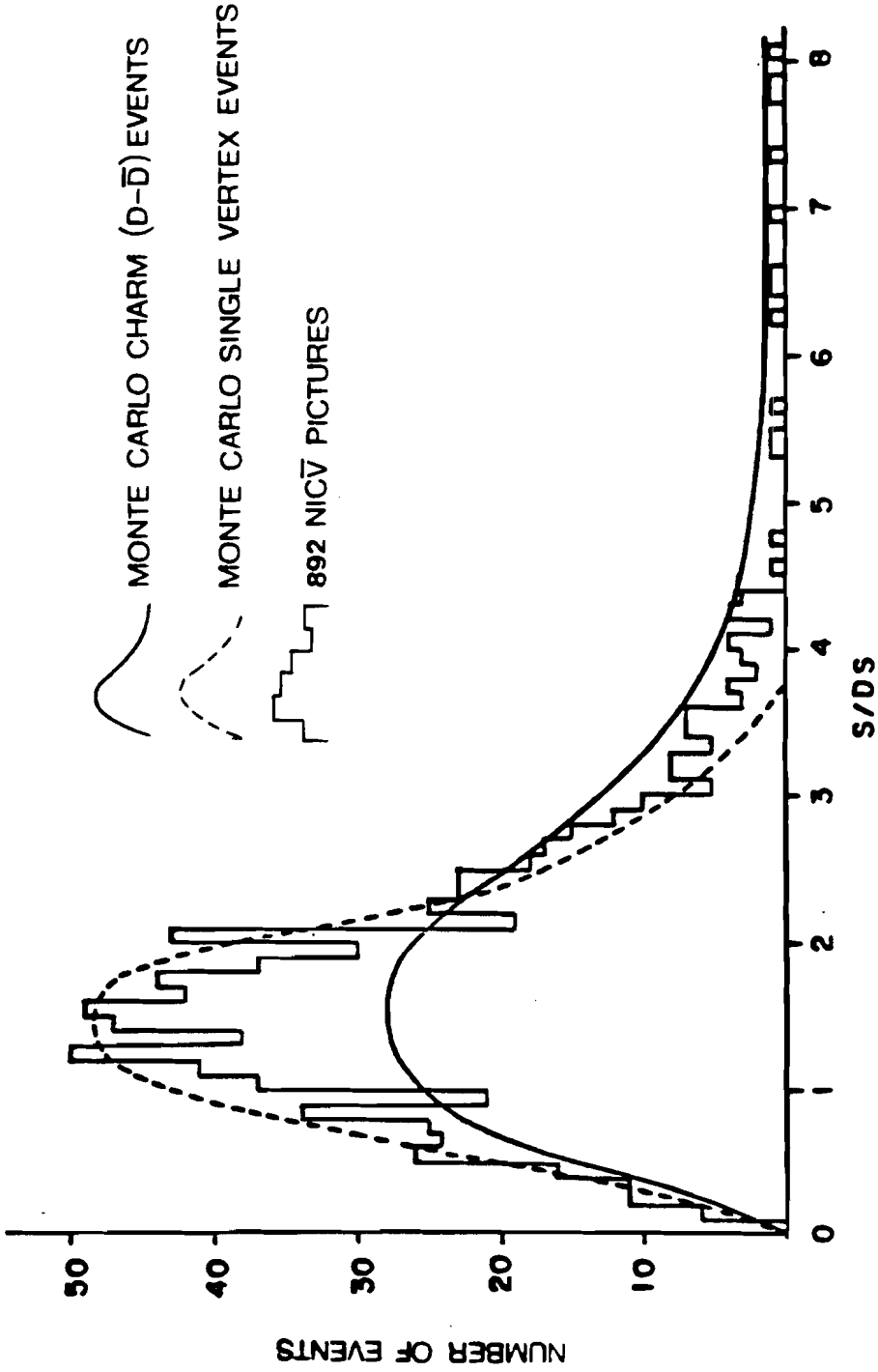

Figure 5-4: The S/ΔS distributions for Monte Carlo events with and without charm; the NIC̄V̄ distribution was plotted before rescanning for mismeasurements

Chapter 6

MOMENTUM ANALYSIS

The muons from interactions inside the streamer chamber were studied carefully in an analysis which not only selected good muon candidates from the large sample of accidental triggers and punch-through pions, but also determined the momentum and angles of the selected muons. The first pass at selecting muon events was done by the on-line trigger. As mentioned previously, the trigger required that hits were recorded in each of the front four banks of scintillation counters, that these hits formed a straight muon road, and that there was at least one hit in the counter bank behind the toroid. The segmentation of the banks of counters was very large, so further selection performed off-line was necessary to refine the data sample. The film from each event tagged off-line as an interesting muon candidate was scanned for fiducial interactions.

The muon track selection was done in three phases. Section 6.1 describes the first pass in which muon candidate events were selected from the raw data tapes. Refinements to this selection are describes in Section 6.3. All pictures from NIC̄V̄MU events with good muon tracks after the first pass analysis were scanned for fiducial interactions and then measured. Section 6.5 describes the second phase of the analysis. All the measured NIC̄V̄MU events were analyzed in this pass. The analysis of the PWC hits was more sophisticated in this second pass. Estimates of the initial muon angles and momentum were derived from this analysis. In the third phase, a muon's angles and momentum were

calculated in a global fit of a muon trajectory to the measured hit's in the PWC's. This analysis is described in Section 6.6 and Appendix 1.

6.1 Event Selection—The First Pass

On the first pass, the object was to retain as many candidate events as possible while eliminating the obviously bad events. The definition of a muon track was generous for this round. More careful study of the muons allowed further refinements, but only after the picture measuring process was completed.

The first requirement for a muon candidate was that each of the three wire chambers recorded a cluster in at least two of its three planes. A cluster in a plane was defined as a strip or consecutive group of strips registering a signal above threshold. In the case where all three planes fired, the strip combinations were checked to see if a region could be found where the three planes' clusters overlapped. If so, a so-called triplet was formed centered on the geometric center of the overlap region. The error assigned to the triplet center reflected a model of cluster formation in which the cluster center could lie anywhere across the width of the hit. The error assigned was thus equal to the cluster width divided by the square root of twelve as would be appropriate for such a flat distribution. For events with hits in only two planes, the third plane was considered inefficient and ignored. Once again the center of the overlap of the clusters defined the triplet center and the errors were evaluated as before. With this method of triplet analysis the error was grossly overestimated for the cathode strips. The error for wide cathode hits is actually much smaller. A charge near the anode wire induces a charge symmetrically on the cathode planes, so the particle has usually passed near the center of a cluster. Triplets with cathode cluster widths greater than one strip would thus have errors comparable in magnitude to the errors of clusters with width one.

After the triplet formation, fiducial cuts were applied to the triplet centers. These cuts discarded triplets that reconstructed inside the deadened central region of the chambers or outside the hadron filter steel. Events with good triplets in each of the three wire chambers were analyzed further.

In the next step, tracks were formed using three points measured upstream of the toroid: the interaction vertex and sets of triplets from the first two chambers. Using the method of least squares, a straight line was fitted to these three points. For the first pass, the vertex was taken to be at the center of the streamer chamber. The errors assigned to the vertex were 0.1 mm in y and 1.0 mm in z. In the coordinate system of this analysis, x lies along the beam direction and z points upwards. The calculated uncertainties associated with the triplets combined the error due to the finite resolution of the chambers with an estimate of the uncertainty due to multiple Coulomb scattering.

The errors associated with multiple scattering are difficult to calculate because of correlations between the measurement points. For the first pass estimate, we ignored these correlations and calculated the uncertainties for B and D separately. An analytical expression was derived that gave the root mean squared deviation in a plane of a muon with momentum P passing through the amount of steel (steel and concrete) lying between the streamer chamber and the PWC B (or D). The expression was calculated including the large energy loss in the steel. The polar angle, the angle between the line drawn from the streamer chamber to the triplet in B (or D) and the beam line, was used to estimate the muon's momentum. Production models for charm predict a strong correlation between the muon momentum and the muon angle. The results of a Monte Carlo simulation were fit to a polynomial to give an expression for this correlation. The multiple scattering error was thus calculated independently for each chamber. By ignoring the correlations between the measurement points, we overestimated the error associated with multiple scattering.

A cut was made on the X^2 derived from the least squares fit to a straight line through the vertex point inside the streamer chamber and the triplets in PWC B and PWC D. Tracks with a X^2/degree of freedom greater than 2.0 were rejected (the number of degrees of freedom is two). We studied events with one and only one good triplet combination in each chamber and found this to be a generous cut.

Triplets in the D chamber associated with acceptable upstream tracks were paired

with triplets in the T2 chamber. For the next test, the B chamber hit was ignored completely. The azimuthal angle (ϕ) of the two points were compared under the assumption that the points were part of a particle trajectory originating at the center of the streamer chamber. By comparing the two values of phi, obvious accidental events were discarded, since the angle phi should remain unchanged as a muon traverses the toroidal field except for the effects of multiple scattering. A $\Delta\phi$ cut was applied to all the combinations. Combinations with $\Delta\phi > 40^\circ$ were rejected. Figure 6-1 shows a plot of the change in ϕ between D and T2 for events with one and only one triplet in all three chambers.

Summarizing, the first round of muon analysis selected events with at least one good triplet in each of the three PWC's, forming at least one good track defined according to the criteria that $X^2 < 4$ and $\Delta\phi < 40^\circ$. Events which satisfied these cuts were called Muon Candidates and were scanned for fiducial interactions which were then measured.

6.2 Muon Studies and Alignments

As mentioned in Chapter Four, we set the toroid field to zero for several runs and collected a sample of straight muon tracks. We used this sample to determine counter and chamber efficiencies and chamber alignments. The alignment of a counter relative to the PWC's was obtained by mapping the position of the triplet in the nearest chamber for events in which the counter's latch was set.

The alignment between the planes of the PWC's was determined from events with one and only one cluster in each one of the three planes of the chamber of interest. By determining the average of the quantity $\Delta U = \sqrt{\frac{1}{2}}(Y+Z) - U$ for each of the chambers, the alignment parameters were determined and the appropriate corrections made. The corrected ΔU distributions for each chamber is given in Figure 6-2.

The alignment between the three PWC's was determined from straight-through MU triggers with one and only one hit in each of the nine planes. The average residuals between the line formed by the Y, Z or U hits in two of the chambers and the Y,Z or U hits in the third chamber provided the value of the relative alignment parameters.

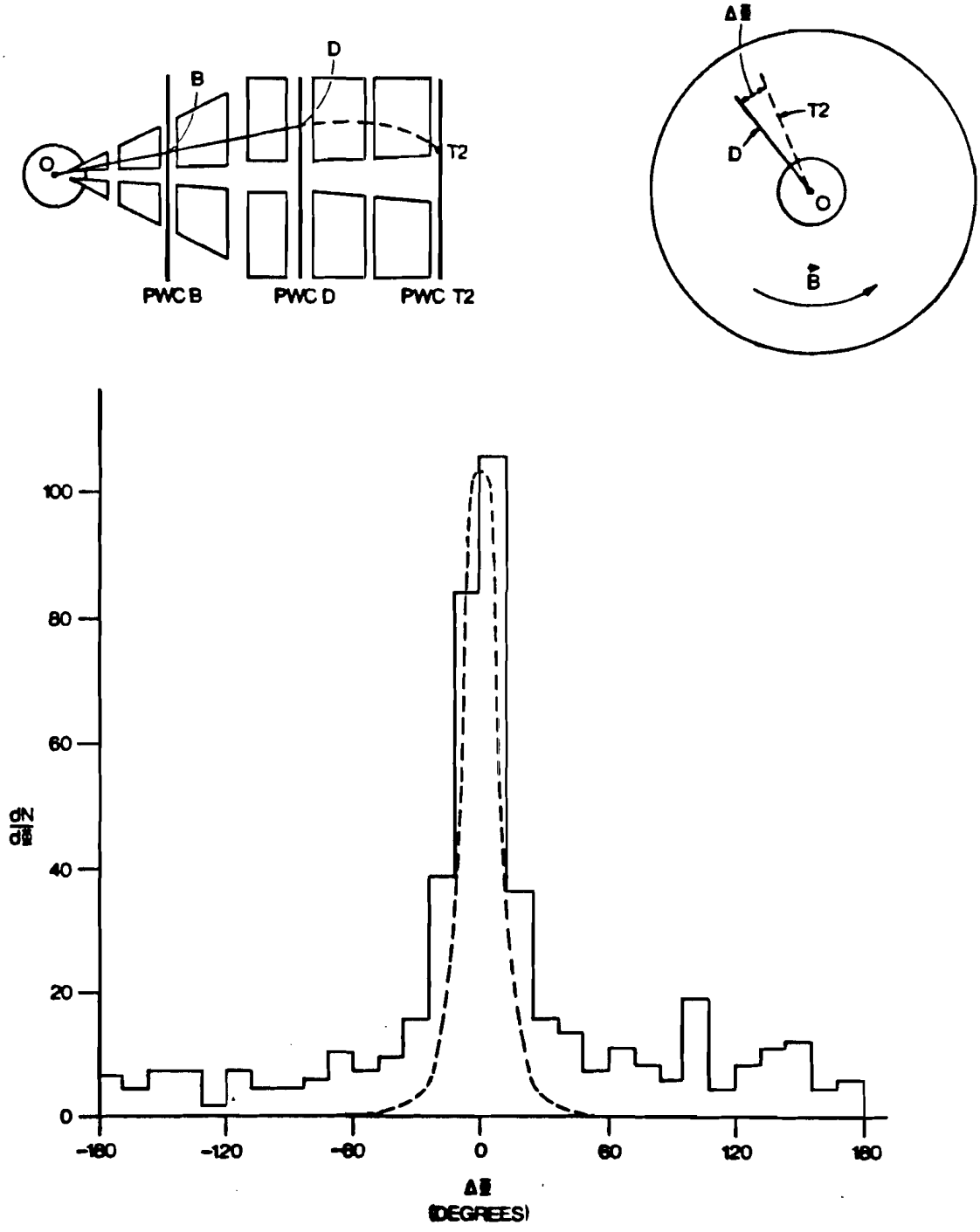

Figure 6-1: Change in ϕ from chamber D to chamber T2. The solid curve the same distribution in a Monte Carlo simulation

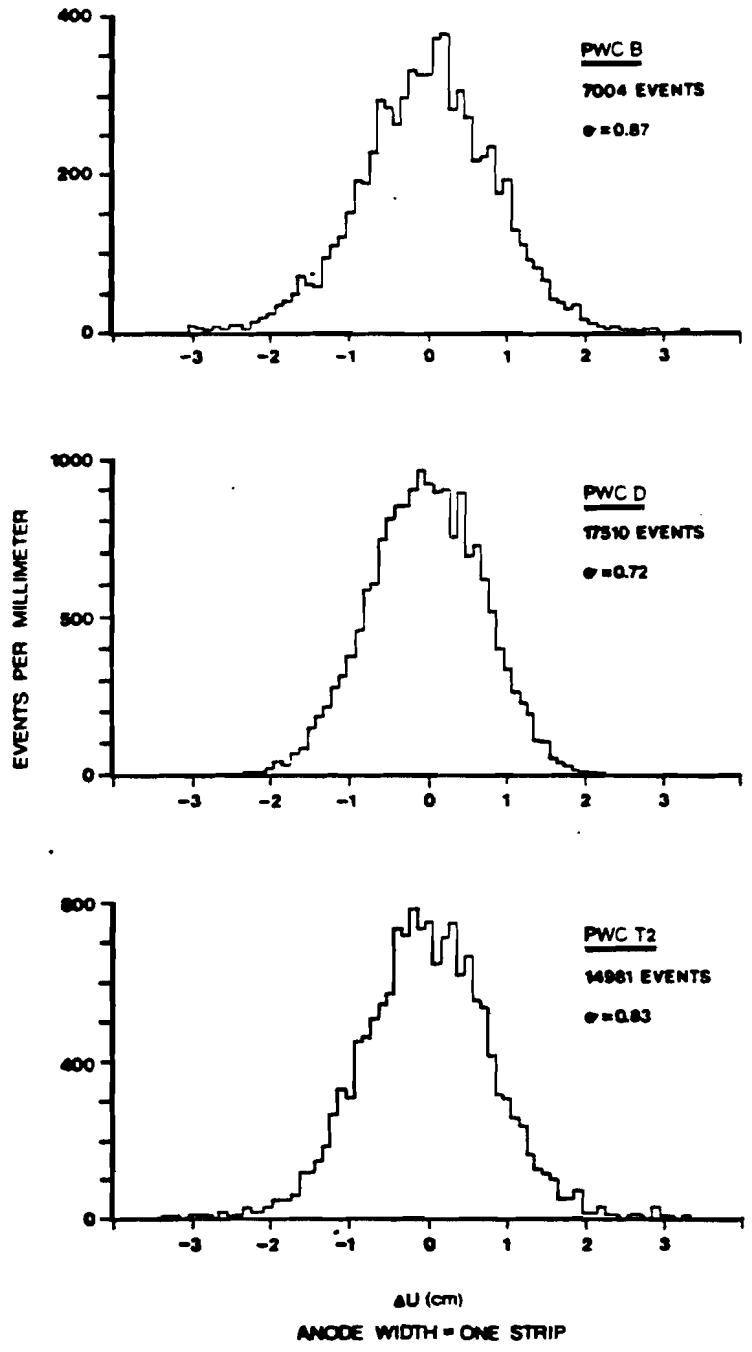

Figure 6-2: The ΔU distributions for triplets with one and only one cluster in each of the PWCs' three planes

The relative alignment of the streamer chamber and the chambers was done using the last data run in which the chambers were pushed 15.0 inches to the west so that the active region of each chamber covered the hole in the center of the hadron shield. We scanned the NIĈV̄ pictures from these events for measurable tracks inside the 30 mrad forward cone. These tracks were measured and matched to the PWC tracks downstream. We made the alignments using the three-dimensional reconstruction technique described in Reference [112].

The chamber alignment parameters were checked by examining a set of events containing one and only one good muon. In addition, the downstream track, when fit to the measured vertex, must have been clear of the obscured region in the chamber. From this sample of clear, clean muon events, we saw an enhancement in the number of events with a track of a projected angle in the XY plane identical to the projected angle of the muon track. No enhancement was seen if we matched the muons from one event to the measured tracks in another event.

The chamber efficiencies were also determined by using MU triggers taken with the toroid field set to zero. To determine the efficiency of each chamber, we required that there was one and only one hit in each of the other six PWC planes. We also required hits in all of the counters in line with the two PWC triplets as an added check. Assuming that a signal in all the PWC planes and counters in a straight line through the apparatus would mean that a charged particle passed through the apparatus, we assumed that the third chamber should record the particle as well. We searched for a good triplet inside the third chamber. PWC B and PWC D were ~95% efficient while PWC T2 was 91% efficient.

6.3 Refinements in the Analysis

The first step in the refinement of the muon analysis was the addition of fiducial volume cuts on the triplets. The first fiducial cut, which was also included in the first pass, was that the triplet in B lay inside the boundary of the steel. The second set of cuts added later, required that the triplets in D lay within the outer radius of the toroid and that the T2 triplets lay outside the toroid hole. The new cut on the D triplets was of little consequence, since there were few hits at such large radii. However, the hits inside the T2 hole were a problem. The T2 chamber had a hole that was 10.6 cm in radius, while the toroid's hole was 22.0 cm in radius. Many extra hits were created by the particles inside the forward 30 mrad cone. The active regions in the other two chambers were completely covered by the steel shielding. By rejecting T2 triplets inside a radius of 22.7 cm, we were able to remove events from the $NI\bar{C}\bar{V}MU$ sample and reduce the number of reconstructed tracks in each event.

In the refined muon analysis, we also required that for each triplet the corresponding scintillation counter in the neighboring bank of counters fired. This requirement did not reduce the total number of events in the sample by more than a few percent. The effective size of the counters was increased by 2 cm in each dimension to allow for the errors in the triplet reconstruction and the effects of the finite track angle.

6.4 Cluster Studies

The method of triplet fitting described in Section 6.1 was known as the overlap method. A good triplet was formed if the hits in the three planes overlapped at any point. The errors on hits were characterized by the full width of cluster. Therefore, a cluster was formed from four consecutive strips would be 8 cm wide and would often overlap with 2 or 3 clusters in the other planes. By studying the ΔU distributions for cathode clusters with widths between 1 and 4 strips, we found that the geometric center of the cathode cluster accurately recorded the position of the muon. The ΔU distributions studied were taken from MU trigger events and from chambers with one and

only one cluster in each of the three planes. The width of the distributions increased slightly with increasing anode cluster width.

For the final analysis, we devised an algorithm for assigning errors to PWC clusters. We studied the ΔU distributions for MU trigger events from several different runs. From this we made tables of the widths of the ΔU distributions, recording a separate entry for each combination of anode and cathode hit widths (ranging from one to four). We assumed an error of $2\mathrm{cm}/\sqrt{12}$ for all anode hits of width less than 4 strips. We found the appropriate cathode error from the width of the ΔU distribution. For a cluster of width greater than 4 strips, we assigned the error: cluster width/$\sqrt{12}$. A cluster with such a width was presumably composed of two hits or a hit plus a delta ray. Hence, they were not treated as if they were symmetric about their centers.

The triplet centers were found by performing a 1-C fit on the three coordinates Y, Z and U. This fitting method was studied extensively in Monte Carlo simulations of the chamber hits. In the Monte Carlo, the cluster widths were simulated by a Poisson-distributed variable which was centered on the center of the actual hit. This description, while crude, fit the observed distributions very well. The triplet fitting was studied by observing the stretch function of one of the three coordinates. The stretch function is defined for a particular variable as the residual ϵ divided by the error in the residual $\sigma(\epsilon)$ [63]. The residual in this case is the difference between the observed value of Y and the fitted value of Y. The width of the stretch function should be one if the errors are properly represented. After setting the cluster errors to be a function of the cluster width as described above, we found that the errors were properly represented for the Monte Carlo events and the data.

6.5 Muon Selection-The Second Pass

The muon selection was done using a revised version of the track fitting procedure described above. The major changes were the new cluster fitting procedure and a better method for estimating the momentum of the muon before the cut on the track X^2. Once the events were selected, a more extensive analysis of their momenta was performed.

The triplets in the PWC's were found by making a X^2 fit to the hits in the three planes of each chamber. The cuts on the triplet formation were as follows:

- A cut was made on the triplet X^2 at 7.0 for chambers with at least one hit in each of the 3 planes.

  For chambers with hits in only 2 of the 3 planes, 'triplets' were formed from the center of overlap of the 2 hits.
- A triplet was rejected if its center lay outside the fiducial volume of chamber. The fiducial volume of each chamber is given below.
  - B: $Y \leq 47.7$cm $Z \leq 47.7$cm
  - D: $R \leq 91.4$cm
  - T2:$R > 22.7$cm
- If the latch for the counter nearest the triplet did not show a hit, the triplet was rejected. Since all events were NI$\bar{C}\bar{V}$MU triggers, we ignored the apparent latch inefficiencies; so if no latches from the nearest counter wass showed a hit, the triplet was accepted.

The track fitting procedure was similar to the one described in Pass One. The major difference was that the momentum of the track was found by analyzing the chamber hits before and after the toroid. The functional relationship between the momentum and the chamber hits was developed from a simulation program that swam particles through the toroid without multiple scattering. In the simulation, the particles were assumed to have originated at the streamer chamber. By generating tracks passing through radius $R_D=(Y_D^2+Z_D^2)^{1/2}$ with momentum P_D at chamber D, we made a table (matrix) of final R_{T2} values. By inverting the matrix, a function $P_D = f(R_D,R_{T2})$ was formed. The assumption was that the unscattered trajectory on average would be a good representation of the actual trajectory.

The momentum was calculated by extrapolating back to the streamer chamber. The minimum value of momentum required to pass through the toroid steel was 2.4 GeV/c. The momentum at the streamer chamber was calculated from the value of the range of a muon in iron.

$$\text{Range} = a\ P_D^{\,b} + L_D \tag{2}$$

$a = 671.4\ g/cm^2$
$b = .932188$
$L_D = 2299.\ g/cm^2\ (1 + R_D/X_D)^{1/2}$

$P_O = (\text{Range}/a)^{1/b} \equiv$ initial momentum at the streamer chamber

In the muon track selection, we first checked the value of $\Delta\Phi$ through the toroid. Then after determining the momentum and charge of the muon candidate, the upstream tracks were fit to a straight line using the method of least squares. In fitting the tracks, the following cuts and assumptions were made:

- The momenta of tracks with no bending in the toroid were set to 10^{30} at the D chamber.
- If the fit momentum of a track (P_D) was less than 2.4, it was set equal to 2.4.
- Tracks with $X^2 > 6.5$ were discarded.
- The errors due to multiple scattering were estimated from the measured momentum.

The sign of the charge of the muon was determined by the direction of its bending in the toroids. The line between the streamer chamber and the D chamber triple was extended to the T2 chamber. If the radius of the T2 hit was greater than (less than) the radius of the extended line at T2, the particle was said to be defocusing (focusing). The sign of the charge was then determined by the sign of the toroid mode. In mode +1, positive particles were focused; in mode -1 negative particles were focused. In our original data sample, 54% of all the NIC̄V̄ triggers recorded by the scalars occurred with the toroids in the +1 mode. The mode of the toroid was determined by measuring the direction of the current in the coils.

The refinements of the muon definition described above were implemented on the Cyber 175 computer at Fermilab. The total number of events in the NIC̄V̄MU muon candidate sample was reduced to 1492. Monte Carlo studies indicated that more than 98% of the charm muons accepted by the first pass analysis passed the refined and final muon cuts. Events which passed all the above cuts were submitted to the final muon analysis program. A file containing the triplets and their errors, the measured charge, the

fitted momentum and the measured angles was passed along to the final analysis program.

6.6 Momentum Analysis

The final muon analysis was a global fit to all the triplets, in order to better determine the track parameters and their errors. Methods used in determining track parameters in counter experiments have been inspired by methods of treating multiple scattering in bubble chambers [68, 81]. The problem here was somewhat more complicated, because the scattering medium was not homogeneous and the magnetic field was not uniform along the particle path length. In addition, the effects of energy loss could not be neglected. Examining techniques used in other high energy physics counter experiments, we were unable to find one that perfectly fit our needs and constraints. A description of some of the standard track fitting techniques can be found in Reference [58].

We used the method of Maximum Likelihood for measuring the initial track parameters $1/QP_0$, Θ_0 and Φ_0 and their errors $E(1/QP_0)$, $E(g(Q)_0)$ and $E(\Phi_0)$. Here Q is the charge, P_0 the initial momentum, Θ_0 the initial polar angle and Φ_0 the initial azimuthal angle. The probability density function describing the probability of measuring a set of three points (the PWC triplets) along the path of a particle originating at the streamer chamber is described in Appendix I. Given a probability density function $P(x|\bar{\theta})$ the likelihood can be written as

$$L(\bar{x}|\bar{\theta}) = \prod_i P(x_i|\bar{\theta}) \quad [63]$$

where x_i is a data point and $\bar{\theta}$ are the parameters to be fitted.

The likelihood function describes the probability of measuring a set of triplets $\{ T^M \}$ if the reference track (ignoring multiple scattering) predicted a set of triplets $\{ T^t \}$. The errors in the track parameters derived from the likelihood function give the 70% likelihood limits. In other words, a 70% probability that the observed triplets $\{ T^M \}$ were generated by tracks with parameters in the interval

$$\Big(1/PQ\text{-}E(1/PQ) < 1/PQ < 1/PQ\text{+}E(1/PQ), \theta\text{-}E(\theta) < \theta < \theta\text{+}E(\theta),$$
$$\Phi\text{-}E(\Phi) < \Phi < \Phi\text{+}E(\Phi)\Big).$$

In searching for the maximum value of the likelihood function, we varied the initial track parameters, generated muons at the center of the streamer chamber with these parameters and let the muon "swim" through the apparatus to find values for the $\{ T^i \}$.

The program used to swim the particles through the apparatus is the same as the Monte Carlo simulation program described in Appendix II. In this version, however, there was no multiple scattering in the steel and no trigger counter checking. All particles with energy greater than 6 GeV and initial polar angle between .030 rad and .200 rad were allowed to swim through the apparatus until they either stopped in the steel or reached the end of the detector. Particles that passed out of the steel were allowed to drift to the end. Particles that passed into the hole were allowed to cross the hole. The Y and Z position of the particle was recorded at the X of each chamber regardless of whether the trajectory was inside the chambers' fiducial regions or not.

The Maximum Likelihood analysis was performed on the Cyber 175 computer at Fermilab with the aid of the program MINUIT [82]. For each event, the triplet points, their errors and the initial estimates of the track parameters obtained from the Second Pass Analysis were read by MINUIT. A search of the parameter space to minimize $-\ln(L)$ was first performed by the SIMPLEX routine and then by the routine MIGRAD which performs a functional minimization by a gradient search [82]. The covariance matrix was estimated by MIGRAD.

Many Monte Carlo studies were done to test the performance of the method. In the first test, we generated 100 events with a momentum of 15 GeV/c and polar angle of 90 mrad. The toroid mode and charge of the muons was such that the particles were focused. The acceptance of the spectrometer for muons of this type was 100%. The chamber hits generated from the Monte Carlo were read into the analysis program. The mean of the calculated momentum was 16.2 GeV/c and the spread of the distribution was

± 2.4 GeV/c. The mean of the distribution in polar angle was 91. mrad ± 6. mrad. The shift in the momentum distribution was too large to be merely a statistical effect.

It is known that the Maximum Likelihood method is often biased in situations when there are only a few experimental measurements. For example, in simultaneously estimating the mean and the error σ^2 of a population that is Gaussian-distributed, the estimate of the σ^2 is biased by an amount $-(1/n)\sigma^2$ were n is the number of measurements [63]. In the limit of large statistics, the bias becomes negligible. In our case, we have one measurement of the track. The amount of bias in the estimate of the momentum was found by further study of Monte Carlo generated events. For any generated momentum, the fitted momentum was too high. The results of the studies were mapped into a momentum correction table as a function of momentum and angle. Furthermore, it is interesting to note that we were able to artificially remove the bias by removing the momentum dependence of the average scattering angle θ_s in both the generating process and the fitting process, thus fixing the width of the probability density function.

The final results for the momentum were bias-corrected. The results obtained by evaluating the covariance matrix using the MINUIT routine MINOS, which directly calculates the covariance matrix, were the same as those obtained from MIGRAD. The likelihood function appeared to be symmetric about the maximum. The off-diagonal terms of the covariance matrix were small. Figures 8-3, 8-4, and 8-5 show the resolution for P, Θ and Φ as they were calculated for Monte Carlo events by the Likelihood Method. Note that since the fitting was done in 1/p, the quoted errors in p are not symmetric.

Tracks with momentum less than 7 GeV/c were discarded by a cut on the muon range in steel. Tracks with $-\ln(L) > 100$ were discarded. The likelihood as a function of momentum x charge is presented in Figure 6-3 for the data and the Monte Carlo.

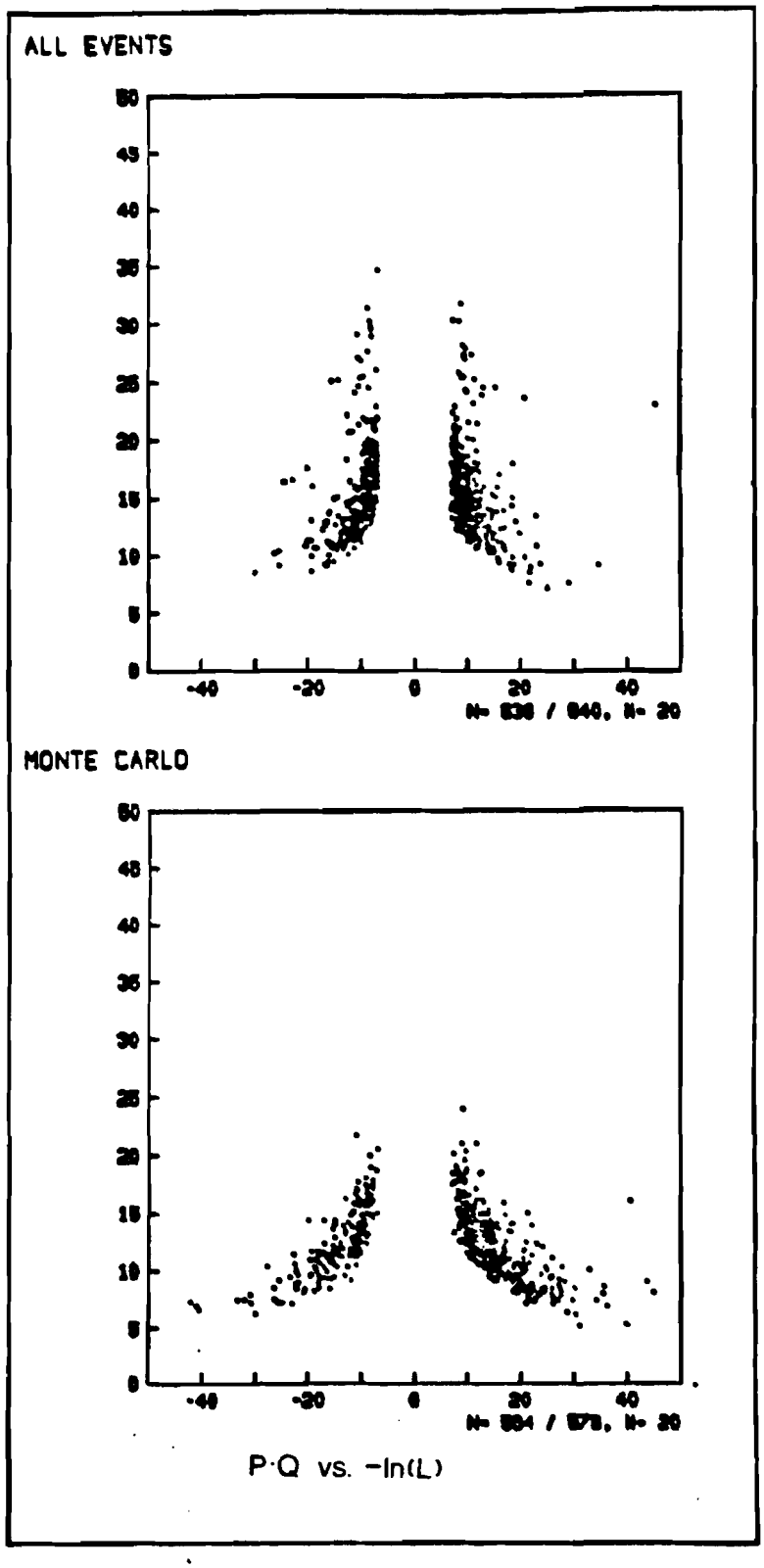

Figure 6-3: Scattergrams of momentum versus -ln(L) for a) the data, and for b) Monte Carlo events

6.7 A Summary of the Muon Selection

The 640 NIC̄V̄MU events in the "Matched" Muon sample passed the following cuts:

- Each event was selected for the initial scan list because there was at least one good muon selected in the First Pass Muon Analysis (See Section 6.1).
- The picture associated with the event contained a measurable fiducial interaction.
- At least one muon track from the event passed the refined muon cuts from the Second Pass Analysis (See Section 6.5)
- The muon track was consistent with the measured tracks in the pictures.
- The best fit muon track had momentum greater than 7 GeV/c.

Figure 6-4 and 6-5 give the Φ and Θ distributions of the best muon tracks from each event. The majority of the 640 muons candidates($\sim$90%) in this sample are attributed to pion decay and hadron punch-through.

A list of the momentum and angles of the best track from each of the final 23 events is given in Appendix III. A check was made to see if any event had two or more tracks. Two tracks were considered independent if they were made from two independent sets of triplets. No two track events were found in the sample of 23 candidate events.

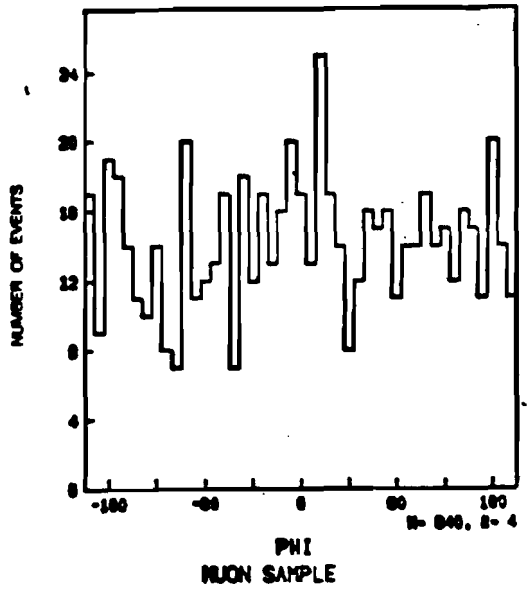

Figure 6-4: The distribution in azimuthal angle of all NIC̄V̄MU events in the Matched Muon sample

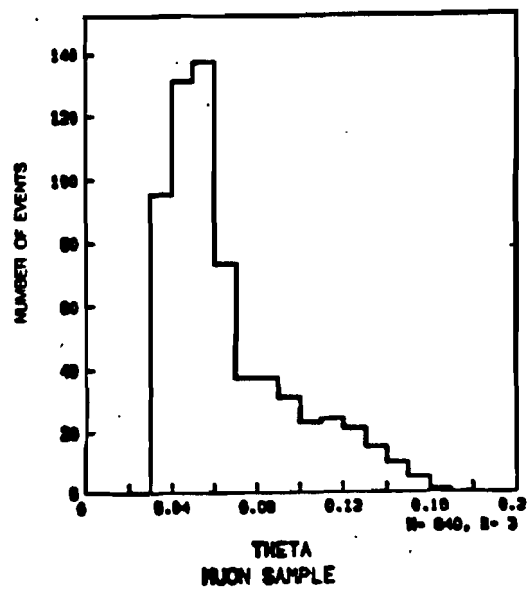

Figure 6-5: The distribution in polar angle of all NIC̄V̄MU events in the Matched Muon sample

Chapter 7

RESULTS AND CONCLUSIONS

The final data sample was defined by a combination of the results of the film analysis outlined in Chapter Five and the muon analysis outlined in Chapter Six. Altogether, twenty-three charm candidates were selected from the whole data sample. The number of background events among the candidates has been found to be 5.68 events.

A synopsis of the event selection procedure is as follows:

1. Events were selected by an on-line trigger. (P_{muon}>6.5 GeV/c and 30 mrad < θ < 250 mrad).
2. Good muon events were selected by a least-squares fit to the upstream segment of the muon track and a cut on the change in azimuthal angle (ϕ) through the toroid ($\Delta\phi < 40^\circ$).
3. The muon requirements were refined to include fiducial volume cuts to assure that the muon remained in the steel.
4. The final muons' momenta must have been greater than 7 GeV/c.
5. All events passing cuts 1-4 with fiducial interactions were measured. Each event was measured in two views.
6. The measured events must have a topology such that two measured tracks had angles greater than 150 mrad in the horizontal plane in both views that define the primary vertex and at least one track with angle less than 150 mrad in both views.
7. All events with the correct topology and a track with angle less than 150 mrad with a vertex miss distance S satisfying the condition that $S/\Delta S > 3.0$ were scanned for mismeasurements.

The final sample of 23 candidate events with $S/\Delta S > 3.0$ taken from 362 NIC̄ν̄MU

events that passed the topology cut can be compared to a sample of 14 candidates from a sample of 892 ordinary interactions (NIC̄V̄ events) that were obtained in the same way (steps 5-7). These events measure the backgrounds in the NIC̄V̄MU pictures due to measurement errors and strange particles [112].

The measured distribution of the polar angle of the muons from the 23 events is shown in Figure 7-1. The distribution of the azimuthal angle of the muons is given in Figure 7-2.

The contribution due to the background in the muon distributions for the 23 events was estimated from the muon tracks taken from a sample of 140 NIC̄V̄MU events with $1.0 < S/\Delta S < 2.0$. In this region, the estimated number of events containing charmed particles was less than 5%. We scaled the background muon distributions to correspond to the 5.68 expected background events in the 23 candidates. The background distributions were then added to the Monte Carlo distributions that were scaled to correspond to the 17.32 signal events.

The results included in this chapter are an analysis of the production models based on the charge ratios of the muons, a comparison of the measured momentum spectrum and P_t spectrum of the muons to the spectrum predicted by the standard decay model, and an analysis of the average lifetime of the charm decays.

7.1 Production Characteristics

Charm production properties are reflected in the decay muon distributions. One way to compare different models is to look at each model's predictions for the muon charge fractions. In this experiment, we measured four classes of muon events: events with positively charged muons in the +1 toroid mode (++), muons with a negative charge in the +1 toroid mode (−+), muons of positive charge in the -1 toroid mode (+−), and muons of negative charge in the -1 toroid mode (−−). 54% of the raw ungated NIC̄V̄ triggers were recorded in the +1 toroid mode where positive charges were focused. We used the number of ungated NIC̄V̄ triggers to estimate the flux to which the apparatus

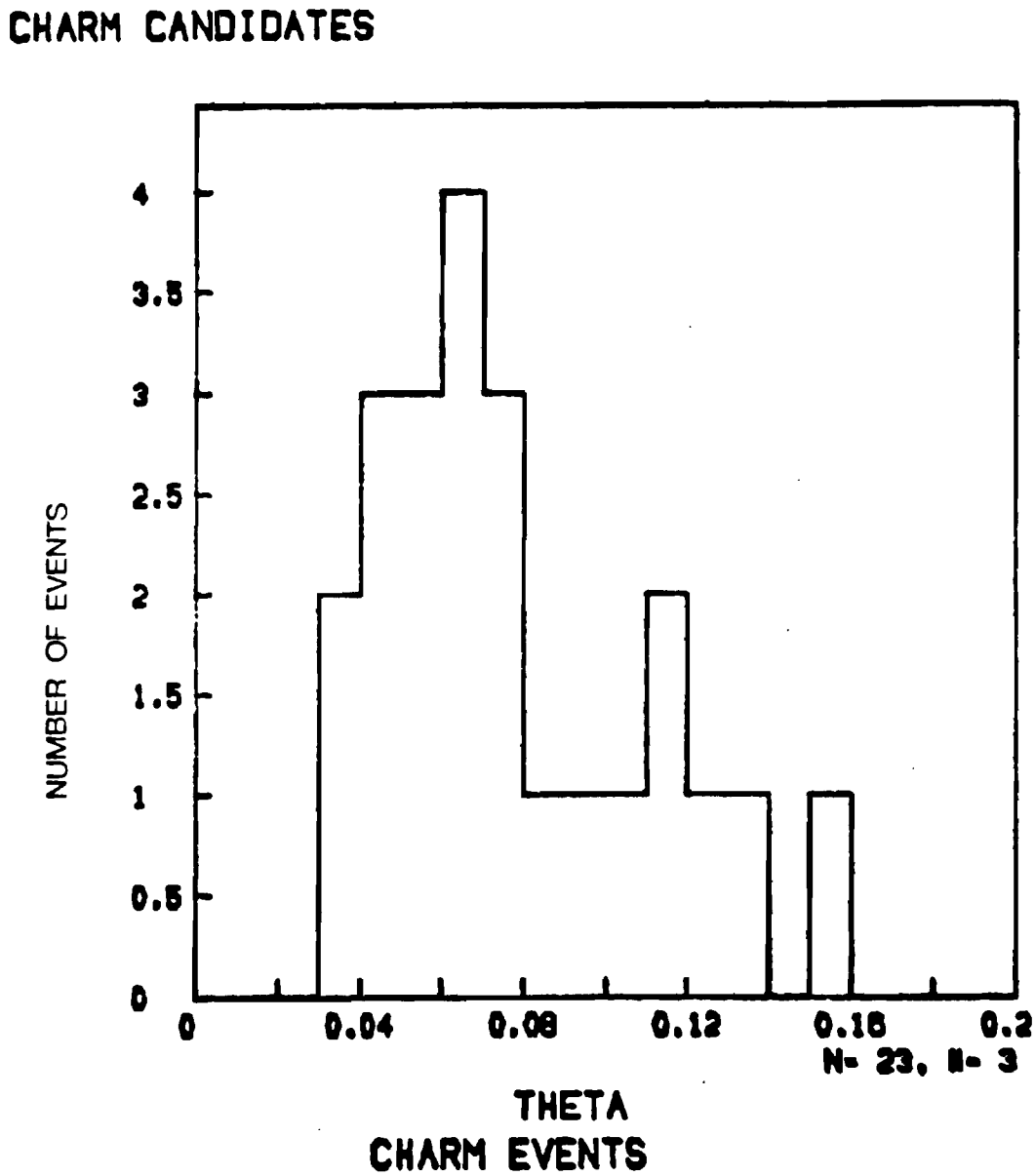

Figure 7-1: The distribution of the polar angle θ of the muons from the 23 candidate events

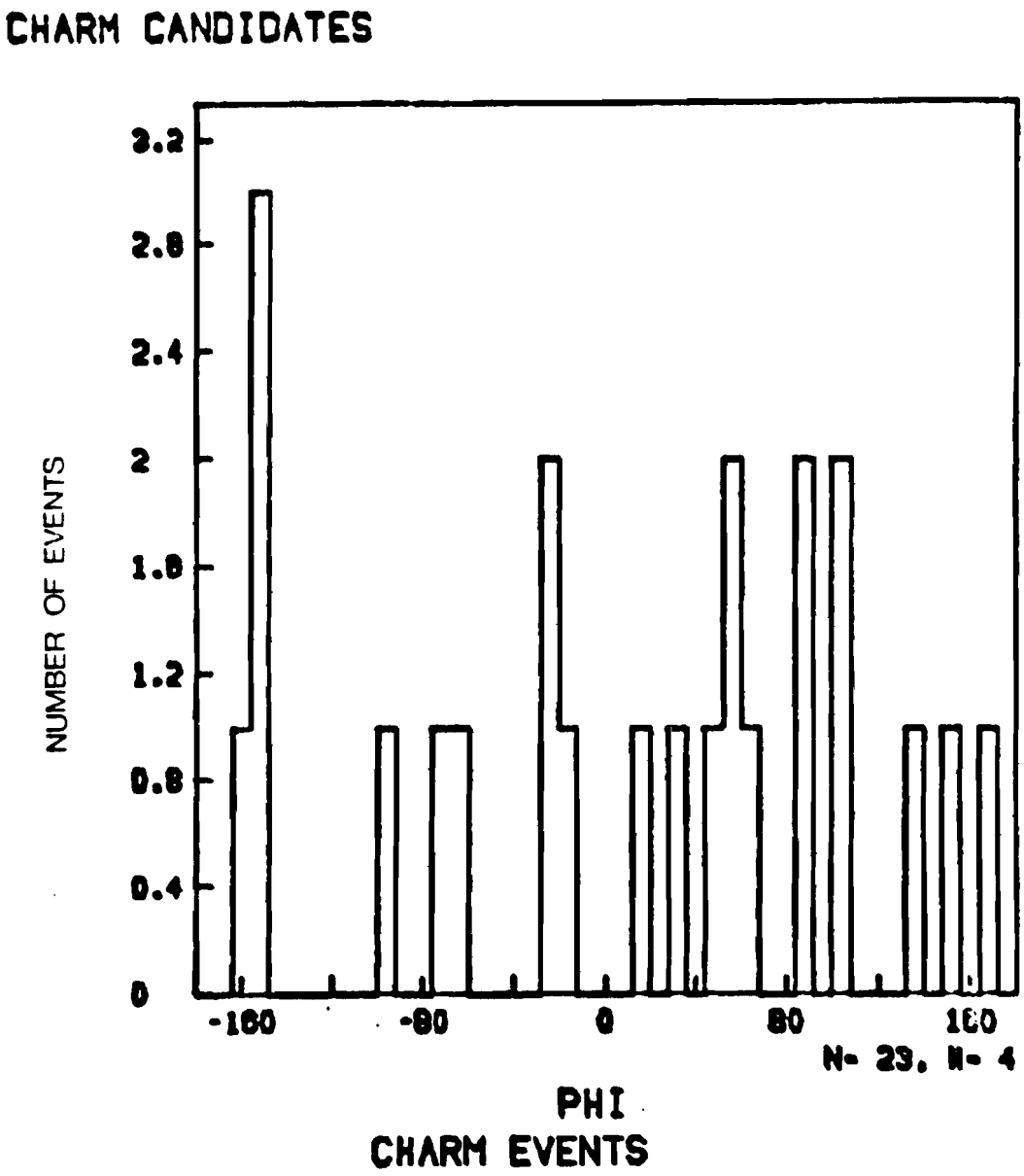

Figure 7-2: The distribution of the azimuthal angle ϕ of the muons from the 23 candidate events

was exposed in each toroid polarity. The momentum spectra of the 23 candidate events separated by charge and mode are shown in Figures 7-3 and 7-4.

For a model of central charm production, with x_F dependence of $(1 - |x|)^5$ for $D\bar{D}$ production, we expected to see an excess of defocusing muons of 3 to 2 in comparison to focusing particles. This ratio is 2 to 1 for more diffractive production models with a $D\bar{D}$ pair produced with $(1 - |x|)^1$ dependence. Furthermore, we expect the measured charge ratio of positive to negative muons to be approximately 1:1 for central production and 2:3 for diffractive models.

For eight models of charm production, we compiled the fraction of Monte Carlo events accepted in each of the four categories mentioned above. In order to directly compare the predicted fractions with the measured fractions, we corrected the fractions predicted by Monte Carlo simulations for each charm production model with the measured background charge and mode fractions. For each model, the probability of obtaining the measured result (L_0) was calculated. In addition, the probability of obtaining results more deviant than the measured result ($P(L<L_0)$) was calculated. We can define the quantity α as the significance to which we can reject a hypothesis. If $P(L<L_0) \leq \alpha$, we can reject a hypothesis with a significance level of α.

The statistical evaluation of a set of binned data of low statistics can be performed using a multinomial distribution in which the total number of events is Poisson-distributed. The resulting distribution is the product of Poisson distributions; k being the number of bins.

$$P(r_1,\ldots r_k,n) = \prod_i \frac{1}{r_i!}(\nu p_i)^{r_i} e^{-\nu p_i}$$

ν = mean number of events measured
n = total number of events measured in this experiment
r_i = number of events measured in each bin
p_i = probability of measuring an event in bin i

The probability density function is useful in studying histograms and data sets split into independent categories.

The measured fractions are summarized in Tables 7-1 and 7-2.

	Charge	Mode	Number	Fraction
Charm	+	+	11	0.478
Candidates	−	+	3	0.130
	+	−	5	0.217
	−	−	4	0.174
Total			23	
Background	+	+	30	.214
	−	+	38	.271
	+	−	51	.364
	−	−	21	.150
Total			140	

NOTE: Toroid Mode (+) means positive muons are focusing.

Table 7-1: The Charge and Mode ratios of the 23 charm candidates and the background events

The measured results indicate an excess of positive muons of more than 2 to 1. If one looks at the fraction of positive muons ($A_c^{Meas} = (N_{++}+N_{+-})/N_{tot}$) and the fraction found in the mode where positive focus ($A_m^{Meas} = (N_{++}+N_{-+})/N_{tot}$), we find that the Monte Carlo predictions of these ratios for $D\bar{D}$ production $(1 - |x|)^3$ and $(1 - |x|)^5$ are consistent with the data: $P(A_c > A_c^{Meas}$ or $A_m > A_m^{Meas}) = 50\%$ for these two models. However, by considering the correlations between the mode and the charge, we are able to compare the different models.

Making a cut at the $(1-\alpha) = 95\%$ level, we find that the data are consistent with two models. In the best model, the D, which contains a $c\bar{q}$, is produced centrally with a $(1 - |x|)^7$ distribution, and the $\bar{D}$, which contains a $\bar{c}q$, is produced with a $(1 - |x|)^1$ distribution characteristic of a leading particle. This model describes the the charge ratio for the muons from the 23 candidate events, but more importantly it is consistent with the charge and mode dependence together.

The model $(1 - |x|)^7(1 - |x|)^1$ is not consistent with the results of the prompt muon

MODEL		CHARGE MODE	FRACTION	L_o	$P(L<L_o)$
Λ_c^+	$(1 - \|x\|)^1$	++	0.096	3.7×10^{-9}	1.2×10^{-5}
$\bar{D}$	$(1 - \|x\|)^3$	−+	0.434		
		+−	0.241		
		−−	0.229		
Λ_c^+	$(1 - \|x\|)^1$	++	0.108	6.5×10^{-9}	2.3×10^{-5}
$\bar{D}$	$(1 - \|x\|)^5$	−+	0.465		
		+−	0.203		
		−−	0.224		
D	$(1 - \|x\|)^1$	++	0.185	2.3×10^{-6}	0.014
$\bar{D}$	$(1 - \|x\|)^1$	−+	0.329		
		+−	0.329		
		−−	0.157		
D	$(1 - \|x\|)^3$	++	0.205	4.7×10^{-6}	0.029
$\bar{D}$	$(1 - \|x\|)^3$	−+	0.324		
		+−	0.324		
		−−	0.147		
D	$(1 - \|x\|)^5$	++	0.237	15.7×10^{-6}	0.085
$\bar{D}$	$(1 - \|x\|)^5$	−+	0.323		
		+−	0.279		
		−−	0.160		
D	$(1 - \|x\|)^7$	++	0.199	4.8×10^{-6}	0.031
$\bar{D}$	$(1 - \|x\|)^7$	−+	0.325		
		+−	0.299		
		−−	0.176		
D	$(1 - \|x\|)^5$	++	0.202	5.2×10^{-6}	0.032
$\bar{D}$	$(1 - \|x\|)^3$	−+	0.309		
		+−	0.330		
		−−	0.159		
D	$(1 - \|x\|)^7$	++	0.263	26.4×10^{-6}	0.117
$\bar{D}$	$(1 - \|x\|)^1$	−+	0.225		
		+−	0.395		
		−−	0.117		

Table 7-2: The Charge / Mode Fractions for eight Charm production models.

experiment at Fermilab [96] which measures an x_F dependence of $(1 - |x|)^5$ for forward production of $D\bar{D}$ in p-Fe collisions at 350 GeV/c. We do find, however, that the

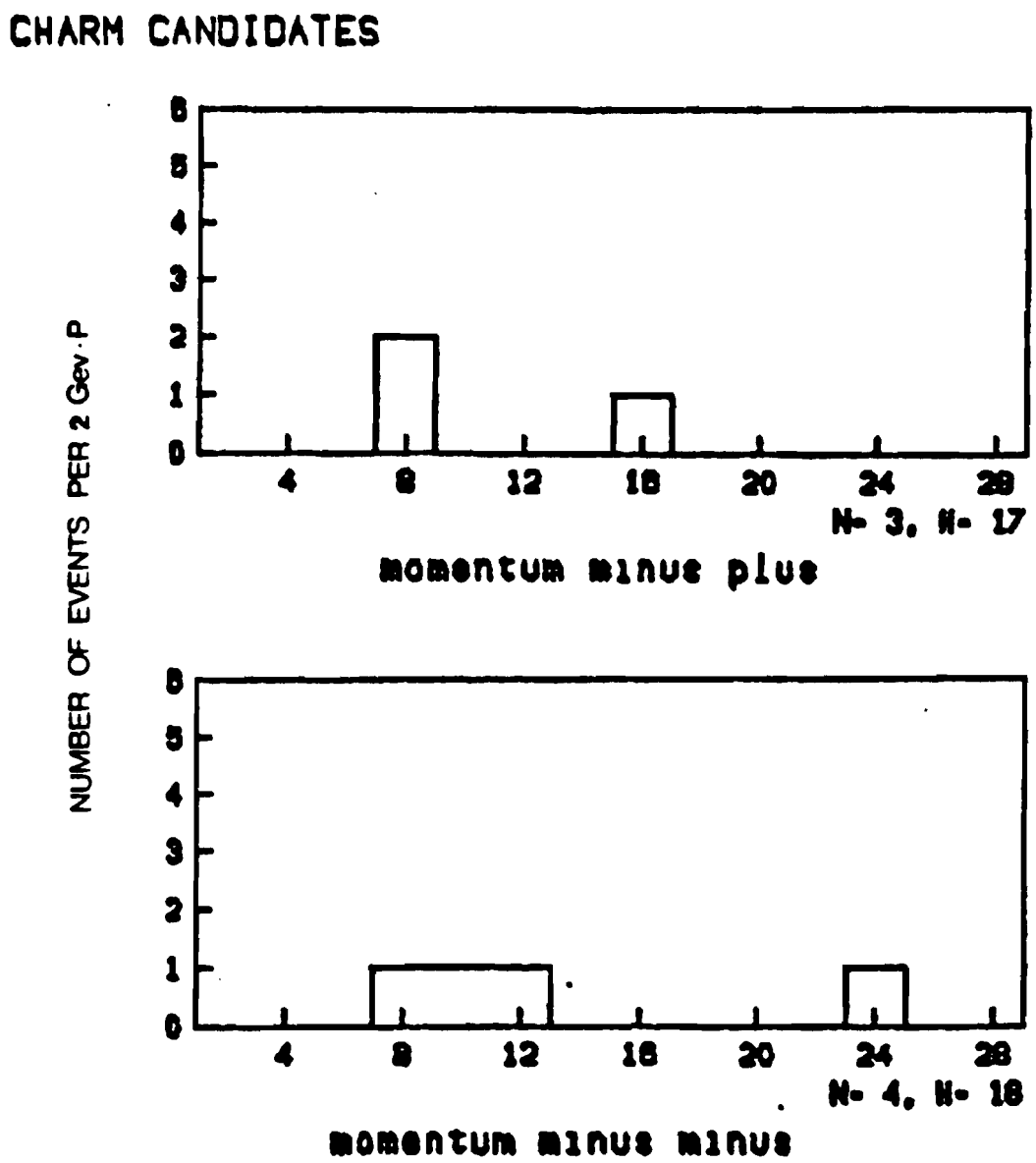

Figure 7-3: The momentum spectra for the charge mode categories (−+) and (−−)

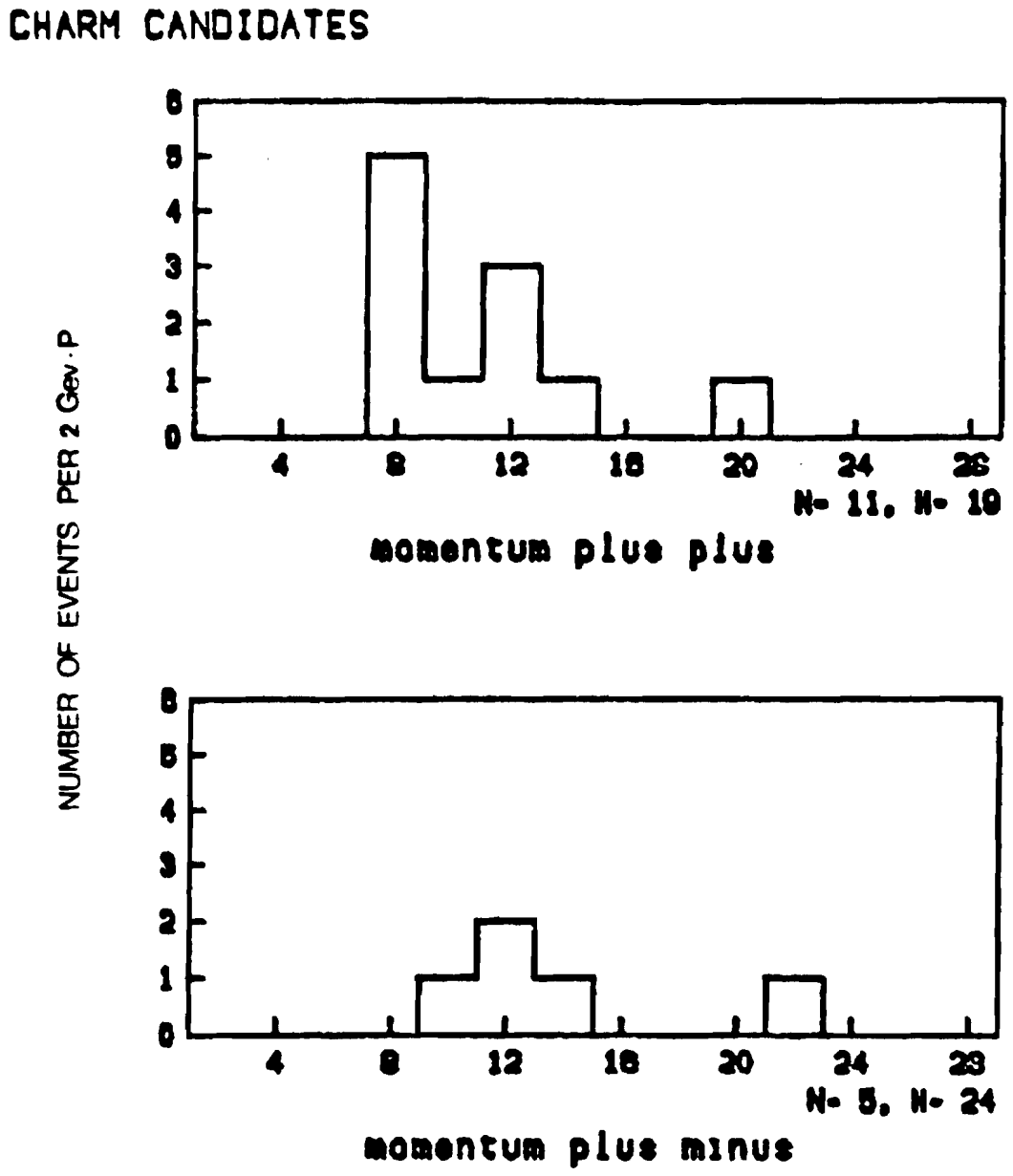

Figure 7-4: The momentum spectra for the charge/mode categories (++) and (+−)

$(1 - |x|)^5$ distribution also makes a good fit to our data. We do not favor $(1 - |x|)^2$ production of $D\bar{D}$ pairs as was found by the LEBC Collaboration in p-H_2 collisions at the SPS at CERN [8].

In Λ_c^+ production models the Λ_c^+(cud) is produced with a x_F distribution of $(1 - |x|)^1$. It is thought that the c quark recombines with two valence quarks in the original hadrons. The $\bar{D}$ recombines with only one valence quark and is produced with a $(1 - |x|)^3$ or $(1 - |x|)^5$ distribution. If $\Lambda_c^+\bar{D}$ production were the main production mechanism, we would expect to see an excess of μ^- from the decay of the $\bar{D}$ since the muon from Λ_c^+ decay would be inside the hole in the hadron shield. We can rule out $\Lambda_c^+\bar{D}$ as the dominant production mechanism in n-Ne collisions at these energies.

The other models are consistent with our data, but the agreement is not overwhelming. In discussing further results, we will compare the measured spectrum with both the $(1 - |x|)^1(1 - |x|)^7$ and $(1 - |x|)^5(1 - |x|)^5$ production model predictions.

7.2 The Momentum Spectrum

The momentum spectrum of the muons from the 23 candidate events is shown in Figure 7-5. In Figures 7-6 and 7-7, the momentum spectrum is compared to the predicted spectrum from the production models $(1 - |x|)^7(1 - |x|)^1$ and $(1 - |x|)^5(1 - |x|)^5$. The background has been added to the Monte Carlo data so that a direct comparison is possible. The spectrum derived from the data has not been corrected for the acceptance of the apparatus; the model predictions reflect the detector acceptance which is included in the Monte Carlo. The measured spectrum is consistent with the Monte Carlo spectra of the two models ($P(L<L_o) \simeq 0.30$).

By studying the $P_t = P \sin\theta$ spectrum, we are able to study the decay mechanism of the charmed particles. In order to compared our muon spectra with electron spectra from charm decays observed at e^+e^- machines, we must include the effects of production kinematics and acceptance for our data. Production models predict a e^{-bp_t} dependence for charmed hadron production. Here, we have assumed $b=2.5(\mathrm{GeV}/c)^{-1}$, as is used in

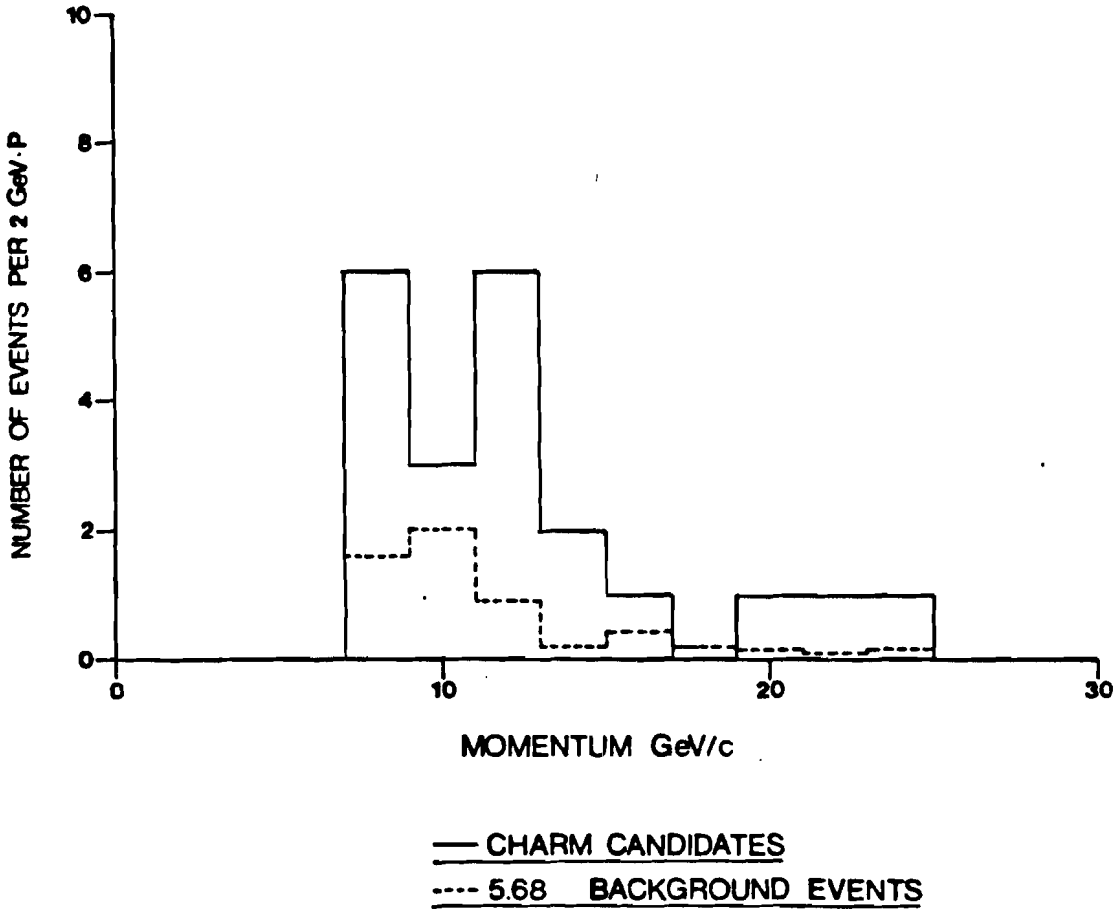

Figure 7-5: Muon Momentum Spectrum for the Charm Candidates

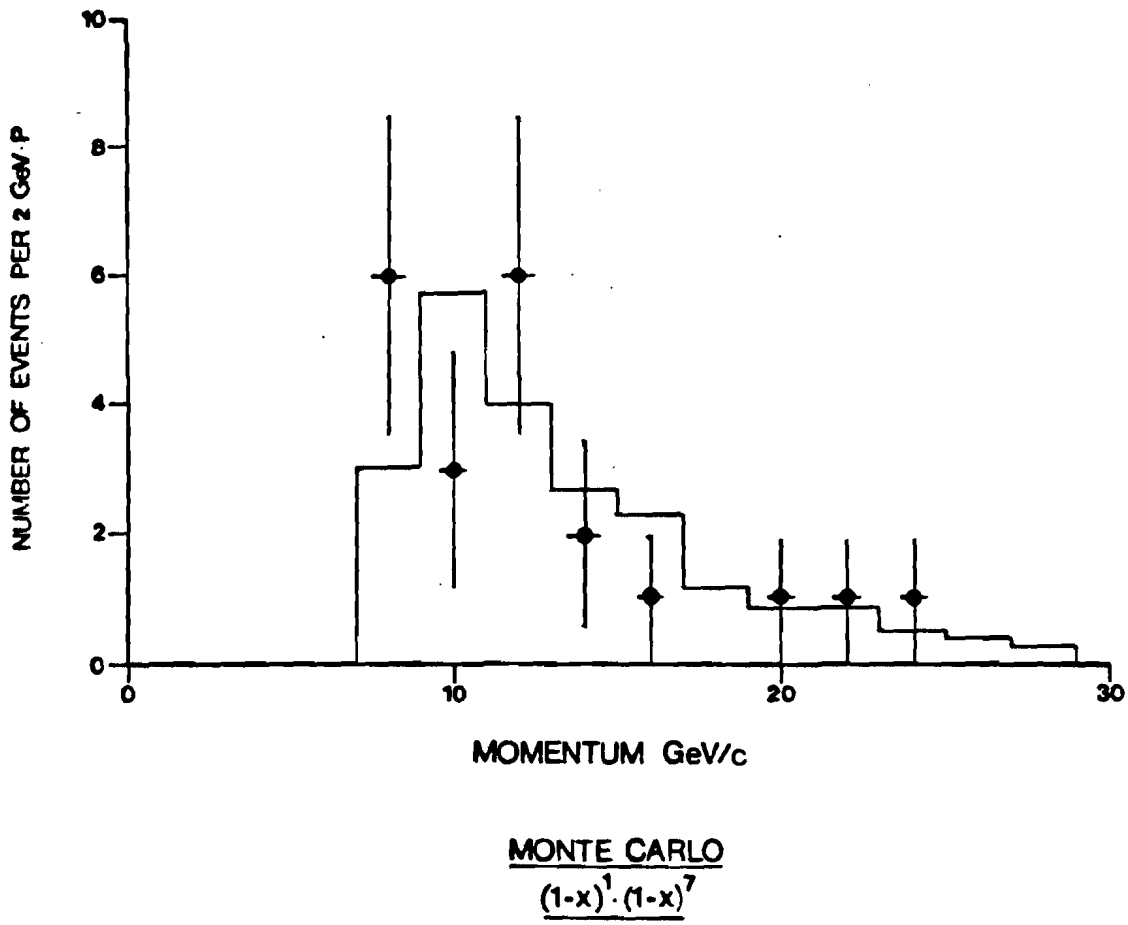

Figure 7-6: Measured Muon Momentum spectrum as predicted by the production model $(1 - |x|)^7(1 - |x|)^1$ for $D\bar{D}$ pairs. The data points, with errors, are also shown

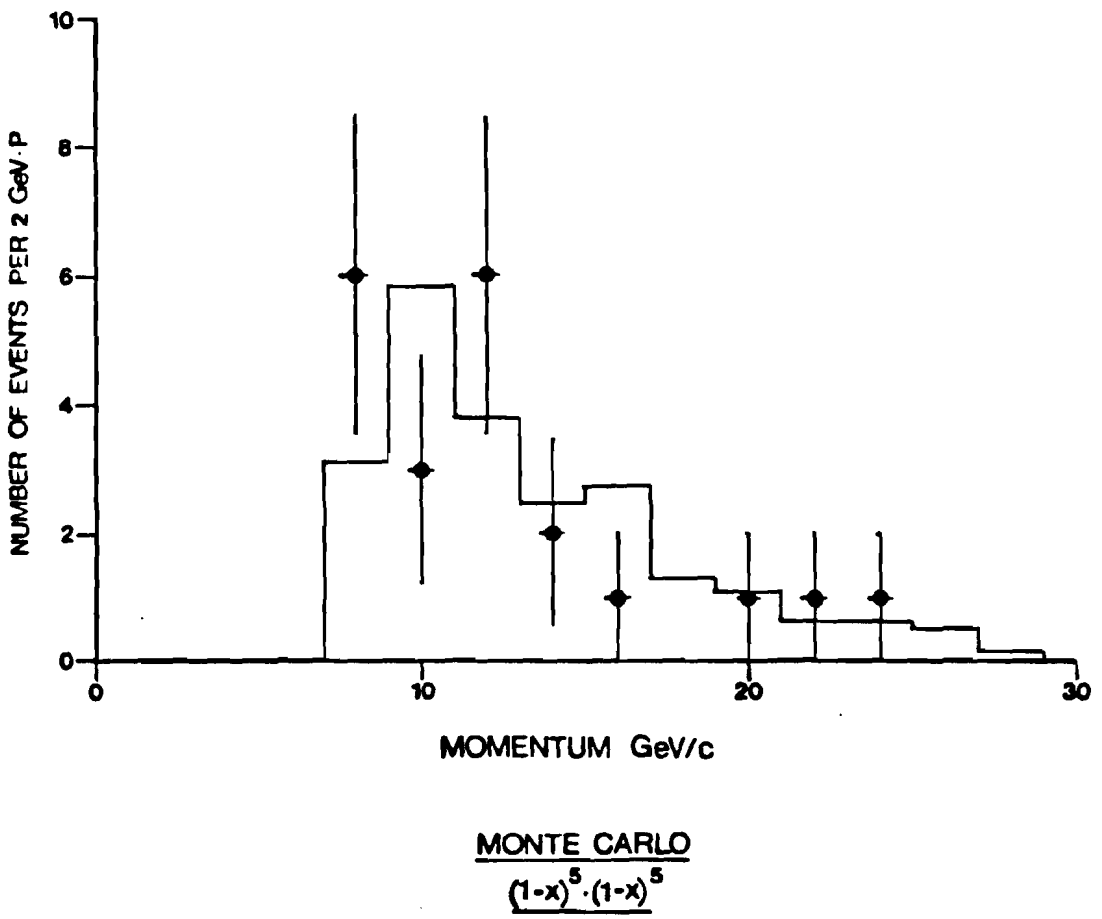

Figure 7-7: Measured Muon Momentum spectrum as predicted by the production model $(1 - |x|)^5(1 - |x|)^5$ for $D\bar{D}$ pairs. The data points, with errors are also shown

the fusion model. This value fits the P_t spectrum measured by the prompt muon experiment at Fermilab [96]. This also fits the distribution in P_t measured by LEBC, although they quote a P_t^2 dependence for the differential cross section. The decay spectrum, assuming μ-e universality, should be the spectrum indicative of the three body β decay of the charmed hadron into $\mu\nu_u$ + one hadron.

The momentum spectrum in the center of mass of electrons from charm decay has been measured by the DELCO Collaboration in an e^+e^- experiment at 3.77 GeV. Their results, which are corrected for acceptance, are presented in Figure 7-8. The overlying curve is taken from the electron energy spectrum in our Monte Carlo. The electron energy in the Monte Carlo is "measured" in the center of mass of the parent charmed hadron (D or $\bar{D}$). The curve is for the three-body semi-leptonic β decay of a charmed meson in which $D \rightarrow Ke\nu$ (50%) and $D \rightarrow K^*(890)e\nu$ (50%). We use the same decay model for generating semi-leptonic muon decays.

The measured P_t spectrum is presented in Figure 7-9. The spectrum is compared to the background adjusted Monte Carlo predictions in Figures 7-10 and 7-11. The P_t spectrum of the background is presented in Figure 7-12.

The measured spectrum reflects the original lepton spectrum folded with the acceptance of the entire detector and analysis programs. The acceptance of trigger is folded with the acceptance of the $S/\Delta S$ analysis to obtain the acceptance curve shown in Figure 7-13.

We conclude that the measured spectrum is consistent with the predictions of the production and decay models. ($P(L<L_o)$=60% for $(1 - |x|)^5$ and $P(L<L_o)$=30% for $(1 - |x|)^7(1 - |x|)^1$ production). Our results are consitent with the hypothesis of μ-e universality in charm decay.

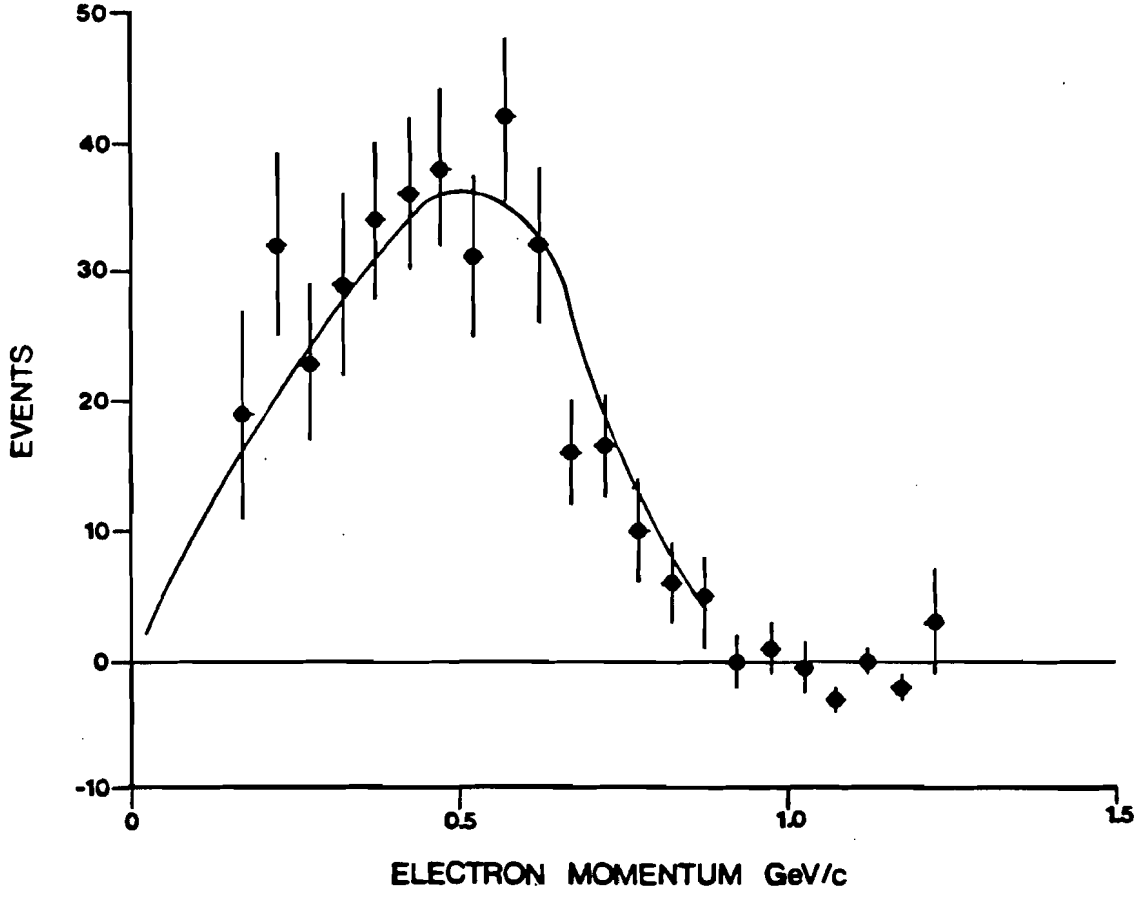

Figure 7-8: The electron energy spectrum measured by the DELCO Collaboration at 3.77 GeV. The curve is the spectrum of electrons in the center of mass frame of the charmed meson in our Monte Carlo simulation.

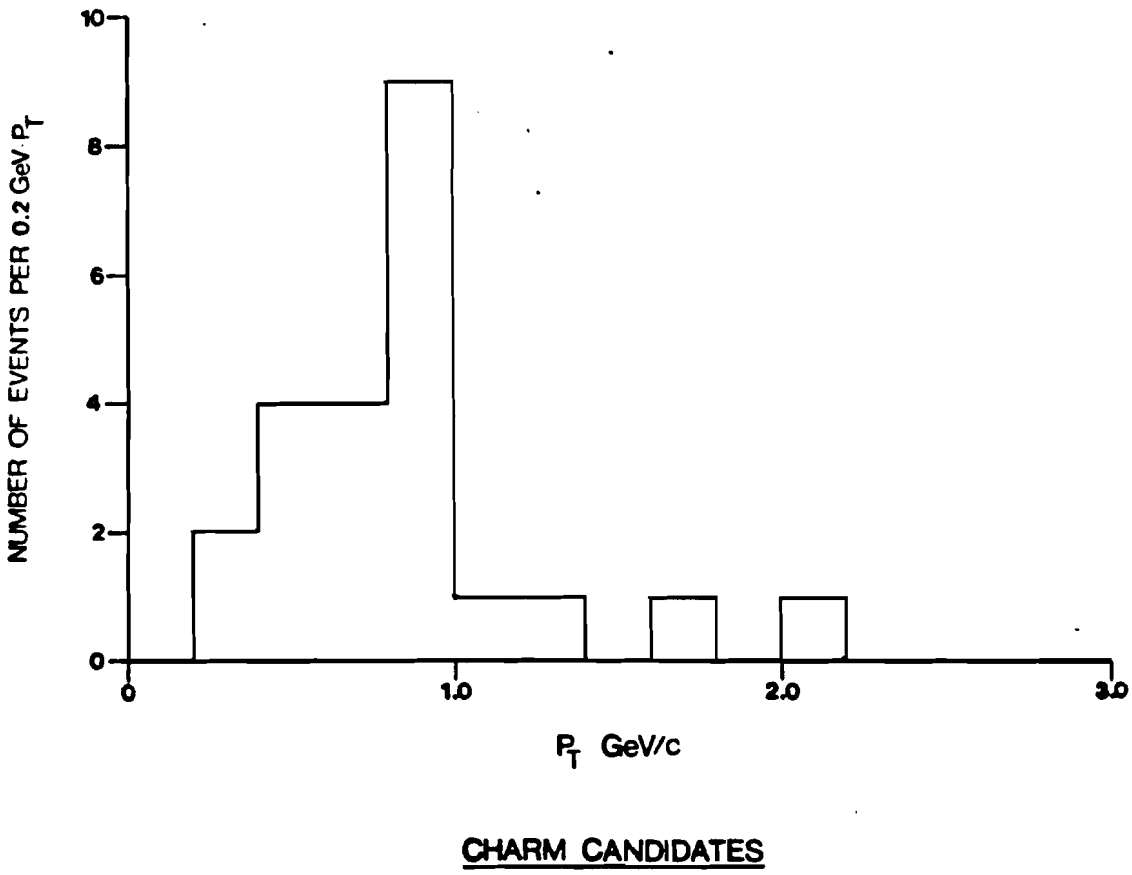

Figure 7-9: The measured P_t spectrum of the 23 Charm Candidates. The average value of P_t is 0.81 GeV/c (background corrected).

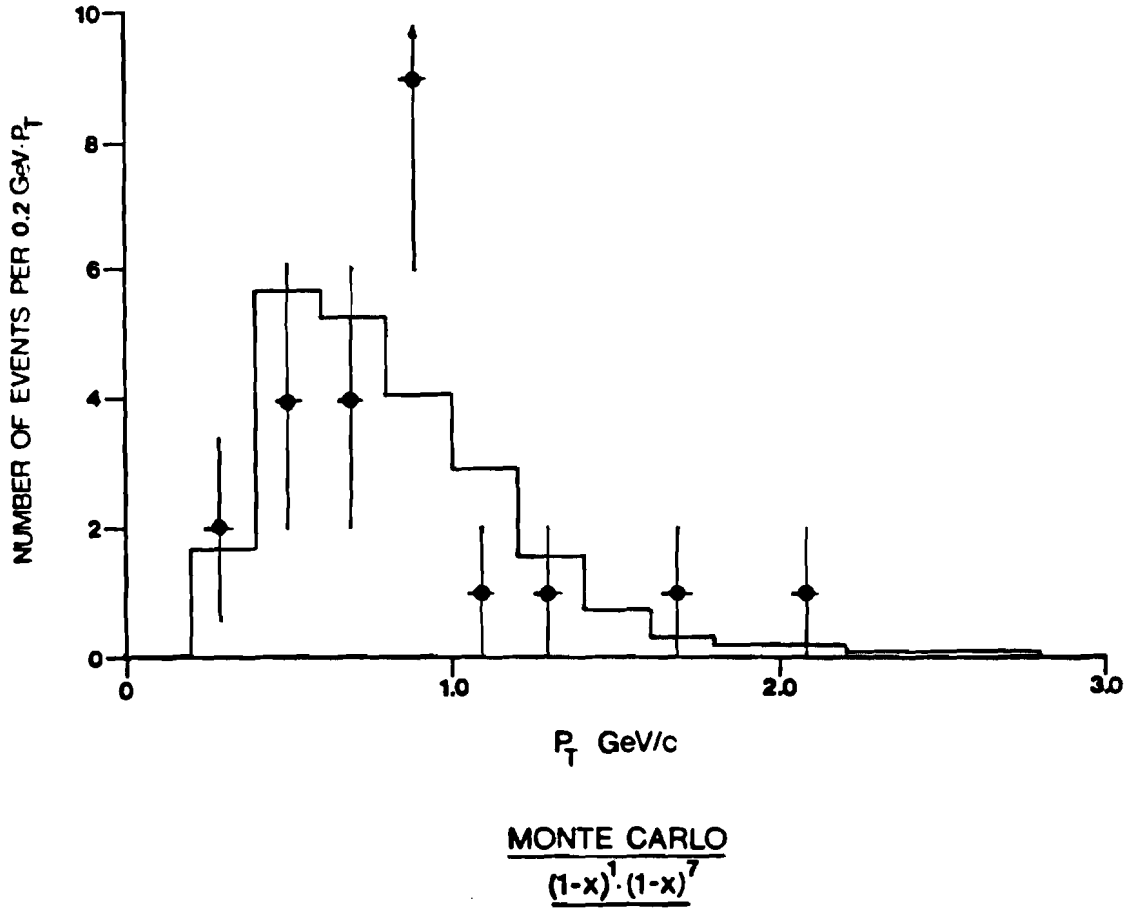

Figure 7-10: The background added P_t spectrum predicted by the production model $(1 - |x|)^7(1 - |x|)^1$ for $D\bar{D}$ pairs.
The data points and errors are also shown.

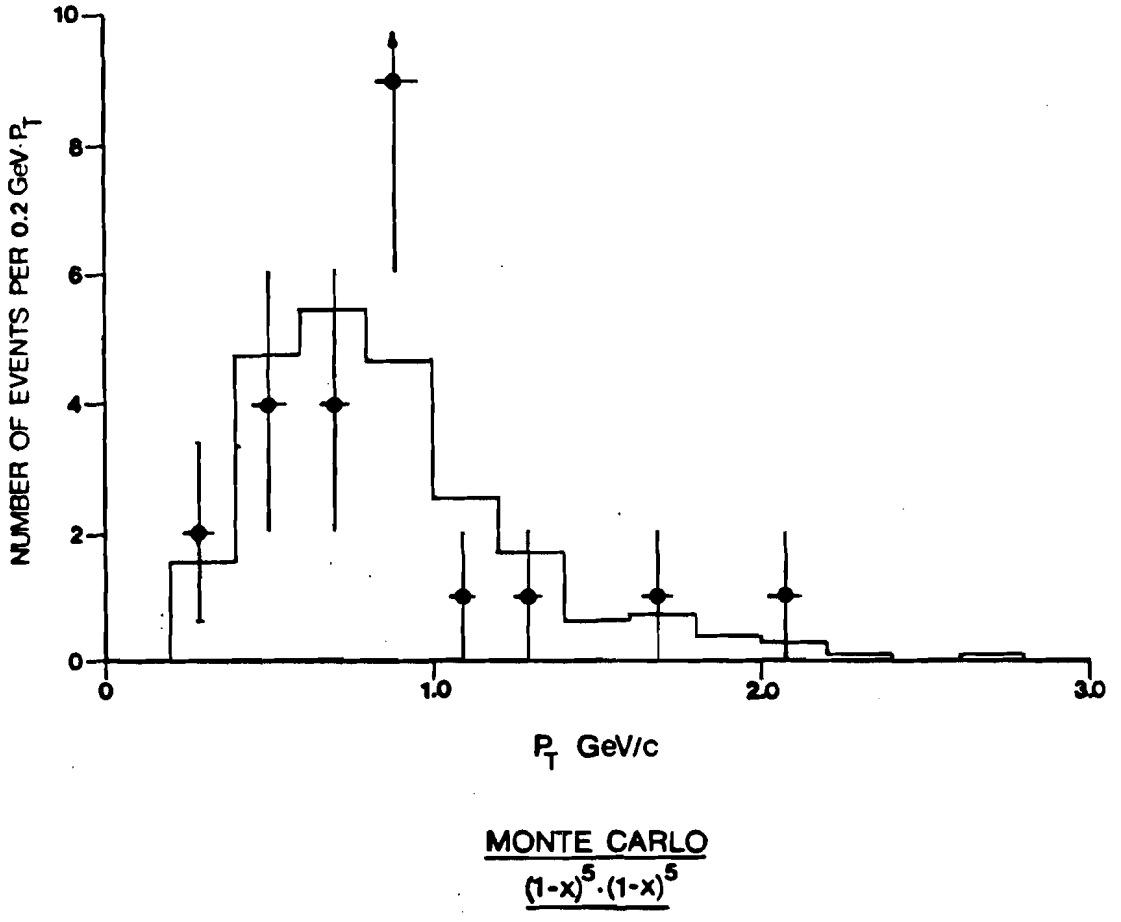

Figure 7-11: The background added P_t spectrum predicted by the production model $(1 - |x|)^5(1 - |x|)^5$ for $D\bar{D}$ pairs.
The data points and errors are also shown.

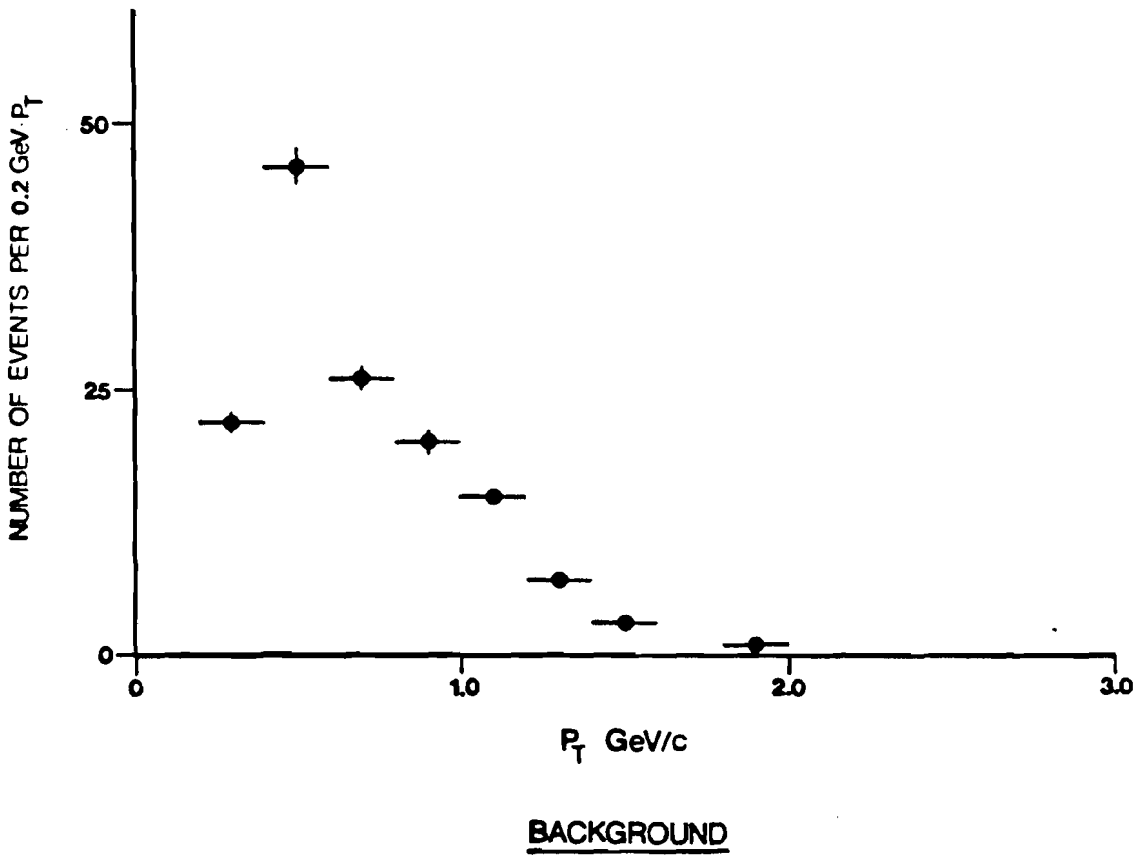

Figure 7-12: The P_t spectrum of the 140 background muon events

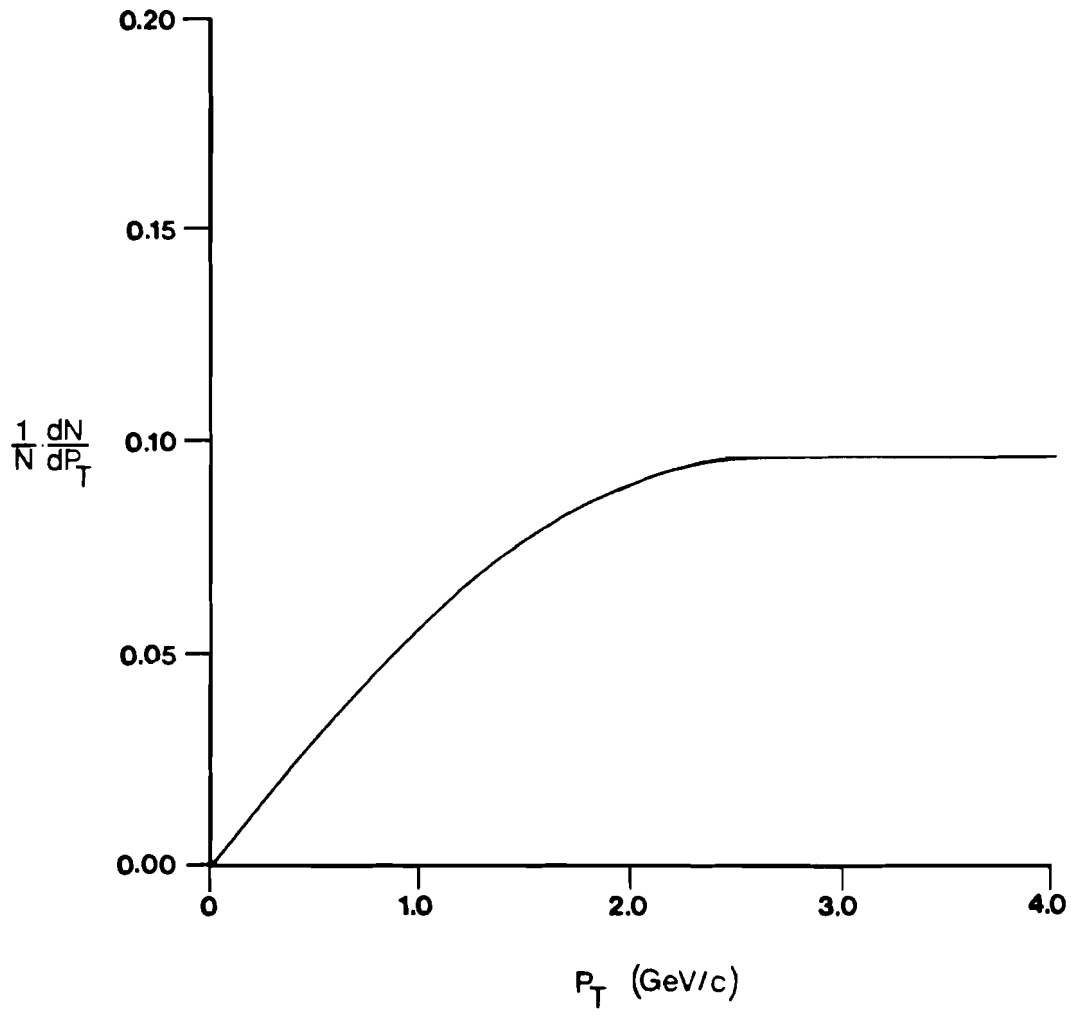

Figure 7-13: The acceptance in P_T for charm taking into account the trigger and the $S/\Delta S$ analysis

7.3 The Average Charm Lifetime

None of the charm candidates contained a visible decay vertex. Because we are not able to distinguish between charged and neutral decays, we measured an average charmed meson ($D\bar{D}$) lifetime. We measured the S ≡ miss distance of a track ≡ $\gamma c \tau \beta \sin\theta_{lab}$ for each track. The miss distance is approximately an invariant for relativistic decays [49, 90]. Compiling the miss distances of the tracks with the largest $S/\Delta S$ from each event, we plotted the distribution in Figure 7-14. We compared the measured distribution to the distributions predicted by five different Monte Carlo simulations of $D\bar{D}$ decays with six different single lifetimes, but always keeping the average semi-leptonic branching ratio equal to 8%. The miss distance distributions of the "measured" Monte Carlo charm events were fitted to the form

$$\frac{dN}{dS} = A_1 s^{b_1}\left(A_2 e^{-c_1 s} + e^{-c_2 s}\right).$$

The two exponentials come because of contributions to the miss distance from measurement error and from the charm lifetime. The shape of the background in the S distribution due to mismeasurement of single vertex events was estimated from a Monte Carlo simulation of measured single vertex events. The resulting S distribution was fitted to the form

$$\left(\frac{dN}{dS}\right)_o = A_o s^{b_o} e^{-c_o s}$$

The strange particle background was added to single vertex background by fitting

$$\left(\frac{dN}{dS}\right)_{BCK} = f\left(\frac{dN}{dS}\right)_o + (1\text{-}f)\ \text{constant}$$

to the measured miss distance distribution of the $NI\bar{C}\bar{V}$ events. Here, the strange particle contribution is approximated by a constant. The magnitude of the contribution is determined by the measured background $NI\bar{C}\bar{V}$ events. The estimated contribution of the 5.68 background events to the measured miss distribution of the 23 candidates is $(dN/dS)_{BCK}$ scaled to correspond to 5.68 events.

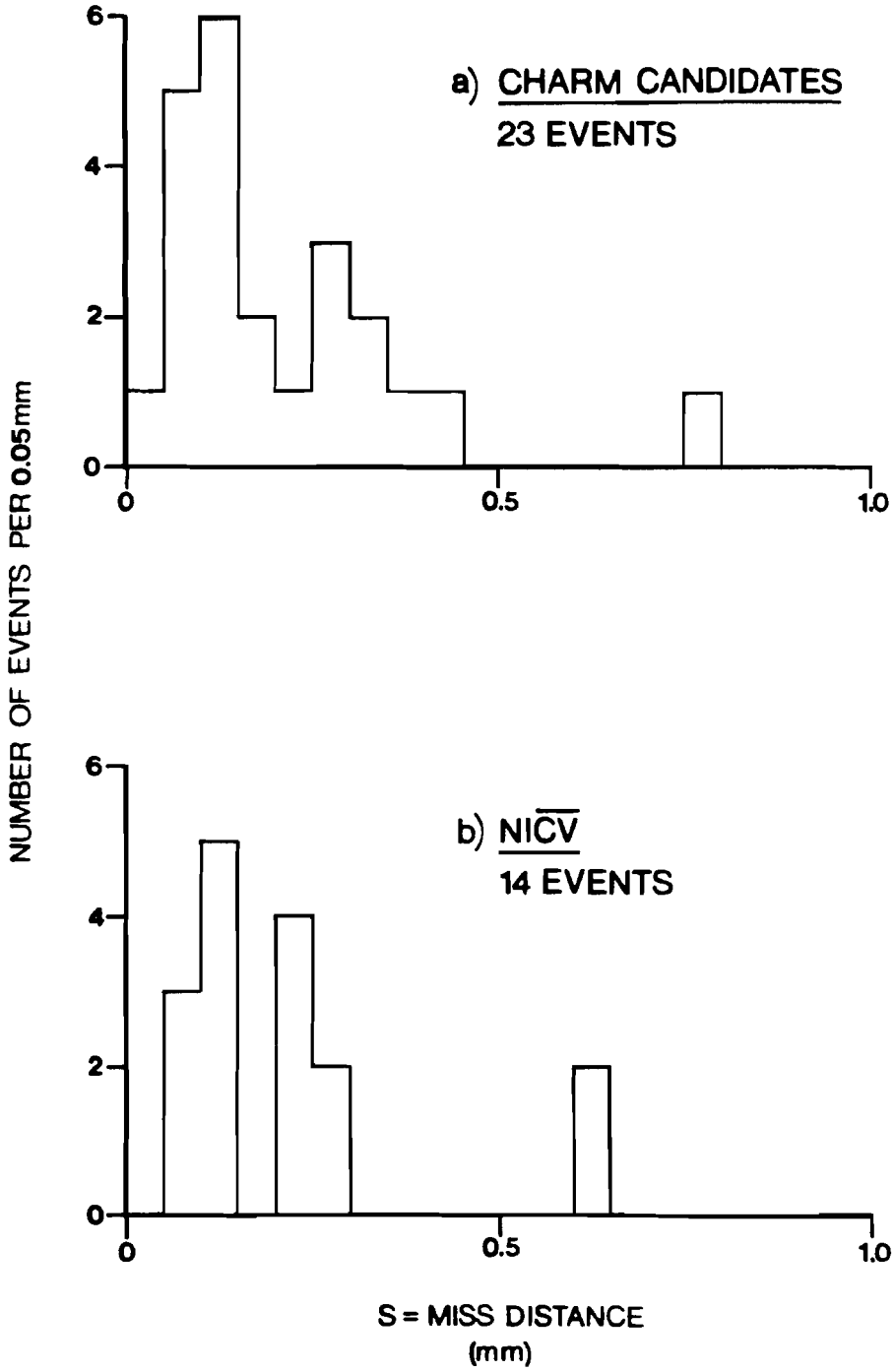

Figure 7-14: The miss distance (S) distribution for the a) Charm Candidates b) 14 NIC̄V̄ events

With the method of Maximum Likelihoods, we found the best fit value of the average lifetime. The values of the likelihood function are shown in Figure 7-15 and in Table 7-3.

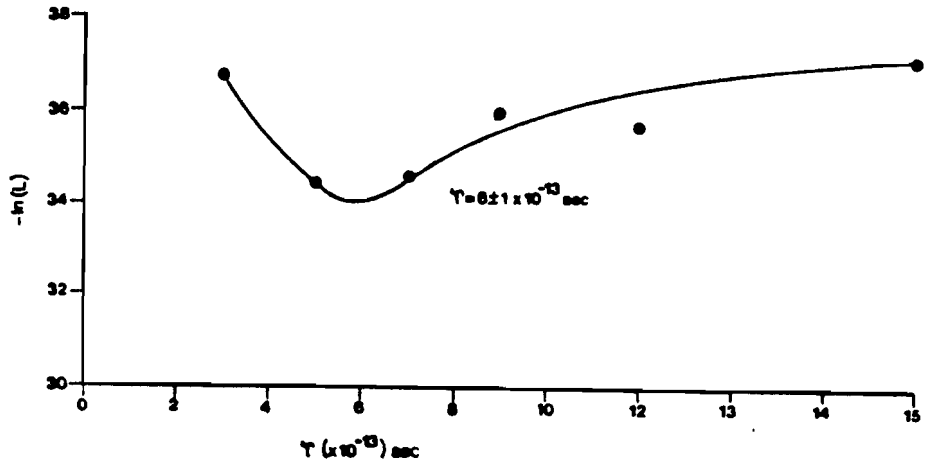

Figure 7-15: Plot of the - ln (L) for single lifetime fits to the measured miss distance distribution.

The average lifetime of the D lifetime is thus measured as $(6.0 \pm 1.0)\times10^{-13}$ sec. where the error is purely statistical. The error in the semi-leptonic branching ratio has not been considered. The integral distribution of the miss distance is shown in Figure 7-16. The Kolmogorov-Smirnov test [63, 57] for comparing data with small statistics with integral distributions indicates that the results are quite consistent with the hypothesis of a single lifetime. The probability of obtaining our result, given that the hypothesis of a single lifetime of 6×10^{-13} sec is true, is approximately 40%. Our value of the lifetime is in good agreement with the average value of the D^+ and D^0 lifetimes. See Figure 7-17 for a comparison of our results to the prediction of the model in which the charged and neutral D lifetimes are assigned according to the world averages for these lifetimes. The current world averages for the two lifetimes are

Lifetime	Likelihood	-Ln(L)
3×10^{-13}sec	9.88×10^{-17}	36.85
5×10^{-13}sec	1.06×10^{-15}	34.48
7×10^{-13}sec	1.01×10^{-15}	34.53
9×10^{-13}sec	1.91×10^{-16}	36.20
12×10^{-13}sec	3.42×10^{-16}	35.61
15×10^{-13}sec	6.51×10^{-17}	37.27

Table 7-3: Values of the likelihood for five different lifetimes. Here we have assumed that the charm events were of a single lifetime.

$$\tau(D^+)=(8.2^{+1.1}_{-0.9})\times10^{-13}\ \text{sec}$$

$$\tau(D^0)=(3.9\pm0.4)\times10^{-13}\ \text{sec}$$

We fit a model of $D\bar{D}$ production with an x_F dependence of $(1 - |x|)^5$, semi-leptonic branching ratios of 11% ($D^\pm$) and 5% (D^0), and separate lifetimes taken from the measured world average for the D^+ and D^0 lifetimes, and found that the miss distance distribution of the twenty-three events was in good agreement with the model's predictions. The probability of obtaining our result is 60%.

7.4 Conclusions

We measured a sample of 23 charm candidate events produced in n-Ne collisions (~330 GeV/c) using a High Resolution Streamer Chamber and a downstream muon spectrometer. The number of background events in the candidate sample is 5.68. From the the muon distributions, we were able to measure production and decay properties of hadronically produced charm particles.

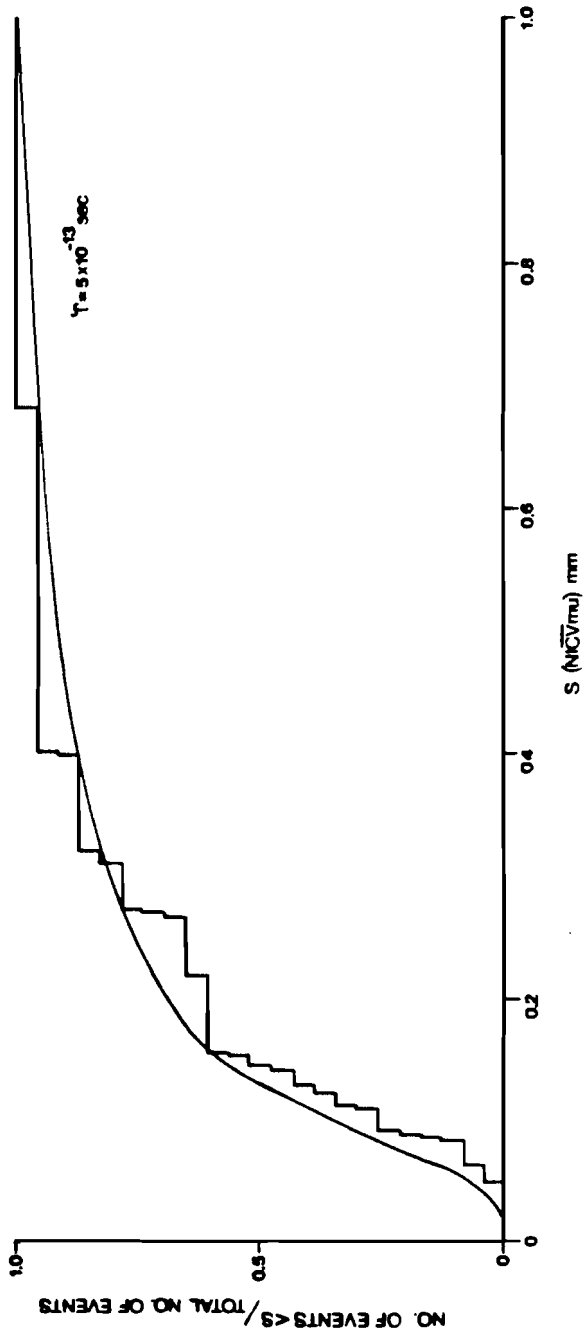

Figure 7-16: The integral distribution of the measured miss distances and the prediction of the model where the D lifetime is 5×10^{-13} sec.

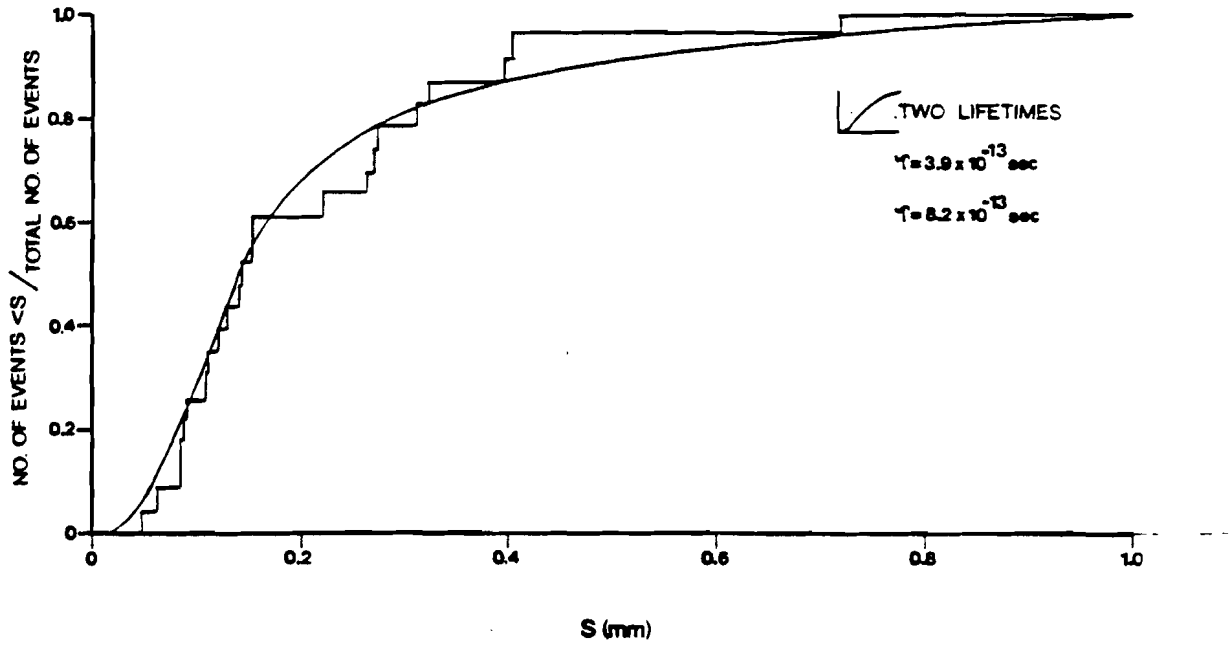

Figure 7-17: The intrgral distribution of the measured miss distances and the predictions of the model in which $D^{\pm}$ has a lifetime of 8.2×10^{-13}sec and D^0 has a lifetime of 3.9×10^{-13}sec

- From the charge ratio N(+):N(−) of the candidates' muons and the numbers of candidates collected in each of the two toroid polarity modes, we found two production models that described the measured result.

  1. In the first model, the D's ($c\bar{q}$) are produced with a $(1 - |x|)^7$ dependence and the $\bar{D}$'s ($\bar{c}q$) are produced with a $(1 - |x|)^1$ dependence indicative of leading particles.
  2. In the second model, both the D's and $\bar{D}$'s are produced centrally with a $(1 - |x|)^5$ distribution.

  Although the statistics are limited, our results say that D's, which contain no valence quarks from the beam or the target, are produced centrally. This is consistent with the predictions of the gluon fusion model and the flavor excitation model. We are unable to distinguish between models with or without recombination effects in $\bar{D}$ production.

- We conclude that $\Lambda_c^+\bar{D}$ production is not dominant in n-Ne collisions.
- We find that the measured momentum spectrum is consistent with the decay muons from charmed particles ($D\bar{D}$) produced with an x_F dependence of $(1 - |x|)^7(1 - |x|)^1$ or a $(1 - |x|)^5(1 - |x|)^5$ dependence. This disagrees with the x_F dependence measured by LEBC in 360 GeV/c p-H_2 collisions.
- The P_t spectrum of the muons is consistent with the predictions of the standard model of three-body charm decay. The energy spectrum of electrons from charm decay [26] is used as a model for the muon energies in the decay model. Our result is consistent with μ-e universality.
- We measured an average $D(\bar{D})$ lifetime of $(6.0\pm1.0)\times10^{-13}$sec which is equal to the average of the values of the $D^\pm$ and the D^0 lifetimes measured elsewhere.

Appendix I. The Momentum Analysis

The analysis of the muons' momenta was complicated by the large multiple Coulomb scattering of the muons in the iron toroids. In order to determine the initial angles θ_o and ϕ_0, the initial momentum P_o and the charge Q of a muon coming from the streamer chamber and passing through the steel of the downstream apparatus, we made a global fit to the measured data points at the streamer chamber vertex and the PWC's. The fitting was performed using the Method of Maximum Likelihood.

We calculated the probability density function describing the probability of measuring the data points, call them $\{ T^M \}$, for a given set of of initial parameters $\{1/QP_o, \theta_o, \phi_o\}$. Since the multiple scattering introduces a correlation between the data points along the particle's trajectory, the probability density function gives the joint probability of measuring all the data points along the tracks at one time. The initial parameters are included by calculating an unscattered muon trajectory for the parameters $\{1/QP_o, \theta_o, \phi_o\}$. These reference trajectories are calculated so that they include the effects of energy loss in the steel and magnetic bending in the toroid. In other words, the probability density function of interest here describes the probability of measuring a set of deviations from a calculated reference trajectory at the positions of each of the three PWC's. The points on the reference trajectory are indicated as $\{ T^t \}$. The initial parameters of the reference trajectory were varied to find the best fit to the measured chamber hits.

We used the coordinates of the fitted triplet centers as the measured values of the Y and Z coordinates at each chambers. In this coordinate system X lies along the beam axis and Z points up. The errors σ were the errors derived from the triplet fits. See Chapter Six for further details on triplet fitting.

The probability density function describing the projected displacement and the

change of angle of a particle after traversing a scatterer of thickness t is given by the following equation.

$$P(\theta_y, y, t) = 2\sqrt{3}\,\frac{1}{\pi}\,\frac{1}{\theta_s^{\,2} t^2}\exp\left[-\frac{4}{\theta_s^{\,2}}\left(\frac{\theta_y^{\,2}}{t} - \frac{3y\theta_y}{t^2} + \frac{3y^2}{t^3}\right)\right] \tag{3}$$

The quantity $\theta_s^{\,2}$ is the mean squared scattering angle in a unit length of the scattering material. In order to complete the description of the scattering, we make the approximation that the scattering in the XY plane is independent of the scattering in the XZ plane. Therefore, a similar but independent expression can be written for Z.

I.1 The Probability Density Function

The problem at hand is one with six large scatterers and three chambers that record the position of the particles at three points along the trajectory. Two of the scatterers are magnetized. The streamer chamber interaction vertex gives a fourth measured point. Considering the large multiple scattering in the steel, it is reasonable to ascribe the vertex to the center of the streamer chamber. In order to describe the scattering properly, a probability density function is needed that will determine the joint probability of observing y_B in the interval y_B to y_B+dy_B, z_B in the interval z_B to z_B+dz_B, y_D in the interval y_D to y_D+dy_D, z_D in the interval z_D to z_D+dz_D, y_{T2} in the interval y_{T2} to $y_{T2}+dy_{T2}$ and z_{T2} in the interval z_{T2} to $z_{T2}+dz_{T2}$ when a particle of given charge, momentum and angle passes from the streamer chamber through the entire apparatus. Here we will assume that the muon originates at the center of the streamer chamber. For the moment, we will ignore the contribution to the measurement error from the finite resolution of the wire chambers.

Consider the case with one scatterer and one chamber (see Figure 8-1). Define Δy_A as the difference between the measured point at chamber A and the point on the reference trajectory at chamber A. In the small angle approximation, the path length in the scatterer is simply the thickness of the scatterer. The probability of deviating a distance Δy_A from the reference trajectory is

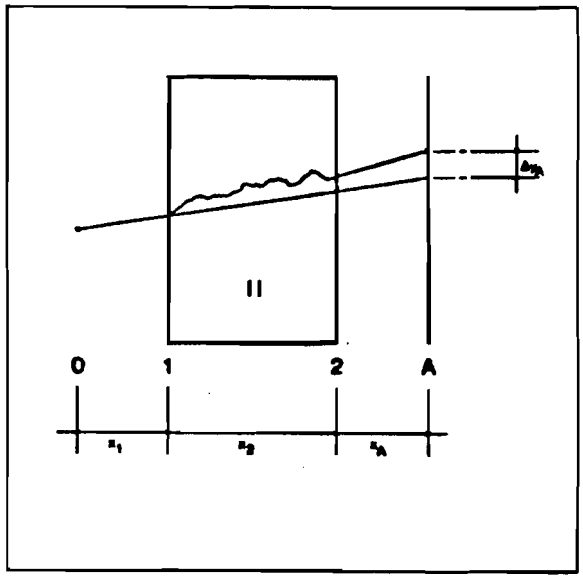

Figure 8-1: One scatterer and one chamber

$$P(\Delta y_A) = \frac{2\sqrt{3}}{\pi}\frac{1}{\theta_{S2}^2 x_2^2}\int d(\Delta\theta_{y2})\, d(\Delta y_2)\, d(\Delta\theta_A)\delta(\Delta\theta_A - \Delta\theta_2)\,\delta(\Delta y_A - \Delta y_2 - \Delta\theta_{y2}x_A)$$
$$exp\left[-\frac{4}{\theta_{S2}^2}\left(\frac{\Delta\theta_{y2}^2}{x_2} - \frac{3\Delta y_2\Delta\theta_{y2}}{x_2^2} + \frac{3\Delta y_2^2}{x_2^3}\right)\right] \tag{4}$$

Extending this definition to describe the E-630 hadron shield and toroid magnets, six large scatterers of iron and concrete must be included. A diagram of the apparatus is shown in Figure 8-2. The reference trajectory { T^t } describes the path of the particle without multiple scattering, however energy loss and magnetic bending are included. Here we assume that the bend angles are small and the scattering can be always described independently in XY and XZ planes. The total probability density function is then factorable:

$$P(y_B, y_D, y_{T2}, z_B, z_D, z_{T2}) = P(y_B, y_D, y_{T2}) \cdot P(z_B, z_D, z_{T2}) \tag{5}$$

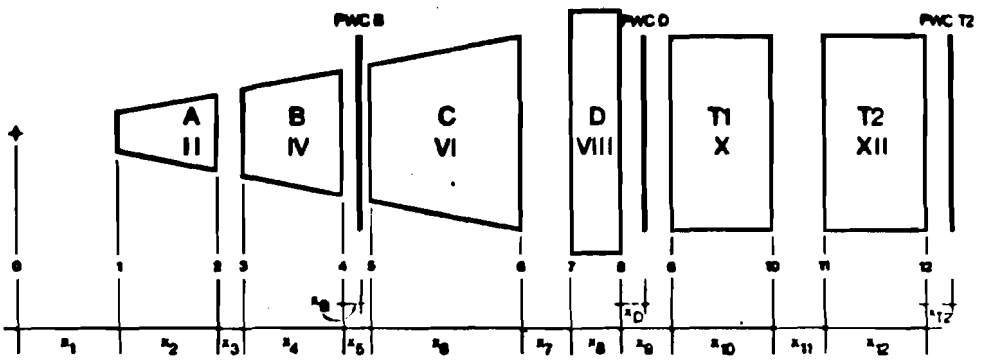

Figure 8-2: Schematic layout of the downstream hadron shield and toroids

The probability density function describing the scattering in the XY plane of a particle traversing the entire apparatus is given in equation 6.

$$
\begin{aligned}
P(\Delta y_B,\ \Delta y_D,\ \Delta y_{T2}) = \left(\frac{2\sqrt{3}}{\pi}\right)^6 \int \cdots \int d(\Delta\theta_B)\, d(\Delta\theta_D)\, d(\Delta\theta_{T2}) \prod_{\substack{i=1 \\ \text{even}}}^{12} \Bigg\{ & d(\Delta\theta_i)\, d(\Delta y_i) \\
& \frac{1}{\theta_{Si}^2 x_i^2}\, exp\left[-\frac{4}{\theta_{Si}^2}\left(\frac{\Delta\theta_{yi}}{x_i} - \frac{3\Delta y_i \Delta\theta_{yi}}{x_i^2} + \frac{3\Delta y_i^2}{x_i^3}\right)\right] \\
& \delta(\Delta\theta_B - \Delta\theta_4^m)\, \delta(\Delta\theta_D - \Delta\theta_8^m)\, \delta(\Delta\theta_{T2} - \Delta\theta_{12}^m) \\
& \delta(\Delta y_B - \Delta y_4^m - \Delta\theta_4^m x_B)\, \delta(\Delta y_D - \Delta y_6^m - \Delta\theta_6^m x_D) \\
& \delta(\Delta y_{T2} - \Delta y_{12}^m - \Delta\theta_{12}^m x_{T2}) \Bigg\}
\end{aligned}
\tag{6}
$$

$$\text{where} \qquad \Delta y_i = \Delta y_i^m - (\Delta y_{i-2}^m + x_{i-1}\Delta\theta_{i-2}^m + x_{i-2}\Delta\theta_{i-2}^m)$$

$$\Delta\theta_i = \Delta\theta_i^m - \Delta\theta_{i-2}^m$$

$$\Delta y_i^m = y_i^m - y_i^t$$

$$\Delta\theta_i^m = \theta_i^m - \theta_i^t$$

$$\Delta\theta_0^m = 0$$

$$\Delta\theta_{i-1}^m = \Delta\theta_{i-2}^m$$

$$\text{and} \qquad \theta_{Si}^2 = \left(\frac{0.021\ \text{GeV}}{\beta c p_i}\right)^2 \frac{1}{(X_0)_i}$$

The quantity Δy_i is the deflection of the particle in the ith scatterer, Δy_i^m is the total deflection of the particle from the reference trajectory at the end of the ith scatterer. The path of the particle in air is represented by a δ-function connecting the position of the particle at the end of the scatterer to the position at the next shield element or next chamber. By integrating over all the possible displacements and angular deflections at each scatterer, an expression is obtained for the probability density function describing the likelihood of observing the deflections Δy_B, Δy_D and Δy_{T2} for a particle of momentum p.

The measurement error is included with the addition of three Gaussians of the form given in equation 7.

$$P(\Delta y_B^M \mid \Delta y_B) = \frac{1}{\sqrt{2\pi}\,\sigma_B}\, exp\left[-\frac{1}{2}\left(\frac{y_B^M - y_B}{\sigma_B}\right)^2\right] \tag{7}$$

The final probability density describing scattering in the XY plane is given by 8.

$$\begin{aligned} P(\Delta y_B{}^M, \Delta y_D{}^M, \Delta y_D{}^M) \;=\; & \int\int\int \; d(\Delta y_B) d(\Delta y_D) d(\Delta y_{T2}) \\ & P(\Delta y_B{}^M | \Delta y_B) P(\Delta y_D{}^M | \Delta y_D) P(\Delta y_{T2}{}^M | \Delta y_D) \\ & P(\Delta y_B, \Delta y_D, \Delta y_{T2}) \end{aligned} \tag{8}$$

The likelihood of measuring $y_B{}^M$,$y_D{}^M$ and $y_{T2}{}^M$ comes from expressing the above probability density function in terms of the reference trajectory, setting $\Delta y_B{}^M = y_B{}^M - y_B{}^t$, where y_B is the y coordinate of the point on the reference trajectory at PWCB.

The integrals can be easily calculated once all the terms in the exponentials are factored. The integrand can then be written in the following form.

$$I = \text{const} \cdot \exp -\left[\sum_{ij} A_{ij} X_i X_j + \sum_i B_i X_i + C\right]$$

The integrals over the δ-functions are completed first. The 12 remaining integrals run from $-\infty$ to $+\infty$ and are Gaussian in nature. By factoring the exponential, the problem reduces to 12 independent Gaussian integrals.

I.2 Generating the Likelihood

In order to write the polynomial in the exponential in the form

$$\sum_i A_{ij}X_iX_j + \sum_i B_iX_i + C,$$

we used the algebraic manipulation program MACSYMA.[7] In order to solve the integrals, we completed the squares numerically of the polynomial, putting the polynomial in the form

$$\prod_i A_{ii}(X_i+B_i')^2+C'$$

which yields twelve independent Gaussian integrals that can be easily solved.

The reference trajectories were calculated in a simulation program where the muons were generated at the center of the streamer chamber with charge Q and angles Θ,Φ and initial momentum P. The particles were then propagated through the apparatus without scattering. For this simulation, the effects of energy loss in the steel and concrete were included. This was essential for accurate simulation in the toroidal magnets. For each of the six scattering elements, the average scattering angle per unit length θ_s was calculated. The simulation program calculates the energy loss and the bending in the magnet in 5 cm steps. See Appendix II for further details.

By varying the initial parameters 1/QP, Θ and Φ, we search for a maximum of the likelihood of a measured set of $y_B{}^M$, $y_D{}^M$,$y_{T2}{}^M$,$z_B{}^M$,$z_D{}^M$,$z_{T2}{}^M$.

$$L=P(y_B{}^M,y_D{}^M,y_{T2}{}^M)\ P(z_B{}^M,z_D{}^M,z_{T2}{}^M)$$

The results of the analysis are given in Chapter Six. The algorithm worked well for calculating the angles. There was, however, a bias in the momentum calculation caused by the momentum dependence of the width of the probability density function. A correction was made to the final estimate of the momentum to correct this bias. Figures

---

[7]MACSYMA is an algbraic manipulation program written at the MIT Math Lab.

8-3, 8-4 and 8-5 give the graphs of the resolution of the detector for momentum, polar angle and azimuthal angle. The momentum resolution is shown as $\delta p/p$, while the angular resolutions are presented as $\delta\theta$ and $\delta\phi$.

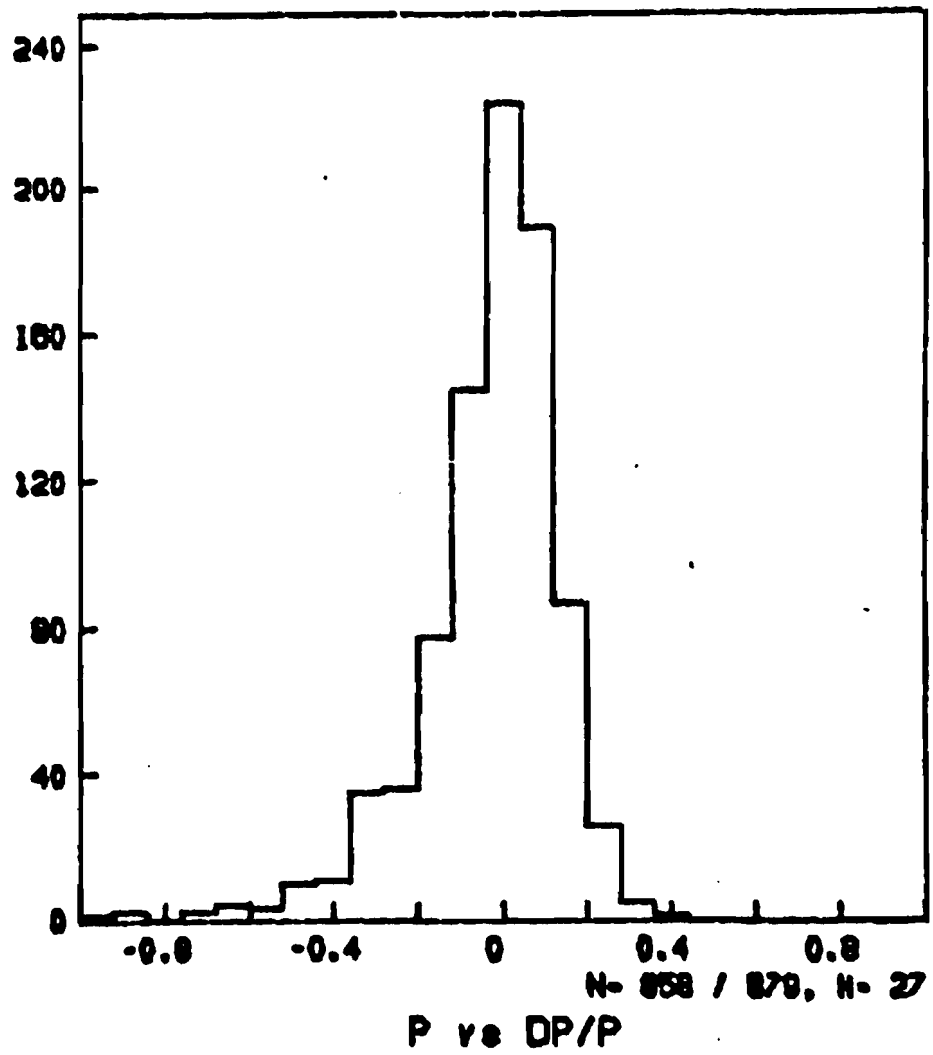

Figure 8-3: Momentum resolution, $\delta p/p$, taken from Monte Carlo events

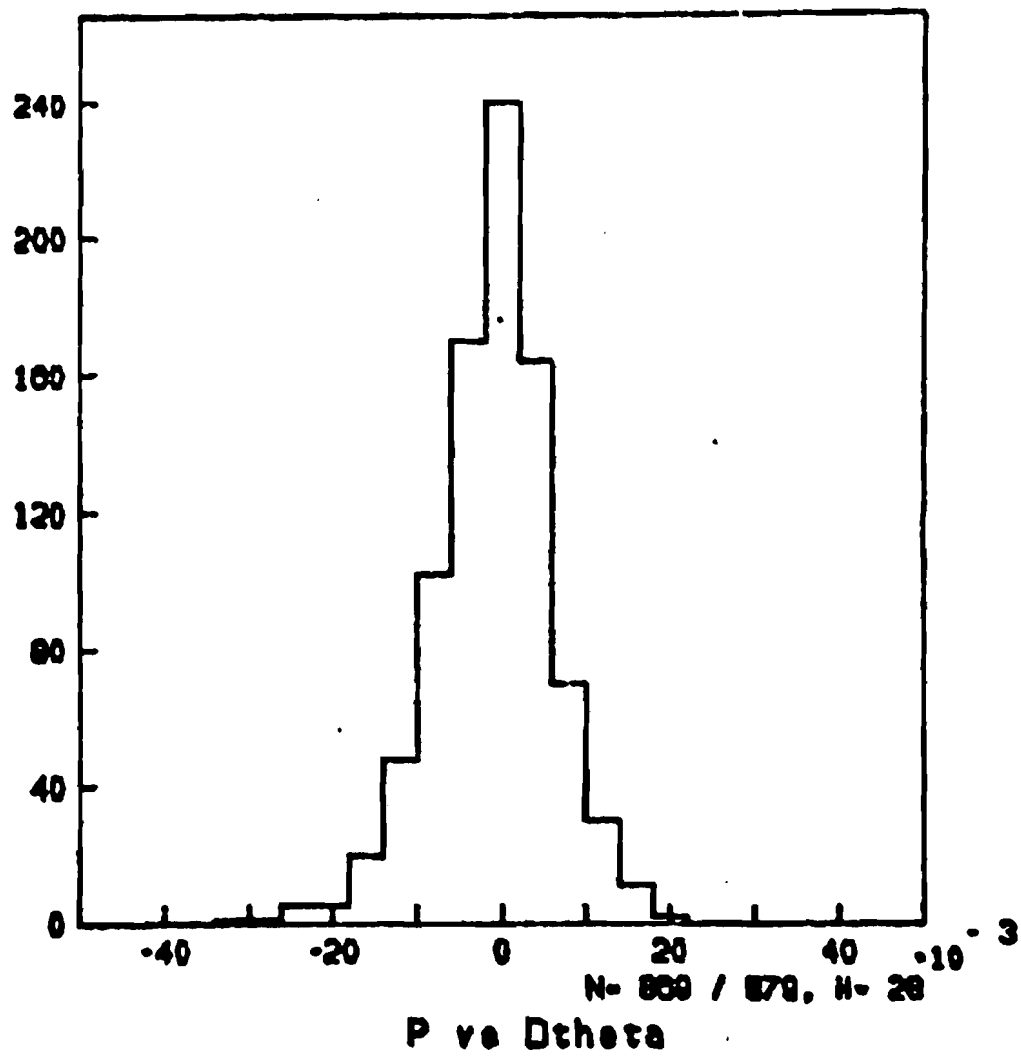

Figure 8-4: Polar angle resolution, $\delta\theta$ in radians, taken from Monte Carlo events

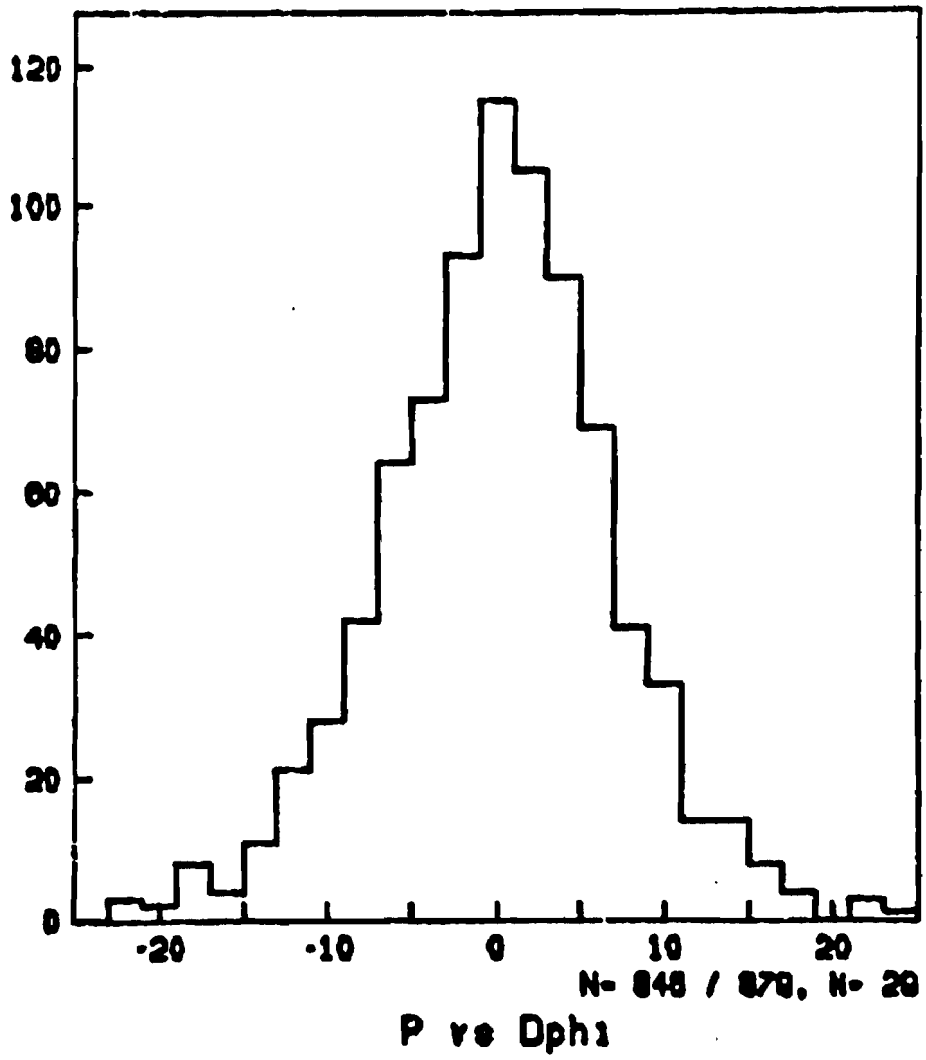

Figure 8-5: Azimuthal angle resolution, $\delta\phi$ in degrees, taken from Monte Carlo events

Appendix II. Monte Carlo Simulation

The Monte Carlo simulation program was designed to study the trigger acceptance and the charm detection efficiency. The trigger efficiency measures the probability of triggering on a charmed particle that decays inside the streamer chamber into a muon. The detection efficiency measures the probability of detecting at least one charm candidate in the pictures with a muon that satisfies the muon trigger requirements.

The simulation can be broken into three parts, the event generation, the muon trajectory and the streamer chamber track simulation. The first and the last parts are described in some detail in Reference [112], but will be briefly reviewed here. The muon trajectory simulation will be discussed in more detail. Figure 9-1 shows an outline of the Monte Carlo Program.

II.1 Event Generation

The events are generated after first simulating the energy spectrum and spot size of the neutron beam. Each beam particle interacts inside the fiducial volume of the chamber and the interaction produces a $D\bar{D}$ pair. The production of each particle is considered independently. The production spectrum of each is based on the model

$$\frac{d\sigma}{dx_F dp_T^2} = C\,(1 - |x|)^n\, e^{-2.5 p_T}.$$

The interaction produces $n\pi$'s in addition to the charm pair with $\langle n_{ch} \rangle = 2.12 + 0.179 \ln S_{eff}$, where S_{eff} is the effective energy in the center of mass [112].

Each charmed particle is allowed to decay according to the measured decay modes. The hadronic branching ratios are taken from References [5, 9] with the exception of the semi-leptonic branching ratio. The average semi-leptonic branching ratio is taken to be

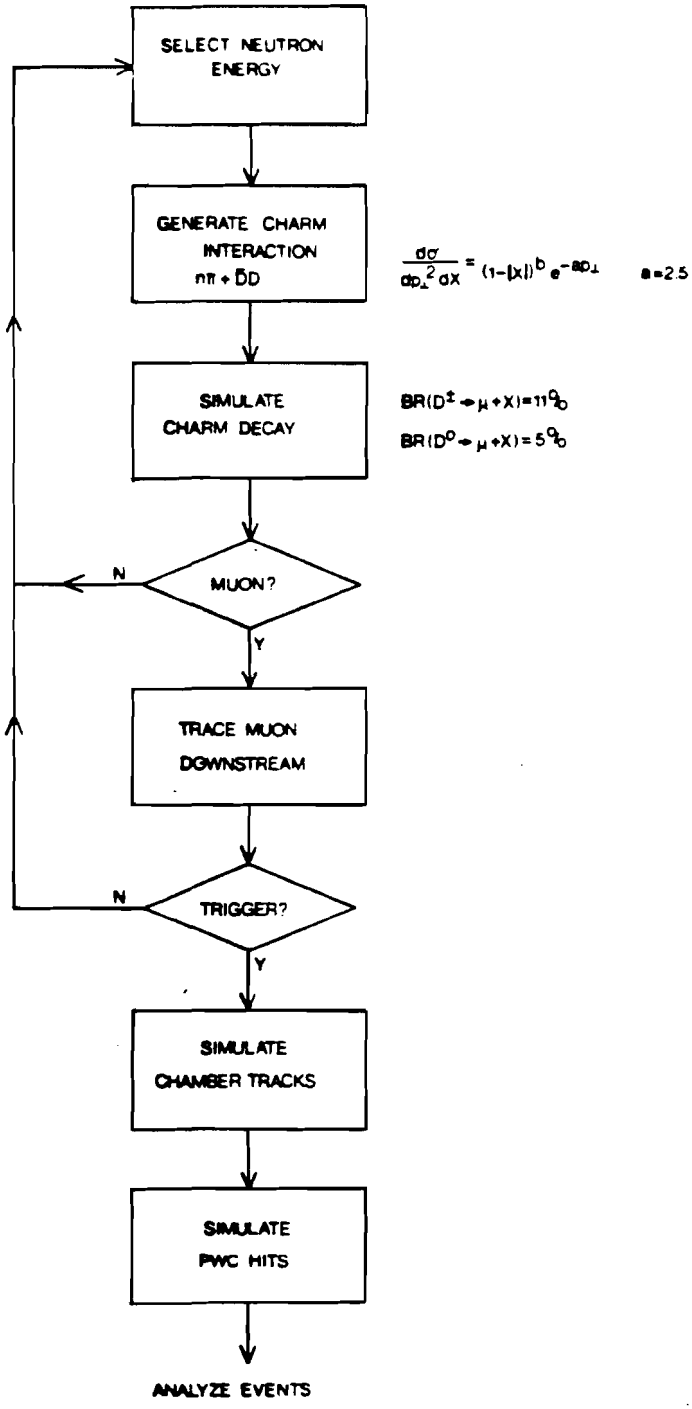

Figure 7-1: An outline of the Monte Carlo

8% [111] and the ratio $\tau(D^+)/\tau(D^0)$ is set to 2-2.5 [94, 75]. The individual values of the branching ratio into muons are set to

$$Br(D^{\pm} \rightarrow \mu) = 11\%$$

$$Br(D^0 \rightarrow \mu) = 5\%$$

$$Br(\Lambda_c^+ \rightarrow \mu) = 5\% \text{ [116]}$$

The lifetimes are chosen in accordance with the latest world averages [94].

$$\tau(D^+) = (8.2 \begin{smallmatrix} + 1.1 \\ - 0.9 \end{smallmatrix}) \times 10^{-13} \text{ sec}$$

$$\tau(D^0) = (3.9 \pm 0.4) \times 10^{-13} \text{ sec}$$

$$\tau(\Lambda_c^+) = (2.2 \begin{smallmatrix} + 0.7 \\ - 0.4 \end{smallmatrix}) \times 10^{-13} \text{ sec}$$

Events with at least one charmed particle decaying into a muon with lab momentum greater than 6 GeV/c within the chamber are accepted for tracking through the apparatus.

The semi-leptonic decays of the charmed particles are split into two classes of three body decays. Fifty percent of the D's decay into $K\mu\nu$ and fifty percent into $K^*(890)\mu\nu$.

II.2 The Muon Trajectories

If the event generates a charm decay muon with momentum greater than 6 GeV and between 30 and 200 mrad, the muon is propagated through the downstream apparatus. The muon is swum through the shield in 5 centimeter segments. In each segment, the energy loss and multiple scattering of the muon are determined. In the toroid the bending of the muon is calculated in 5 centimeter steps as well. For each step, the energy loss is considered first, then the bending if appropriate, and then the multiple scattering.

The energy loss of the muon in the steel and concrete is calculated according to the following formula as outlined in references [5, 60].

$$\frac{dE}{ds} = \frac{D\, Z_{med}\, \rho_{med}}{A_{med}} \left[\frac{Z_{inc}}{\beta} \right]^2 \left[\ln\left(\frac{2 m_e \gamma^2 \beta^2 c^2}{I} \right) - \beta^2 - \tfrac{1}{2}\delta - \frac{C}{Z_{med}} \right]$$

$D = 4\pi N_A r_e^2 m_e c^2$

$I \equiv$ binding energy of the electrons in the medium

$\delta \equiv$ density effect $\rightarrow 2\ln\gamma$ + constant
for ultra relativistic charges

$C \equiv$ shell corrections, for muons with speeds comparable to the electrons in the medium

$\rho_{med} \equiv$ density of the medium

The density effects and shell corrections are calculated as a function of $\eta \equiv \beta/\sqrt{1-\beta^2}$. The momentum at the middle of each segment is estimated

$$P_{middle} = P_i - \frac{5\ \text{cm}}{2} \left(\frac{P_i}{P_{xi}} \right) \frac{dP}{ds}.$$

where P_i refers to the momentum at the beginning of the segment. The new value of the intermediate momentum is used for calculating the magnetic bending and multiple scattering.

The azimuthal magnetic field B is calculated as a function of the position x along the beam axis and the radius ($\equiv(y^2+z^2)^{1/2}$) of the muon at the beginning of the toroid segment. The deflection of the particle in the field is calculated by rotating into a coordinate system where $Y_i' = 0$ and $Z_i' > 0$. The radius of curvature ρ is described in terms of P_{mid} given above.

$$\rho(\text{cm}) = \frac{P_{mid} \cos\lambda}{3.0\text{x}10^{-4}\, B_{mid}}$$

where $\cos\lambda = \sqrt{(P_{xi}')^2+(P_{zi}')^2}/P_i$

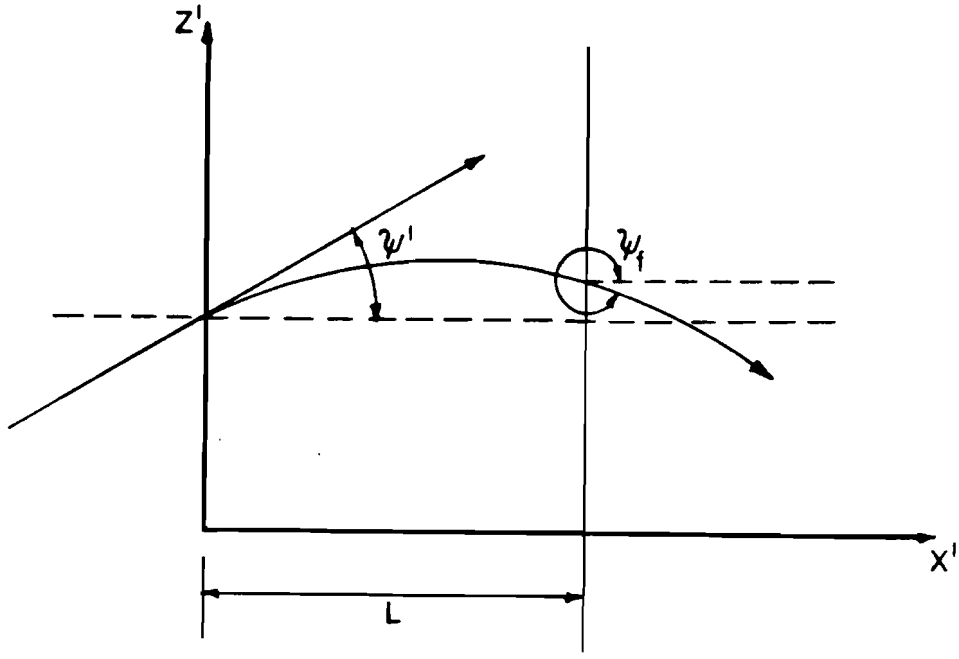

Figure 9-2: The bending of a particle in the steel toroid

The deflections in position and angle after a distance L are

$$\delta z = -\rho \cos\psi_i \left[1 - \left(1 - \frac{L^2 - 2\rho L \sin\psi_i}{(\rho\cos\psi_i)^2} \right)^{\frac{1}{2}} \right]$$

and

$$\sin\psi_f = \sin\psi_i - L/\rho$$

The multiple scattering is modeled according to the probability density function of Rossi [100] as described in Appendix I, Equation 1. For each length L (L=5cm) the mean square scattering angle θ_s is calculated.

$$\theta_s^2 = \left(\frac{0.021\ \text{GeV}}{\beta_{mid} P_{mid}}\right)^2 \frac{1}{L_{rad}}$$

$$P_{mid} = P_i - \tfrac{1}{2} s \cdot \frac{dP}{ds}$$

$$\beta_{mid} = 1 / (1 + [(E_i+P_i)(E_i-P_i) / P_{mid}^2])^{\frac{1}{2}}$$

The quantity s is the total path length of the muon in the steel.

The scattering is simulated in a frame where $P_y' = P_z' = 0$. In this frame, the multiple scattering can be calculated for (y', θ_y') and (z', θ_z') independently according to Equation 1 in Appendix I.

The structure of the Monte Carlo is such that the multiple scattering, energy loss or magnetic field can be "turned off" for testing purposes. In the simulation program used to calculate the reference trajectories for the muon analysis (Appendix I), the multiple scattering is turned off.

Between steel sections, the particles drift in air where the effects of energy loss and multiple scattering are neglected. Particles that pass into the hole are allowed to drift except if they pass through a cone veto counter or are inside the toroid hole. Muons exiting the outer edge of the steel drift to the next counter wall or PWC.

At each counter wall, there is a check to assure that the muon passes through a trigger counter. Muons inside the 30 mrad hole or outside the wall area are rejected. A check is made to assure that the remaining muon events satisfy the entire trigger requirement as defined in Chapter Four.

If any muon passes through the active region of a PWC, the hit is recorded and a hit width is assigned for each plane according to a Poisson distribution. The mean of the Poisson distribution is the average width of hits observed in the chamber. For each PWC, the mean cathode hit width is the average of the Z and U planes. A single cluster width is then chosen for the two cathode planes in each PWC. The final hit width is the

cluster width adjusted to match the physical dimensions of the cathode strips. The information about the PWC hits is written into the same format as the chamber data so that the events can be analyzed. A summary of the muon propagation is shown in Figure 9-3.

II.3 The Streamer Chamber

The measurement simulation program is a sophisticated program that is able to reproduce the track widths and obscured regions of the streamer chamber pictures [112]. With this program, we were able to determine the efficiency for seeing a charmed particle in the pictures. In particular, were were able to simulate events to test the hypothesis that events with tracks that miss the primary vertex (S/DS $>$ 3.0) are rich in charm.

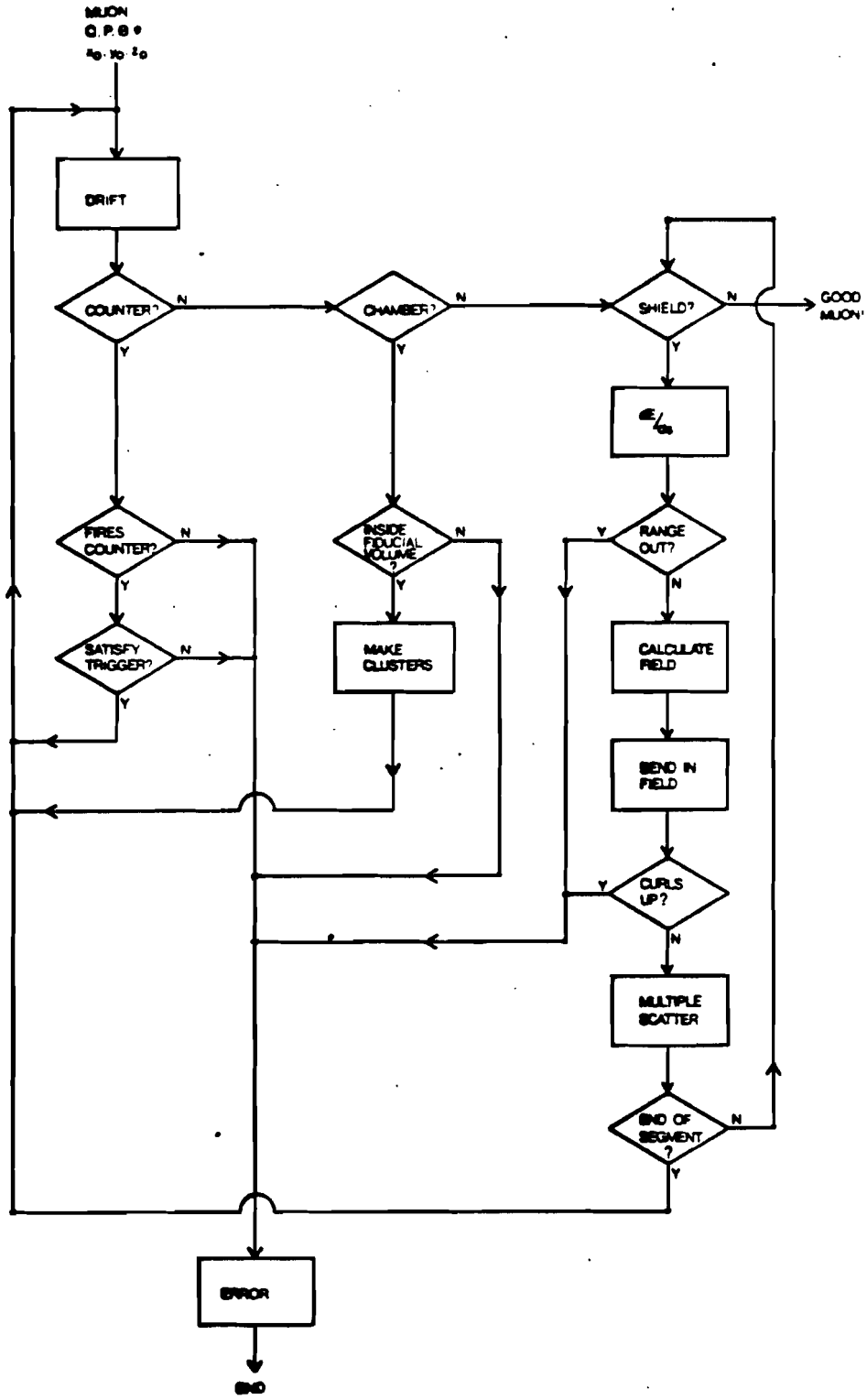

Figure 9-3: The muon trajectory Monte Carlo for a muon of charge Q and momentum P

Appendix III. The Candidate Events

EVENT 548 998

Toroid Mode	−1		
Muon: Momentum	11.5	+3.14 −2.06	GeV/c
Muon: Charge	+1		
Muon: Polar Angle θ	0.053	±0.012	radians
Muon: Azimuthal Angle ϕ	−155.6	±13.0	Degrees
Muon: Upstream X^2	0.14		
Miss distance Largest S/DS Track in Streamer Chamber	0.128	±0.036	mm
Total no. of Measured Tracks	23		
No. of Fragments	5		
No. of Fragments Measured	3		
Secondary Interactions	1		

EVENT 556 1944

Toroid Mode	+1		
Muon: Momentum	19.0	+8.49 −4.67	GeV/c
Muon: Charge	+1		
Muon: Polar Angle θ	0.107	±0.007	radians
Muon: Azimuthal Angle ϕ	15.8	± 4.5	Degrees
Muon: Upstream χ^2	0.37		
Miss Distance Largest S/DS Track in Streamer Chamber	0.128	±0.036	mm
Total no. of Measured Tracks	14		
No. of Fragments	5		
No. of Fragments Measured	3		
Secondary Interactions	0		

EVENT 570 334

Toroid Mode	+1		
Muon: Momentum	10.2	+3.09 −4.67	GeV/c
Muon: Charge	+1		
Muon: Polar Angle θ	0.084	±0.017	radians
Muon: Azimuthal Angle ϕ	−74.7	± 6.7	Degrees
Muon: Upstream X^2	2.66		
Miss Distance Largest S/DS Track in Streamer Chamber	0.337	±0.071	mm
Total no. of Measured Tracks	3		
No. of Fragments	0		
No. of Fragments Measured	0		
Secondary Interactions	0		

EVENT 574 1571

Toroid Mode	−1		
Muon: Momentum	21.1	+22.59 −7.52	GeV/c
Muon: Charge	+1		
Muon: Polar Angle θ	0.039	±0.006	radians
Muon: Azimuthal Angle ϕ	169.4	±12.4	Degrees
Muon: Upstream χ^2	2.46		
Miss Distance Largest S/DS Track in Streamer Chamber	0.270	±0.053	mm
Total no. of Measured Tracks	8		
No. of Fragments	5		
No. of Fragments Measured	0		
Secondary Interactions	0		

The primary interaction is upstream of the visible chamber volume.

EVENT 578 583

Toroid Mode	+1		
Muon: Momentum	7.7	+1.43 −1.07	GeV/c
Muon: Charge	+1		
Muon: Polar Angle θ	0.070	±0.002	radians
Muon: Azimuthal Angle ϕ	65.3	± 8.4	Degrees
Muon: Upstream X^2	1.42		
Miss Distance Largest S/DS Track in Streamer Chamber	0.401	±0.074	mm
Total no. of Measured Tracks	8		
No. of Fragments	5		
No. of Fragments Measured	0		
Secondary Interactions	0		

EVENT 578 1050

Toroid Mode	+1		
Muon: Momentum	7.8	+1.25 −0.95	GeV/c
Muon: Charge	−1		
Muon: Polar Angle θ	0.031	±0.006	radians
Muon: Azimuthal Angle ϕ	133.7	±10.9	Degrees
Muon: Upstream X^2	0.16		
Miss Distance Largest S/DS Track in Streamer Chamber	0.153	±0.045	mm
Total no. of Measured Tracks	5		
No. of Fragments	2		
No. of Fragments Measured	0		
Secondary Interactions	0		

EVENT 578 2138

Toroid Mode	+1		
Muon: Momentum	16.6	+7.44 −2.06	GeV/c
Muon: Charge	−1		
Muon: Polar Angle θ	0.070	±0.006	radians
Muon: Azimuthal Angle ϕ	−67.3	± 5.4	Degrees
Muon: Upstream X^2	1.57		
Miss Distance Largest S/DS Track in Streamer Chamber	0.064	±0.018	mm
Total no. of Measured Tracks	10		
No. of Fragments	2		
No. of Fragments Measured	0		
Secondary Interactions	0		

EVENT 581 509

Toroid Mode	+1		
Muon: Momentum	8.4	+1.13 −0.90	GeV/c
Muon: Charge	+1		
Muon: Polar Angle θ	0.114	±0.011	radians
Muon: Azimuthal Angle ϕ	−20.3	± 5.5	Degrees
Muon: Upstream X^2	0.01		
Miss Distance Largest S/DS Track in Streamer Chamber	0.049	±0.016	mm
Total no. of Measured Tracks	9		
No. of Fragments	1		
No. of Fragments Measured	1		
Secondary Interactions	0		

EVENT 590 423

Toroid Mode	+1		
Muon: Momentum	12.8	+3.95 −2.54	GeV/c
Muon: Charge	+1		
Muon: Polar Angle θ	0.061	±0.009	radians
Muon: Azimuthal Angle ϕ	−148.3	± 6.8	Degrees
Muon: Upstream X^2	0.01		
Miss Distance Largest S/DS Track in Streamer Chamber	0.085	±0.028	mm
Total no. of Measured Tracks	11		
No. of Fragments	4		
No. of Fragments Measured	4		
Secondary Interactions	0		

EVENT 590 2067

Toroid Mode	+1		
Muon: Momentum	11.5	+3.33 −2.19	GeV/c
Muon: Charge	+1		
Muon: Polar Angle θ	0.063	±0.008	radians
Muon: Azimuthal Angle ϕ	148.7	± 6.8	Degrees
Muon: Upstream X^2	0.14		
Miss Distance Largest S/DS Track in Streamer Chamber	0.273	±0.047	mm
Total no. of Measured Tracks	8		
No. of Fragments	1		
No. of Fragments Measured	1		
Secondary Interactions	0		

The primary interaction is upstream of the visible chamber volume.

EVENT 599 594

Toroid Mode	−1		
Muon: Momentum	9.7	+2.52 −1.73	GeV/c
Muon: Charge	−1		
Muon: Polar Angle θ	0.056	±0.001	radians
Muon: Azimuthal Angle ϕ	−26.4	± 8.9	Degrees
Muon: Upstream X^2	0.33		
Miss Distance Largest S/DS Track in Streamer Chamber	0.143	±0.040	mm
Total no. of Measured Tracks	9		
No. of Fragments	5		
No. of Fragments Measured	0		
Secondary Interactions	0		

EVENT 600 1296

Toroid Mode	−1		
Muon: Momentum	11.8	+3.11 −2.07	GeV/c
Muon: Charge	+1		
Muon: Polar Angle θ	0.073	±0.012	radians
Muon: Azimuthal Angle ϕ	51.0	± 8.8	Degrees
Muon: Upstream χ^2	0.09		
Miss Distance Largest S/DS Track in Streamer Chamber	0.717	±0.045	mm
Total no. of Measured Tracks	10		
No. of Fragments	2		
No. of Fragments Measured	2		
Secondary Interactions	0		

EVENT 608 638

Toroid Mode	+1		
Muon: Momentum	8.5	+1.25 −0.97	GeV/c
Muon: Charge	−1		
Muon: Polar Angle θ	0.047	±0.011	radians
Muon: Azimuthal Angle ϕ	91.4	±10.1	Degrees
Muon: Upstream χ^2	0.01		
Miss Distance Largest S/DS Track in Streamer Chamber	0.311	±0.090	mm
Total no. of Measured Tracks	13		
No. of Fragments	0		
No. of Fragments Measured	0		
Secondary Interactions	0		

EVENT 611 1562

Toroid Mode	−1		
Muon: Momentum	12.6	+3.68 −2.38	GeV/c
Muon: Charge	−1		
Muon: Polar Angle θ	0.094	±0.011	radians
Muon: Azimuthal Angle ϕ	104.7	± 5.0	Degrees
Muon: Upstream X^2	1.41		
Miss Distance Largest S/DS Track in Streamer Chamber	0.111	±0.036	mm
Total no. of Measured Tracks	9		
No. of Fragments	3		
No. of Fragments Measured	1		
Secondary Interactions	0		

EVENT 616 7

Toroid Mode	+1		
Muon: Momentum	11.3	+3.08 −2.06	GeV/c
Muon: Charge	+1		
Muon: Polar Angle θ	0.067	±0.010	radians
Muon: Azimuthal Angle ϕ	32.6	±8.6	Degrees
Muon: Upstream X^2	0.06		
Miss Distance Largest S/DS Track in Streamer Chamber	0.123	±0.028	mm
Total no. of Measured Tracks	9		
No. of Fragments	2		
No. of Fragments Measured	0		
Secondary Interactions	0		

The primary interaction is upstream of the visible chamber volume.

EVENT 620 1439

Toroid Mode	−1		
Muon: Momentum	24.7	+22.24 −8.45	GeV/c
Muon: Charge	−1		
Muon: Polar Angle θ	0.068	±0.006	radians
Muon: Azimuthal Angle ϕ	−154.3	± 5.2	Degrees
Muon: Upstream X^2	5.00		
Miss Distance Largest S/DS Track in Streamer Chamber	0.153	±0.042	mm
Total no. of Measured Tracks	8		
No. of Fragments	1		
No. of Fragments Measured	1		
Secondary Interactions	1		

EVENT 630 1723

Toroid Mode	+1		
Muon: Momentum	8.1	+0.02 −0.02	GeV/c
Muon: Charge	+1		
Muon: Polar Angle θ	0.159	±0.0001	radians
Muon: Azimuthal Angle ϕ	105.7	± 4.8	Degrees
Muon: Upstream X^2	2.79		
Miss Distance Largest S/DS Track in Streamer Chamber	0.112	±0.033	mm
Total no. of Measured Tracks	9		
No. of Fragments	8		
No. of Fragments Measured	6		
Secondary Interactions	0		

EVENT 631 581

Toroid Mode	+1		
Muon: Momentum	7.3	+0.45 −0.40	GeV/c
Muon: Charge	+1		
Muon: Polar Angle θ	0.127	±0.013	radians
Muon: Azimuthal Angle ϕ	56.6	± 5.7	Degrees
Muon: Upstream X^2	0.14		
Miss Distance Largest S/DS Track in Streamer Chamber	0.396	±0.061	mm
Total no. of Measured Tracks	8		
No. of Fragments	0		
No. of Fragments Measured	0		
Secondary Interactions	0		

The primary interaction is upstream of the visible chamber volume.

EVENT 631 1934

Toroid Mode	+1		
Muon: Momentum	7.6	+0.77 −0.65	GeV/c
Muon: Charge	+1		
Muon: Polar Angle θ	0.111	±0.013	radians
Muon: Azimuthal Angle ϕ	−98.1	± 6.2	Degrees
Muon: Upstream X^2	0.23		
Miss Distance Largest S/DS Track in Streamer Chamber	0.219	±0.057	mm
Total no. of Measured Tracks	16		
No. of Fragments	5		
No. of Fragments Measured	2		
Secondary Interactions	0		

EVENT 631 2206

Toroid Mode	+1		
Muon: Momentum	13.1	+1.52 −1.26	GeV/c
Muon: Charge	+1		
Muon: Polar Angle θ	0.043	±0.001	radians
Muon: Azimuthal Angle ϕ	−17.2	± 8.2	Degrees
Muon: Upstream χ^2	0.87		
Miss Distance Largest S/DS Track in Streamer Chamber	0.141	±0.039	mm
Total no. of Measured Tracks	12		
No. of Fragments	4		
No. of Fragments Measured	3		
Secondary Interactions	0		

EVENT 635 218

Toroid Mode	−1		
Muon: Momentum	10.3	+2.56 −1.73	GeV/c
Muon: Charge	+1		
Muon: Polar Angle θ	0.048	±0.010	radians
Muon: Azimuthal Angle ϕ	84.6	± 9.4	Degrees
Muon: Upstream X^2	0.29		
Miss Distance Largest S/DS Track in Streamer Chamber	0.091	±0.028	mm
Total no. of Measured Tracks	8		
No. of Fragments	2		
No. of Fragments Measured	1		
Secondary Interactions	0		

EVENT 635 1856

Toroid Mode	−1		
Muon: Momentum	14.9	+3.53 −6.40	GeV/c
Muon: Charge	+1		
Muon: Polar Angle θ	0.055	±0.011	radians
Muon: Azimuthal Angle ϕ	−157.5	±12.3	Degrees
Muon: Upstream X^2	0.35		
Miss Distance Largest S/DS Track in Streamer Chamber	0.322	±0.074	mm
Total no. of Measured Tracks	7		
No. of Fragments	0		
No. of Fragments Measured	0		
Secondary Interactions	0		

The primary interaction is upstream of the visible chamber volume.

EVENT 664 2171

Toroid Mode	−1		
Muon: Momentum	8.8	+2.85 −1.77	GeV/c
Muon: Charge	−1		
Muon: Polar Angle θ	0.135	±0.011	radians
Muon: Azimuthal Angle ϕ	55.0	± 4.6	Degrees
Muon: Upstream X^2	3.67		
Miss Distance Largest S/DS Track in Streamer Chamber	0.088	±0.028	mm
Total no. of Measured Tracks	6		
No. of Fragments	1		
No. of Fragments Measured	0		
Secondary Interactions	0		

References

[1] K. Abe et al.
Lifetimes of Charmed Particles Produced in a 20-GeV γp experiment.
Physical Review Letters 48:1562, 1982.

[2] H. Abramowicz et al.
Prompt Neutrino Production in a Proton Beam Dump Experiment.
Zeitschrift fur Physik 13C:179, 1982.

[3] G. S. Abrams et al.
Discovery of a Second Narrow Resonance in e^+e^- Annihilation.
Physical Revies Letters 33:1453, 1974.

[4] B. Adeva et al.
Experimental Study of Inclusive Muon Spectra from Electron-Positron Collisions in the Energy Region $33 \leq \sqrt{s} \leq 38.54$GeV.
Physical Review Letters 51:443, 1983.

[5] M. Aguilar et al.
Particle Properties Data Booklet.
Lawrence Berkeley Laboratory, 1982.

[6] M. Aguilar-Benitez et al.
Lifetime Measurement of Charm Mesons Produced in π^-p and pp Interactions at 360 GeV/c.
Physics Letters 122B:312, 1983.

[7] M. Aguilar-Benitez et al.
Charm D-Meson Production in 360 GeV/c π^-p Interactions.
Physics Letters 123B:98, 1983.
LEBC Collaboration.

[8] M. Aguilar-Benitez et al.
Charm D Meson Production in 360 GeV/c pp Interactions.
Physics Letters 123B:103, 1983.
LEBC Collaboration.

[9] M. Aguilar-Benitez et al.
D Meson Branching Ratios and Hadronic Charm Production Cross Sections.
Physics Letters 135:237, 1984.
LEBC Collaboration.

[10] H. Aihara et al.
Prompt Electron Production in e^+e^- Annihilations at 29 GeV.
1984.

[11] E. Albini et al.
Electronic Measurement of the Lifetime of $D^\pm$ Mesons.
Physics Letters 110B:339, 1982.

[12] A. Ali and E. Pietarinen.
Semileptonic Decays of Heavy Quarks in Quantum Chromodynamics.
Nuclear Physics B 154:519-534, 1979.

[13] P. Alibram et al.
Observation of an excess of ν_e $\bar{\nu}_e$ events in a Beam Dump Experiment at 400 GeV.
Physics Letters 74B:134, 1978.

[14] G. Altarelli, N. Cabibbo, G. Corbo, L. Maiani, and G. Martinelli.
Leptonic Decay of Heavy Flavors.
Nuclear Physics B 208:365, 1982.

[15] G. Altarelli and L. Mani.
Identical Particle Interference in D^+ Meson Lifetime.
Physics Letters 118B:414, 1982.

[16] T. Appelquist, R. M. Barnett, K. Lane.
Charm and Beyond.
Annual Review of Nuclear and Particle Science 28:387-499, 1978.

[17] J. J. Aubert et al.
Experimental Observation of a Heavy Particle J.
Physical Review Letters 33:1404, 1974.

[18] J. J. Aubert et al.
Mesurements of the Proton Structure Function F_2 in Muon-Hydrogen Interactions at 120 and 280 GeV.
Physics Letters 105B:315, 1981.

[19] J. J. Aubert et al.
Measurements of the Nucleon Structure Function F_2 in Muon-Iron Interactions at 120, 250 and 280 GeV.
Physics Letters 105B:322, 1981.

[20] J. J. Aubert et al.
An Experimental Limit on Intrinsic Charm Component of the Nucleon.
Physics Letters 110B:73, 1982.
EMC Collaboration.

[21] J. J. Aubert et al.
The Ratio of the Nucleon Structure Function for $F_2{}^N$ for Iron and Deuterium.
Physics Letters 123B:275, 1983.

[22] J. J. Aubert et al.
Production of Charmed Particles in 250 GeV μ^+-Iron Interactions.
Nuclear Physics B 213, 1983.

[23] J. J. Aubert et al.
Measurement of the Deuteron Structure Function $F_2{}^D$ and a Comparison of Proton and Neutron Structure.
Physics Letters 123:123, 1983.

[24] J. -E. Augustin et al.
Discovery of a Narrow Resonance in e^+e^- Annihilation.
Physical Review Letters 33:1406, 1974.

[25] T. Aziz and A. Gurtu.
Charm Production in Fixed Target Experiments.
Zeitschrift fur Physik C, Particles and Fields :137-144, 1983.

[26] W. Bacino et al.
Semileptonic Decays on the D Meson.
Physical Review Letters 43:1073, 1979.

[27] W. Bacino et al.
Evidence for Unequal Lifetimes of the D^0, D^+.
Physical Review Letters 45:329, 1980.

[28] A. Badertscher et al.
Search for Charmed Particles with the Heavy Liquid Bubble Chamber BIBC.
Physics Letters 123B:471, 1983.

[29] R. Bailey et al.
Production and Decay Properties of D and D^* Mesons in π^-Be Interactions.
Physics Letters 132:241, 1983.

[30] R. Bailey et al.
Observation of $D^{*\pm}$ and $D^0/D^\pm$ Production in High Energy π^-Be Interactions at the SPS.
Physics Letters 123B:230, 1983.

[31] M. Bander, D. Silverman and A. Soni.
Mechanism for the Defference in Lifetimes of Charged and Neutral D Mesons.
Physical Review Letters 44:7, 1980.

[32] V. Barger, F. Halzen, S. Pakvasa and R.J.N. Phillips.
Beam Dump e/μ Asymmetry of Charged Higgs Origin.
Physics Letters 116B:357, 1982.

[33] U. Baur.
Weak Decays of Charmed Particles.
1982.
Talk given at the 1st Hellenic School on Elementary Particle Physics.

[34] A. Benvenuti et al.
A Large-Area Magnetic Spectrometer for the Study of High-Energy Neutrino Interaction.
Nuclear Instruments and Methods 125:457, 1975.

[35] B. J. Bjorken and S. L. Glashow.
Elementary Particle and SU(4).
Physics Letters 11:255, 1964.

[36] R. Blankenbecker, S. J. Brodsky.
Unified Description of Inclusive and Exclusive Reactions at all Momentum Transfers.
Physical Review D 10:2973, 1974.

[37] A. Bodek et al.
A Study of the Forward Production of Charm Particle Pairs in p-Fe and π^--Fe Interactions.
Physics Letters 113B:77, 1982.

[38] M. Boratav.
A Review of Charm Search in Hadronic Experiments.
Technical Report 79-40, CERN/EP, 1979.

[39] S. J. Brodsky, P. Hoyer, C. Peterson, N. Sakai.
The Intrinsic Charm of the Proton.
Physics Letters 93B:451, 1980.

[40] S. J. Brodsky, C. Peterson and N. Sakai.
Intrinsic Heavy Quark States.
Physical Review D 23:2745, 1981.

[41] N. Cabibbo and L. Maiani.
Two-Body Decays of Charmed Mesons.
Physics Letters B 73:418, 1978.

[42] N. Cabibbo, G. Corbo and L. Maiani.
Lepton Spectrum in Semileptonic Charm Decay.
Nuclear Physics B 93:155, 1979.

[43] T. R. Cardello.
Strange Charged Baryon Production.
PhD thesis, Yale University, 1983.

[44] C. E. Carlson and R. Suaya.
Hadronic Charm Production in QCD.
Physics Letters 81B:329, 1979.

[45] J. R. Biel.
Camac Diagnostic Language.
Fermilab PN-93.1.
A Language designed to aid in the testing of Camac modules.

[46] G. Charpak, D. Rahm, H. Steiner.
Some Development in the Operation of Multiwire Proportional Chambers.
Nuclear Instruments and Methods 80:13, 1970.

[47] G. Charpak et al.
Time degeneracy of Multiwire Proportional Chambers.
Nuclear Instruments and Methods 99:279-284, 1972.

[48] B. L. Combridge.
Associated Production of Heavy Flavour States in pp and $\bar{p}$ interactions: some QCD estimates.
Nuclear Physics B 151:429, 1979.

[49] P. S. Cooper.
Miss Distance Distribution.
Technical Report, Yale, 1981.
Internal Report.

[50] R. R. Crittenden and J. C. Krider.
A Method for Producing an Insensitive Region in a Multiwire Proportional Chamber.
Nuclear Instruments and Methods 128:599, 1975.

[51] A. De Rújula et al.
A Fresh Look at Neutrino Oscillations.
Nuclear Physics B 168:54, 1980.

[52] S. Dhawan.
A Fast Readout and Geometrical Reconstruction System for Proportional Wire Chambers.
IEEE Trans. Nuclear Science NS-21 1:922, 1974.

[53] M. Dine.
Monte Carlo Studies of the Hadron Filter and of Strange Particle Backgrounds for the High Resolution Streamer Chamber.
1977.
Internal Report for E-490.

[54] M. Dine and R. Kellogg.
Streamer Chamber Hadron Filter: Summary of Monte Carlo Predictions.
1978.
Internal Report for E-490.

[55] D. Drijard et al.
Observation of Charmed D Meson Production in pp collisions.
Physics Letters 81B:250, 1979.

[56] D. Drijard et al.
Charmed Baryon Production at the CERN Intersecting Storage Rings.
Physics Letters 85B:452, 1979.

[57] W. T. Eadie, D. Drijard, F. E. James, M. Roos, B. Sadoulet.
Statistical Methods in Experimental Physics.
North Holland, 1971.

[58] H. Eichinger and M. Regler.
Review of Track-Fitting Methods in Counter Experiments.
Technical Report 81-06, CERN, 1981.

[59] J. Ellis, M. K. Gaillard and D. V. Nanopoulos.
On the Weak Decays of High-Mass Hadrons.
Nuclear Physics B 100:313-328, 1975.

[60] U. Fano.
Penetration of Protons, Alpha Particles and Mesons.
Annual Review of Nuclear Science 13, 1963.

[61] H. Fritzsch and P. Minkowski.
The Puzzle of Nonleptonic Decays and its Resolution.
Physics Letters 90B:455, 1980.

[62] P. Fritze et al.
Further Study of the Prompt Neutrino Flux From 400 GeV Proton-Nucleus Collisions using BEBC.
Physics Letters 96B:427, 1980.

[63] A. G. Frodesen, O. Skjeggestad, H. Tofte.
Probability and Statistics in Particle Physics.
Universitetsforlaget, 1979.

[64] M. K. Gaillard, B. W. Lee, J. L. Rosner.
Search for Charm.
Reviews of Modern Physics 47:277, 1975.

[65] A. Barbaro-Galtieri.
Results from the Spear Magnetic Detector with Lead Glass Addition.
In *Proceedings of the 1977 International Conference on Lepton and Photon Interactions at High Energies.* Deutsches Elektron-Sychrotron DESY, 1977.

[66] K. L. Giboni et al.
Diffractive Production of th Charmed Baryon Λ_c^+ at the CERN ISR.
Physics Letters 85B:437, 1979.

[67] S. L. Glashow, J. Iliopoulos, L. Maiani.
Weak Interactions with Lepton-Hadron Symmety.
Physical Review D 2:1285, 1970.

[68] R. L. Gluckstern.
Uncertainties in Track Monentum and Direction, due to Multiple Scattering and Measurement Errors.
Nuclear Instruments and Methods 24:381, 1963.

[69] G. Goldhaber et al.
Observation in e^+e^- of a Narrow State at 1865 MeV/c^2 Decaying to $K\pi$and $K\pi\pi\pi$.
Physical Review Letters 37:255, 1976.

[70] B. Guberina, D. Takic and J. Trampetic.
Hard- and Soft-Gluonic Effects in Charmed Baryon Decays.
Zeitschrift fur Physik 13, 1982.

[71] J. F. Gunion.
Short Distance Counting Rules for Low p_T Fragmentation.
Physics Letters 88b:150, 1979.

[72] F. Halzen.
Production of Heavy Quarks.
In *Proceedings 21st International Conference on High Energy Physics*, pages C3-381. Journal de Physique, Les Editions de Physique, 1982.

[73] F. Halzen, W.-Y. Keung, D. M. Scott.
Production of Heavy Quarks: A Nonperturbative Approach.
Physics Review D 27:1631, 1983.

[74] J. Jonker et al.
Experimental Study of Prompt Neutrino Production in 400 GeV Proton-Nucleus collisions.
Physics Letters 96B:435, 1980.

[75] G. Kalmus.
Weak Decays of New Particles.
In *Proceedings 21st International Conference on High Energy Physics*, pages C-3 431-470. Journal de Physique, Les Editions de Physique, 1982.

[76] G. L. Kane, K. Stowe and W.B. Rolnick.
General Analysis of $D \rightarrow K\pi l\nu$ Physics.
Nuclear Physics B 152:390-428, 1979.

[77] J. Kirkby.
Direct Electron Production Measurements by DELCO at SPEAR.
In *Proceedings 1977 International Symposium on Lepton and Photon Interactions*, pages 1. Deutsches Elektron Synchrotron DESY, Hamburg, 1977.

[78] A. Litke et al.
Hadron Production by Electron-Positron Annihilation at 4-GeV Center-of-Mass Energies.
Physical Review Letters 30:1189, 1973.

[79] MIT Math Lab.
An algebraic manipulation program.

[80] R. Majka et al.
Design and Performance of a High Resolution Streamer Chamber.
Nuclear Instruments and Methods 192:241-252, 1982.

[81] B. Mecking.
The Accuracy of Track Reconstruction with Inhomogeneous Magnetic Detectors.
Nuclear Instruments and Methods 203:299-305, 1982.

[82] CERN Program Library.
Program for function minimization.

[83] F. Muller.
Hadroproduction of Heavy Flavours.
Technical Report EP/83-67, CERN, 1983.

[84] L. Taff, D. Ritchie, and T. Lagerlund.
RTMulti Data Acquisition System.
Fermilab PN-110.1K.
Data Acquisition System; Fermilab.

[85] T. Nash.
Recent Results on D Decays an Lepton, Photon, (and Hadron) Production of Charm.
In *Proceedings of the 1983 International Symposium on Lepton and Photon Interactions at High Energies*, pages 329-375. F. R. Newman Laboratory of Nuclear Studies, 1983.

[86] M. E. Nelson et al.
Inclusive Electron Production in e^+e^- Annihilation at 29 GeV.
Physical Review Letters 50:1542, 1983.

[87] R. Odorico.
Hadronic Production of Charm Via Flavour Excitation.
Nuclear Physics B 209:77-113, 1982.

[88] I. Peruzzi et al.
Observation of a Narrow Charged State at 1876 MeV/c^2 Decaying to an Exotic Combination of $K\pi\pi$.
Physical Review Letters 37:569, 1976.

[89] M. A. Peshkin.
Magnetic Field Measuring.
A series of notes on an integrator used for measuring magnetic fields.

[90] S. Petrera and G. Romano.
A Method to Evaluate the Detection and the Mean Life-Time of Short Lived Particles.
Nuclear Instruments and Methods 174:61-65, 1980.

[91] S. Petrera and G. Romano.
Detection and Measurement of Short Flight Paths in Nuclear Emulsions.
Nuclear Instruments and Methods 174:53-60, 1980.

[92] D. B. Pitman.
Lifetime Measurements of the D^+, F^+, and Λ^+.
PhD thesis, University of Toronto, 1982.

[93] C. Quigg.
Charmed Meson Decays and the Structure of the Charged Weak Current.
Zeitschrift fur Physik C 4, 1980.

[94] W. N. Reay.
Heavy Quark and Lepton Lifetimes.
In *Proceedings of the 1983 International Symposium on Lepton and Photon Interactions at High Energies*, pages 244-274. F. R. Newman Laboratory of Nuclear Studies, 1983.

[95] P. Rice-Evans.
Spark, Streamer, Proportional and Drift Chambers.
The Richelieu Press, London, 1974.

[96] J. L. Ritchie et al.
Forward Production of Charm States and Prompt Single Muons in 350 GeV/c p-Fe Interactions.
Physics Letters 126B:499, 1983.

[97] J. L. Ritchie.
Hadronic Charm Production by Protons and Pions on Iron.
PhD thesis, University of Rochester, 1983.

[98] J. L. Ritchie et al.
Forward Production of Charm States and Prompt Single Muons in 278 GeV π^--Fe Interactions.
Physics Letters B submitted, 1984.

[99] S. P. Rosen.
Remarks on the Differing Lifetimes of Charmed Mesons.
Physical Review Letters 44:4, 1980.

[100] B. Rossi.
High Energy Particles.
Prentice-Hall, 1952.

[101] J. Sandweiss.
The High Resolution Streamer Chamber.
Physics Today , 1978.

[102] J. Sandweiss et al.
Observation of the Production of Short-Lived Particles in a High Resolution Streamer-Chamber Experiment.
Physical Review Letters 44:1104, 1980.

[103] J. Sandweiss.
High Resolution Streamer Chambers for Heavy Quark Spectroscopy.
Physics Reports 83:39-60, 1982.

[104] J. Sandweiss.
E490 Monte Carlo.
Memo on the algorithm for the E-490 Monte Carlo to study Charm cross sections.

[105] F. Sauli.
Principles of Operation of Multiwire Proportional and Drift Chambers.
Technical Report 77-09, CERN, 1977.

[106] R. H. Schindler et al.
Measurements of the Properties of D-Meson Decays.
Physical Review D 24:78, 1981.

[107] D. Son et al.
Charmed-Baryon Production in $\nu d \rightarrow \mu^- \Lambda X$ Reactions.
Physical Review Letters 49:1128, 1982.

[108] R. Steiner.
Flavor Production in Hadron-Proton Collisions at 200 GeV/c.
PhD thesis, Yale University, 1984.

[109] S. Stone.
Weak Decays of Heavy Quarks.
In *Proceedings of the 1983 International Symposium on Lepton and Photon Interactions at High Energies*, pages 203-243. F. R. Newman Laboratory of Nuclear Studies, 1983.

[110] J. L. Thron.
A Search for Heavy Charged Particles and Light Nuclei and Antinuclei Production at High Energies.
PhD thesis, Yale University, 1983.

[111] G. H. Trilling.
The Properties of Charmed Particles.
Physics Reports 75, 1981.

[112] L. Tzeng.
Measurement of the Hadronic Charm Production Cross Section in a High Resolution Steamer Chamber Experiment.
PhD thesis, Yale University, 1984.

[113] N. Ushida.
Measurement of the D^0 Lifetime.
Physical Review Letters 45:1049, 1980.

[114] N. Ushida et al.
Measurement of D^+, F^+ and Λ_c^+ Charmed-Particle Lifetimes.
Physical Review Letters 45:1053, 1980.

[115] N. Ushida et al.
New Results for the Lifetimes of the $D^\pm$, $F^\pm$ and Λ_c^+.
Physical Review Letters 51:2362, 1983.

[116] E. Vella et al.
Observation of Semileptonic Decays of Charmed Baryons.
Physical Review Letters 48:1515, 1982.

[117] R. Winder and C. Michael.
Some QCD Esitmates of the Production of Heavy Flavours in Hadron-Hadron Collisions.
Nuclear Physics B 173:59, 1980.

[118] K. Winter.
Beam Dump Results.
In *Proceedings of the 1983 International Symposium on Lepton and Photon Interactions*, pages 177. Cornell University, 1983.

[119] A. Zichichi.
Heavy Flavours at the ISR.
In *International Conference on High Energy Physics. Proceedings*. European Physical Society, 1982.